

Summary of results: testing BF estimators with mock data

Abbe Whitford

June 19, 2023

Tests on simplistic mock data

This section shows results from applying the MVE and Kaiser MLE to simplistic mocks with varying survey geometries.

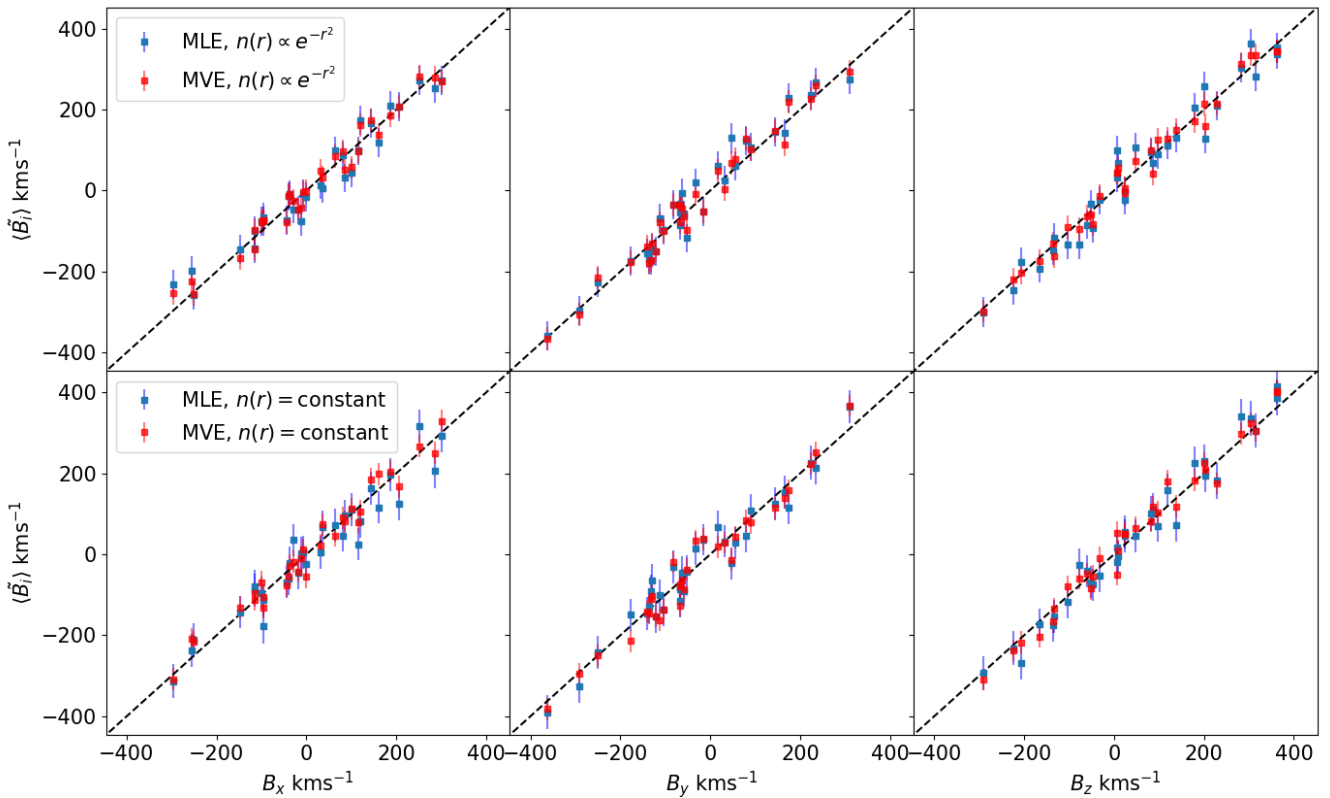


Figure 1: Recovered bulk flow components vs the real bulk flow components B_i for 512 simplistic mocks (constructed as described in the paper for the simplistic mocks), each with 5000 objects. Each point on this plot is an average of 16 different mocks but having the same net constant bulk flow \mathbf{B} added to the data in common. Blue points show the results from applying the MVE to the mocks (with 1500 objects in the ideal survey), red points the Kaiser MLE. The top panels are results for the estimator applied to mocks with a gaussian radial distribution of objects and a uniform radial distribution of objects in the lower panels. The mocks are spherical (full sky coverage).

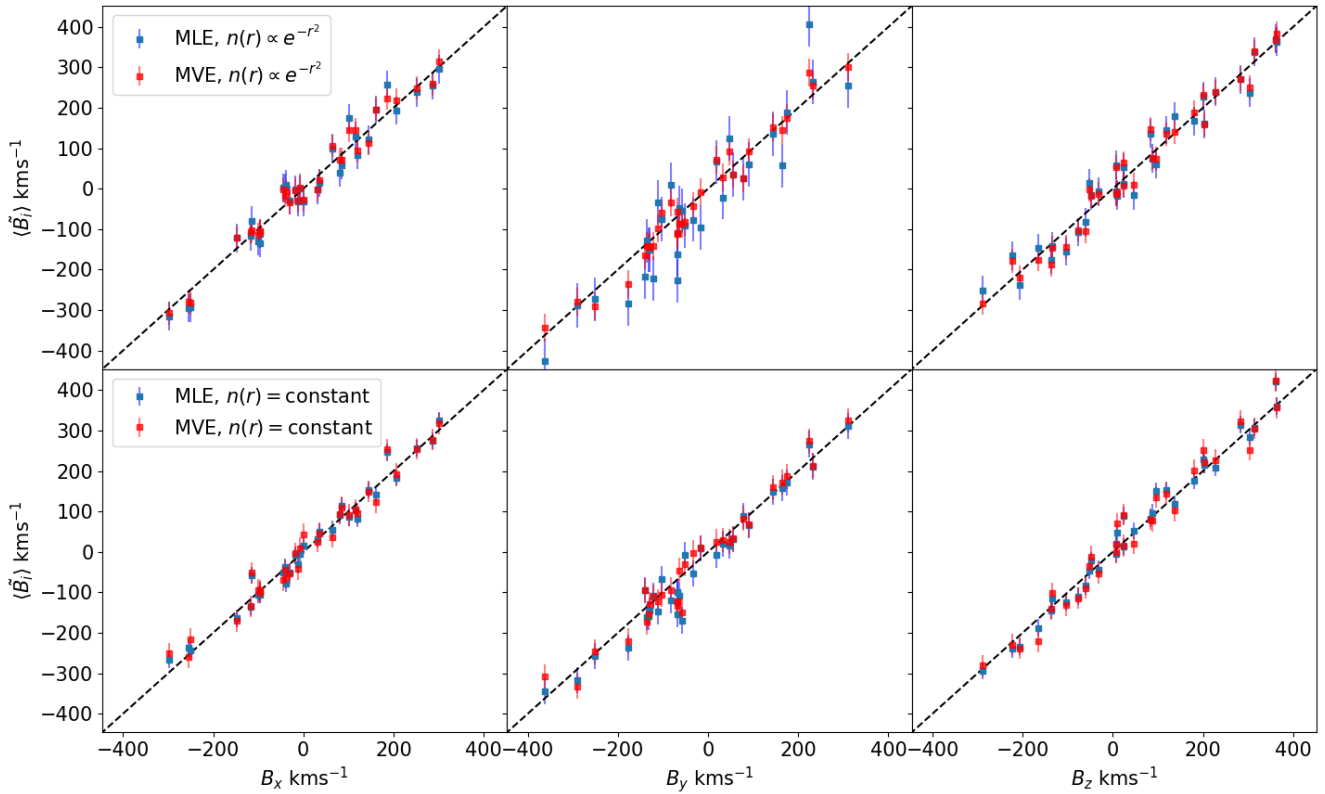


Figure 2: As for Figure 1 but with hemispherical mocks.

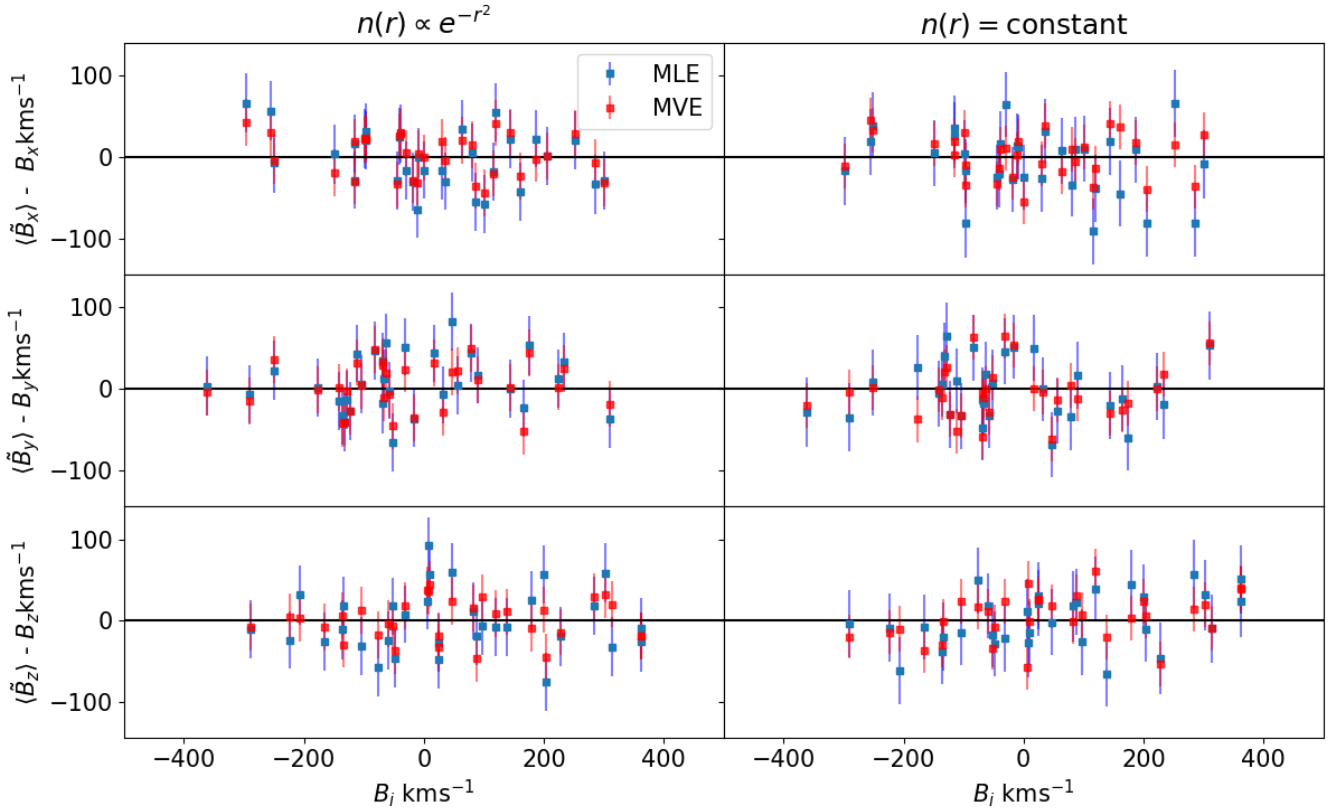


Figure 3: This plot shows the data as in Figure 1, but shows the residuals $\tilde{B}_i - B_i$ on the y axis.

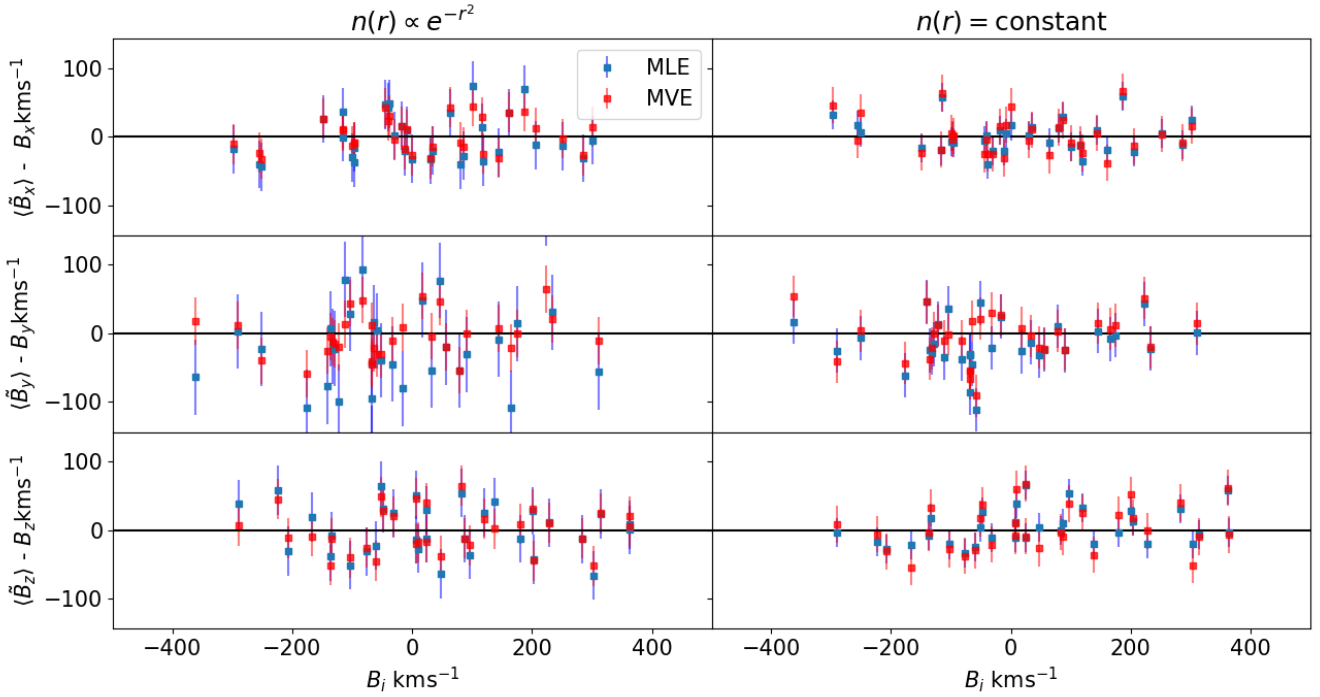


Figure 4: This plot shows the data as in Figure 2, but shows the residuals $\tilde{B}_i - B_i$ on the y axis.

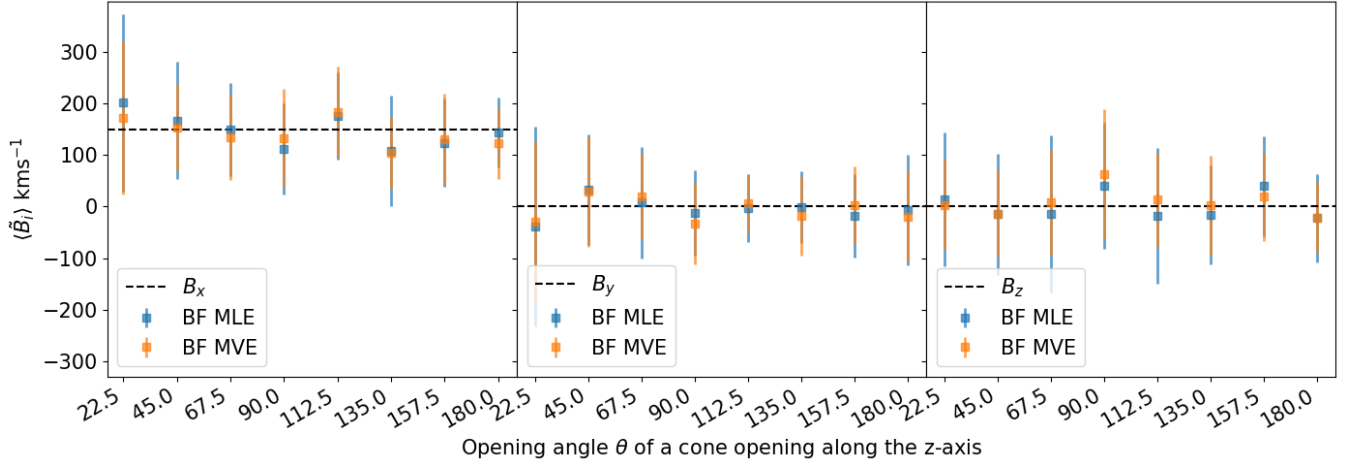


Figure 5: The averaged recovered bulk flow $\langle B_i \rangle$ component from simplistic mocks with a cone geometry. Each panel shows $\langle B_i \rangle$ in the x , y and z directions. The true \mathbf{B} is the same for each mock and the components are shown by the horizontal dashed line in each panel. Each point shows the average recovered bulk flows of 32 mocks with the same opening angle θ , plotted against θ ; $\theta = 180$ corresponds to a spherical survey, $\theta = 90$ corresponds to a hemisphere. For all the mocks the spatial distribution of objects follows a gaussian radial distribution such that $n(r) \propto e^{-r^2}$ with a standard deviation of $\sim 50 \text{Mpc h}^{-1}$ and each mock has 5000 objects. The recovered bulk flows from the MLE and the MVE methods (with 1500 objects for the ideal survey) are shown in blue and orange respectively. The error bars on each point represent the standard deviation of $\langle B_i \rangle$.

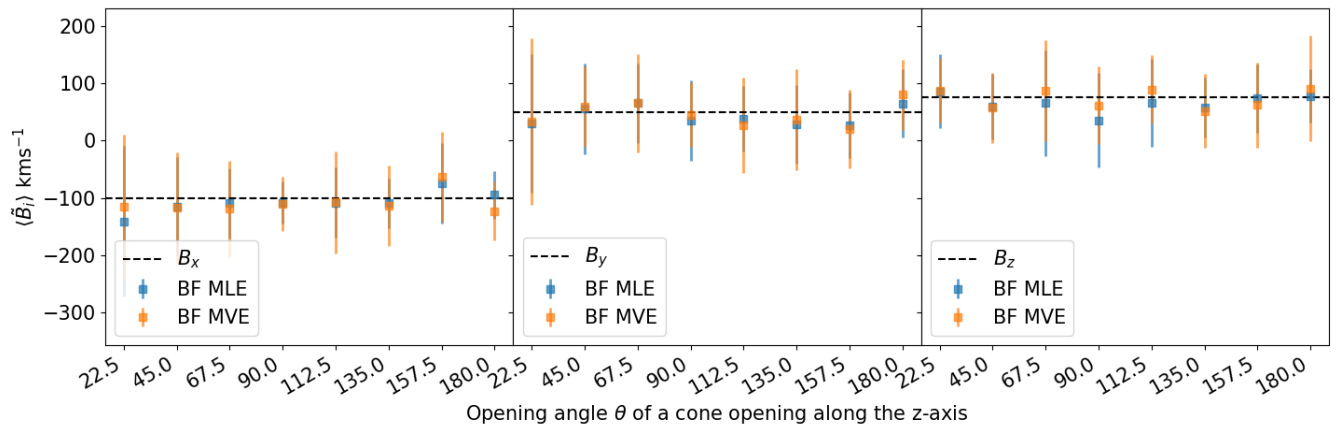


Figure 6: Same as Figure 5, but for mocks with a uniform rather than gaussian distribution of objects.

Applying the SDSS sky mask to the simplistic mocks

Here we apply the SDSS sky mask to the simplistic mocks using the MLE method, and likewise find that the goodness-of-fit is unaffected by the geometry in Figure 7 and 8.

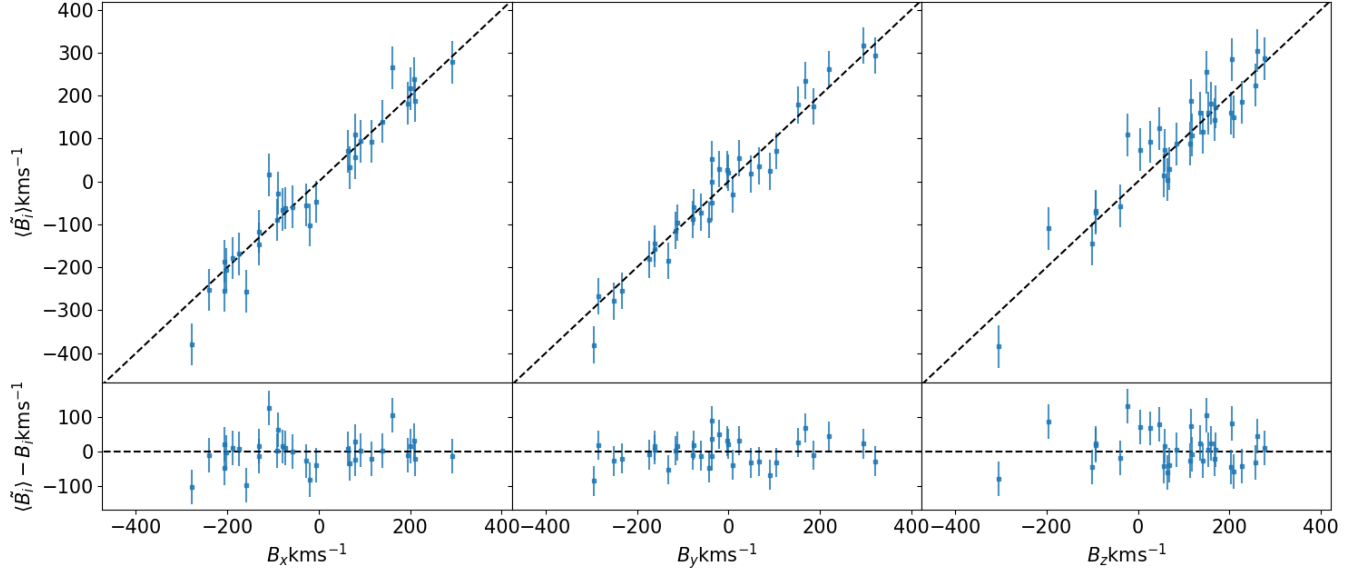


Figure 7: Recovered bulk flow components vs the real bulk flow components B_i for 256 simplistic mocks (constructed as described in the paper for the simplistic mocks with a gaussian radial geometry), each with 5000 objects before being sub-sampled for those that fall within the SDSS mask. Each point on this plot is an average of 16 different mocks but having the same net constant bulk flow \mathbf{B} added to the data in common. Here we have applied the Kaiser MLE. The top panels are results for the recovered estimates vs the truth while the bottom panel shows the residuals of the estimate from the truth.

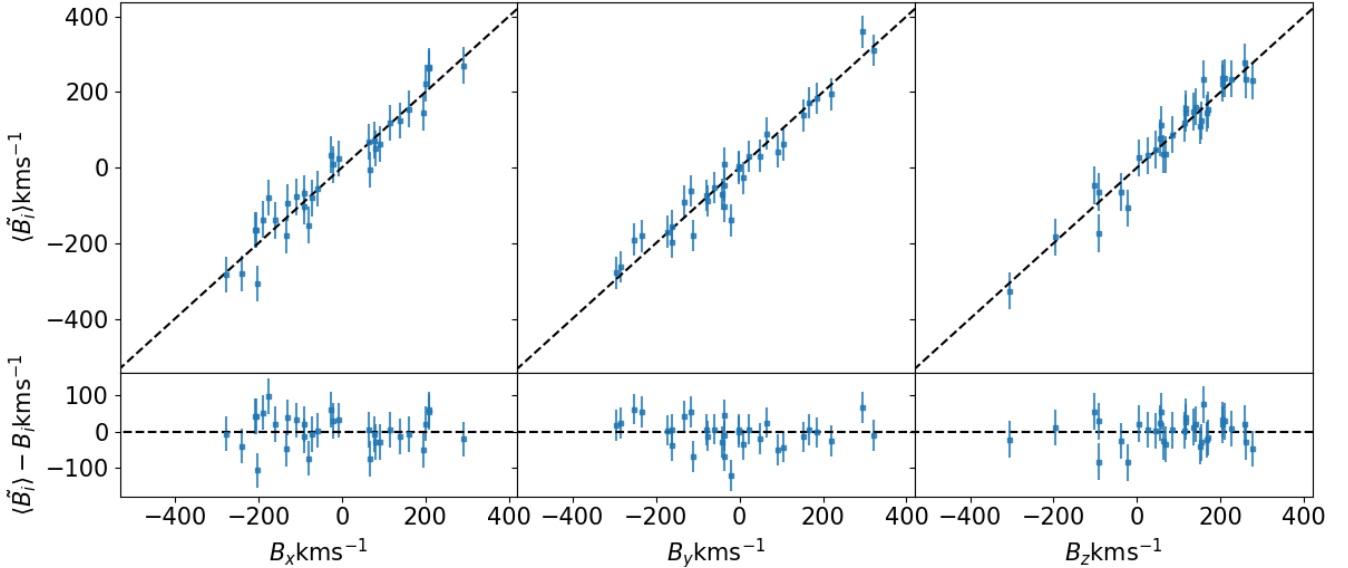


Figure 8: Same as in Figure 7 but for mocks with a $n(r) \propto r^{-2}$ radial distribution of objects.

Applying the Fundamental Plane fitting procedure to the simplistic mocks

Results from applying the selection effects of the SDSS sample (after assigning FP parameters) to fit the log-distance ratios of objects in the simplistic mocks, in Figure 9 for 256 mocks. This was in order to test whether the assumptions

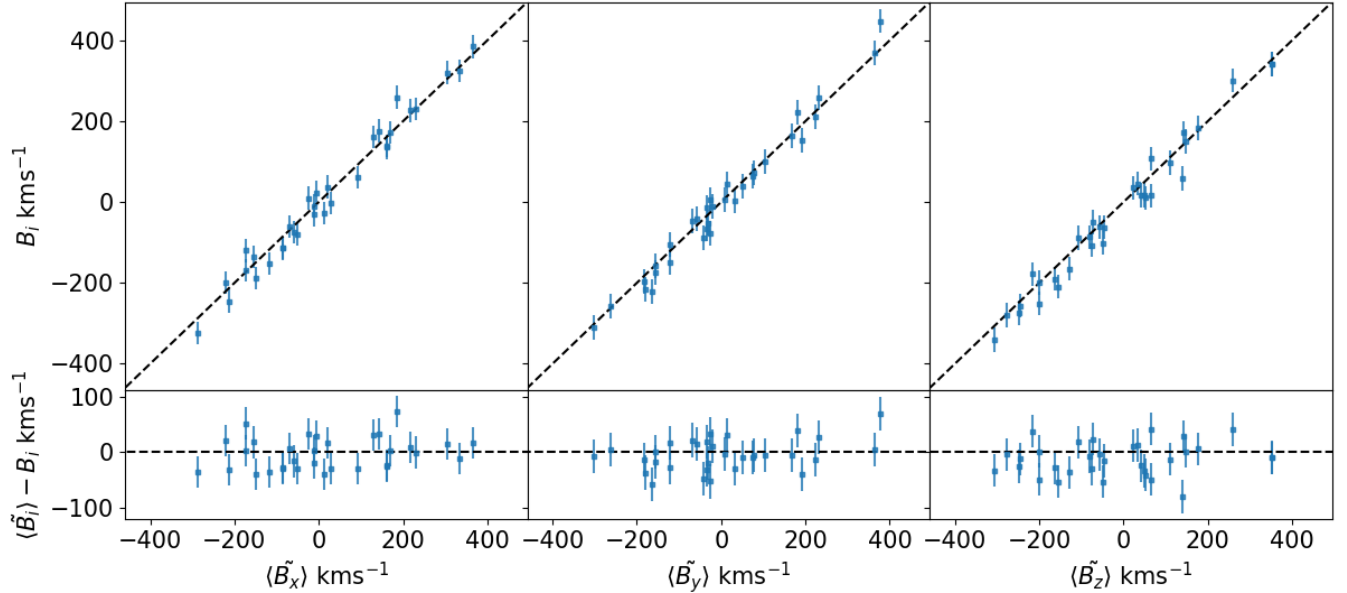


Figure 9: Recovered bulk flow components vs the real bulk flow components B_i for 256 simplistic mocks. Each mock is constructed with 10000 objects with a spherical sky mask and uniform radial selection function before being sub-sampled for the SDSS selection cuts and fitting the FP parameters to extract log-distance ratios. Each point on this plot is an average of 16 different mocks but having the same net constant bulk flow \mathbf{B} added to the data in common. The log-distance ratios used to compute the bulk flow using the Kaiser MLE procedure are recovered using the FP fitting procedure in Howlett et al., 2022.

behind the FP fitting procedure were causing the χ^2 to be greater than unity in general due to an error or assumptions incorporated in the analysis. However we found that we still obtain a reduced $\chi^2 \sim 1$ when applying the FP fitting procedure to the simplistic mocks, which validates the procedure and suggests it is not related to inaccuracy in the methods to extract peculiar velocities from the Fundamental Plane relation.

Conclusions from tests on simplistic mocks

- For the simplistic mocks both the MLE and MVE are able to obtain an unbiased estimate of \mathbf{B} with a $\chi^2 \sim 1$ (this is calculated from the individual bulk flows measured for each mock before averaging the results as shown in the plots).
- The performance of the estimators is thus to a reasonable level of precision, such that the error bars represent the uncertainty in the bulk flow well, regardless of the survey selection function, for these simplistic mocks.
- The methods used in Howlett et al., 2022 (and other works who follow a similar approach) in order to recover the FP (Fundamental Plane) parameters are validated, and the methods used are not related to issues with precision regarding bulk flow estimates.
- The irregular sky mask for the SDSS survey is not a related factor to any issues regarding the precision of bulk flow estimates, because with the simplistic mocks we obtain an unbiased bulk flow estimate using these methods, even when we have applied the SDSS sky mask to them, giving them a more complex survey geometry.

Tests on Zeldovich mocks

SDSS mocks with Zeldovich approximation

Here we show results when applying the Kaiser MLE method to realistic SDSS mocks (including all selection effects) but without non-linear structure growth, by generating the simulated positions and velocities of galaxies using the Zeldovich approximation. In Figure 10 the results are unbiased for the bulk flow estimate but the independently calculated reduced χ^2 for each bulk flow mode is approximately 6.4, 4.3, 9.8. This implies that removing the non-linear structure growth from the realistic SDSS mocks (by comparing these results to those in Howlett et al., 2022) did not improve the bulk flow fit. The changing in the distribution of velocities due to non-linear structure growth thus does not appear to be related to the precision of the Kaiser MLE method to estimate the bulk flow. In Figure 11, the shear modes of the velocity field are included in the modelling. The results are also unbiased, and the scatter in the measurements slightly increases. The individually calculated reduced χ^2 for each bulk flow mode is 8.6, 4.7, 6.5. Including the modelling for the additional modes has little effect on the overall goodness-of-fit.

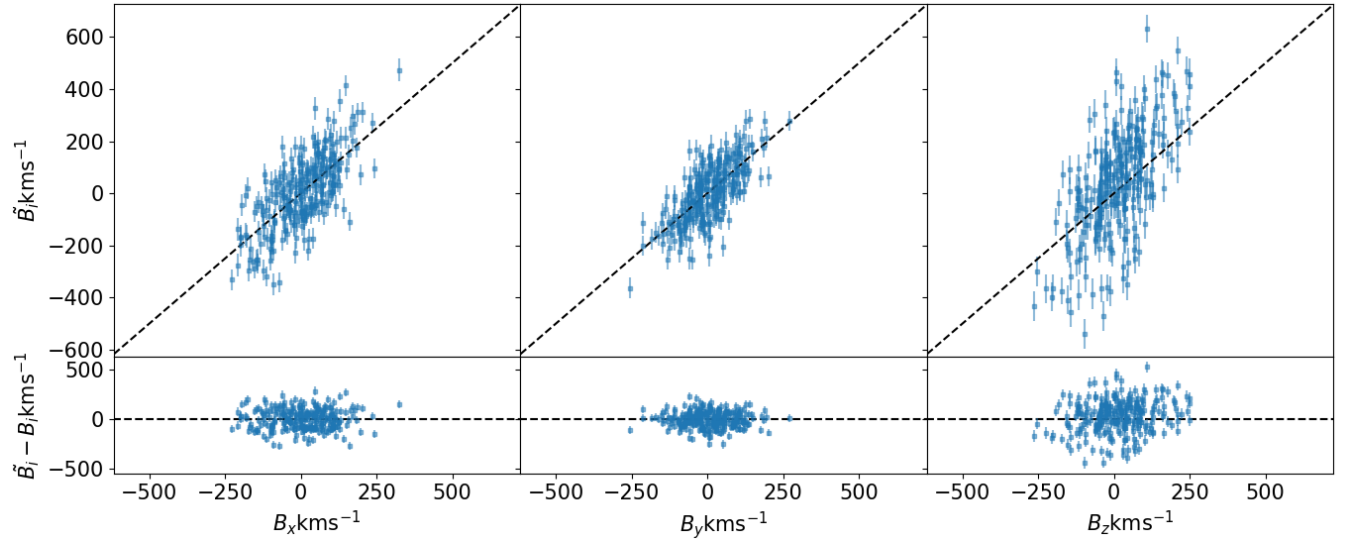


Figure 10: Recovered bulk flow using the Kaiser MLE approach for 256 SDSS mocks that do not contain non-linear structure growth (the simulated galaxy positions and velocities come from the Zeldovich approximation). In this analysis only the bulk flow modes are included in the modelling.

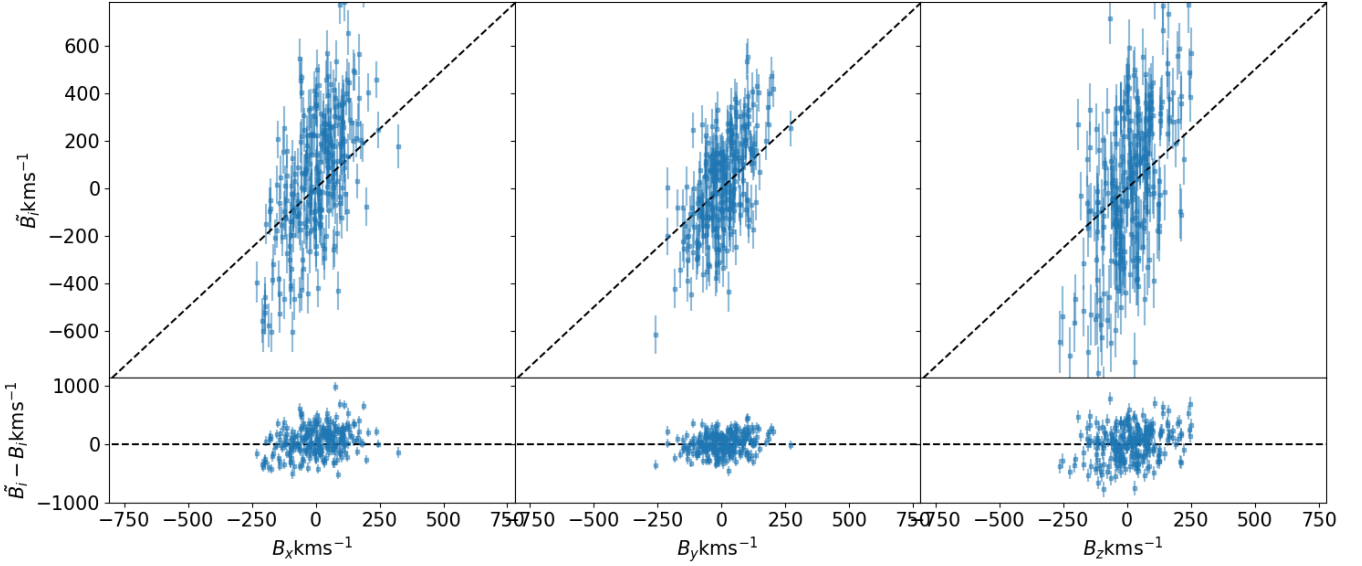


Figure 11: Recovered bulk flow using the Kaiser MLE approach for 256 SDSS mocks that do not contain non-linear structure growth (the simulated galaxy positions and velocities come from the Zeldovich approximation). In this analysis the bulk flow and shear modes are included in the modelling.

MLE tests with varying geometry in Zeldovich mocks, 34000 objects

We produce more general zeldovich mocks with 34000 galaxies in each mock.

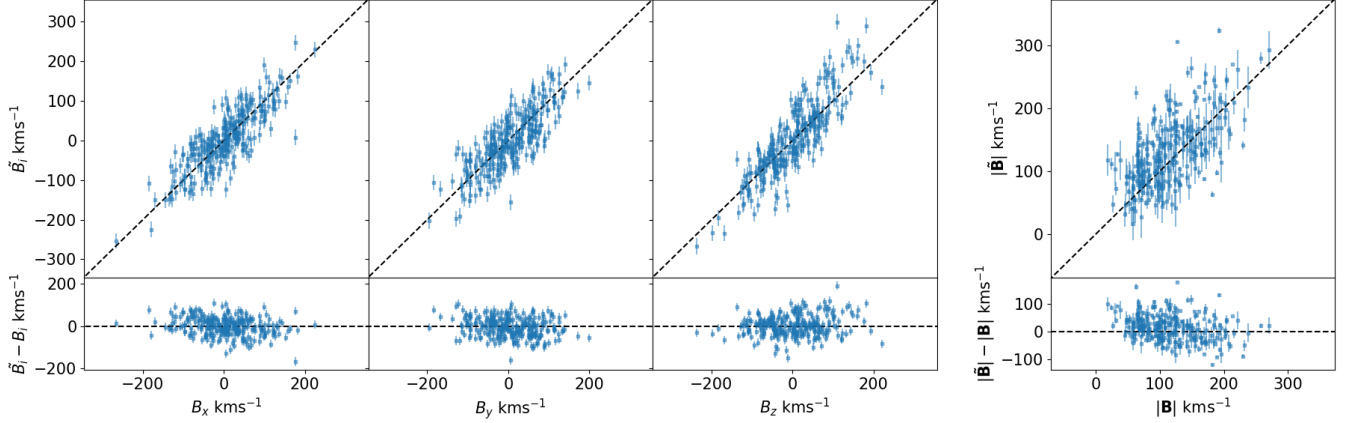


Figure 12: Recovered bulk flow using the Kaiser MLE approach for 256 Zeldovich mocks with approximately 34000 objects. The geometry has a spherical sky mask and a uniform radial selection function. The last panels show the bulk flow amplitude compared to the true amplitude.

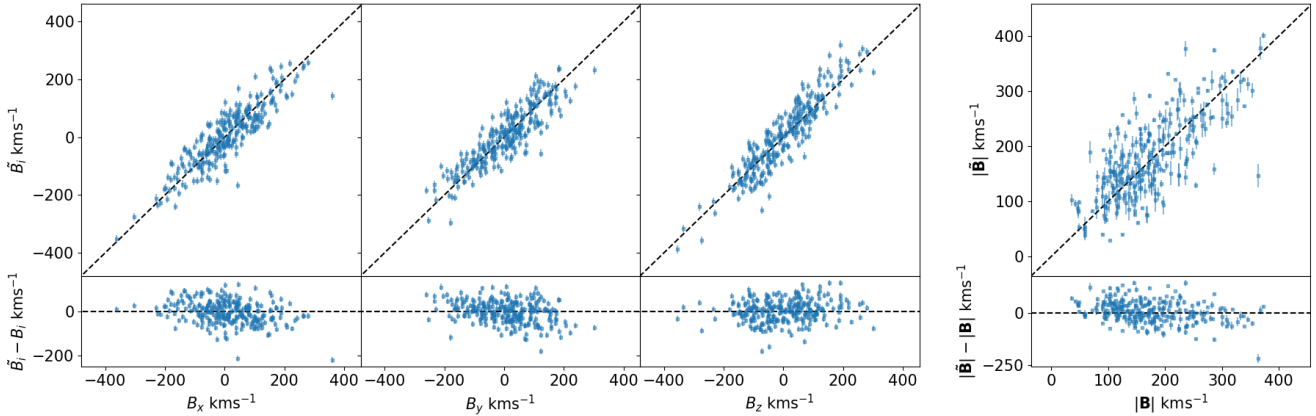


Figure 13: The same as in Figure 12, but for mocks with a gaussian radial selection function.

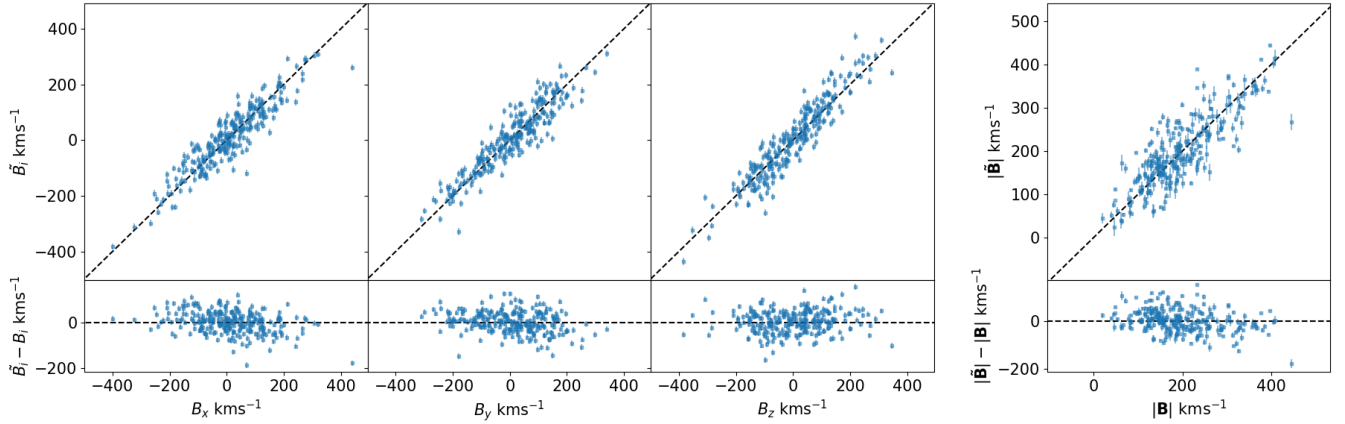


Figure 14: The same as in Figure 12, but for mocks with a selection function that has $n(r) \propto r^{-2}$.

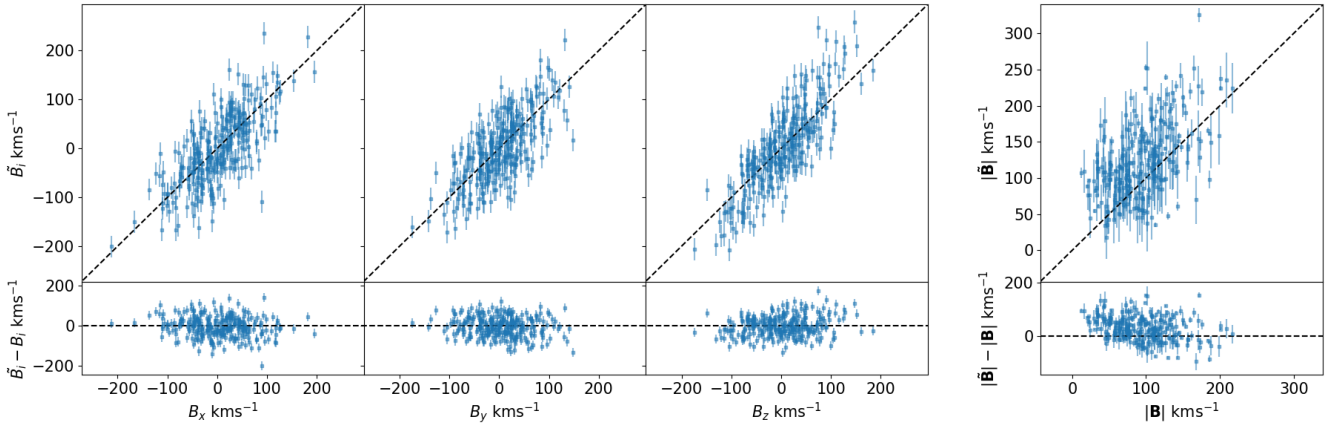


Figure 15: The same as in Figure 12, but for mocks with a selection function that has $n(r) \propto r^1$.

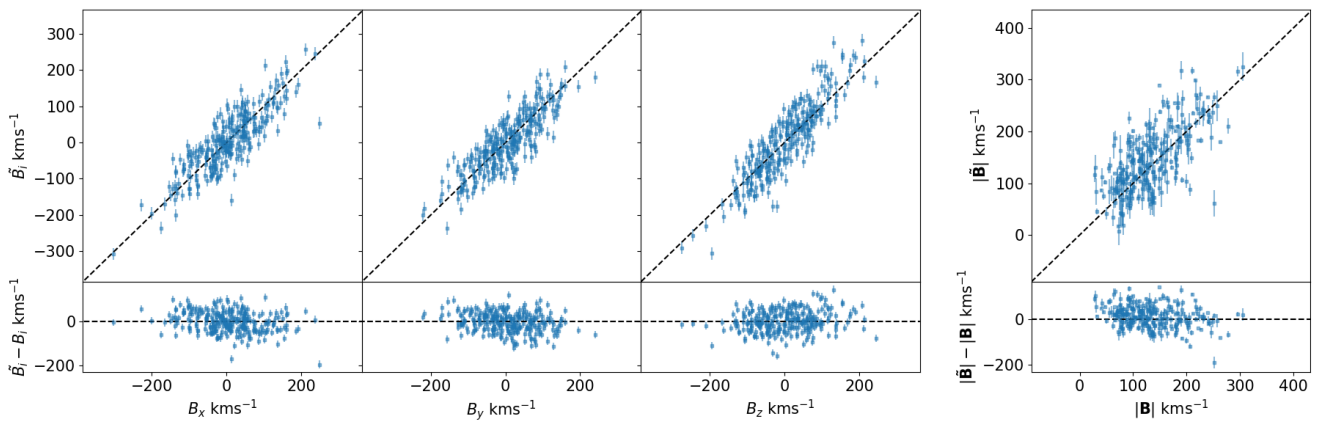


Figure 16: The same as in Figure 12, but for mocks with the radial selection function of the SDSSv mocks.

For each set of mocks tested and shown in Figures 12, 13, 14, 15, 16 the reduced χ^2 for the goodness-of-fit for the recovered bulk flow to the truth varies, but there does not seem to be any significant biases in general with different geometries. The χ^2 appears to be correlated with properties of the survey geometry. This is demonstrated by Figures 17 and 18.

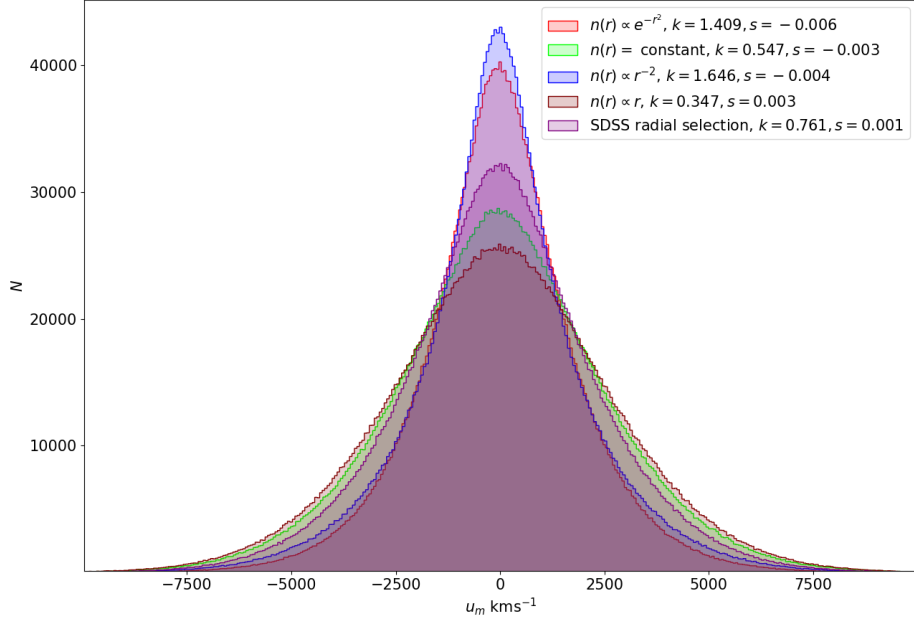


Figure 17: The distribution of observed radial peculiar velocities in the Zeldovich mocks with varying radial selection functions used to downsample the mocks to approximately 34000 galaxies. In the legend the functional form of the selection function of the mocks is indicated along with the calculated excess sample kurtosis k of the distribution from a gaussian distribution and the skewness s of the distribution. For all mocks the observed velocities plotted are estimated using a transformation by Watkins et al (2015) that gaussianizes the individual PV PDFs when they are calculated from the log-distance ratios that are observed. For each set of mocks the uncertainty on each log-distance ratio is a constant value. While the PV estimator is unbiased as an estimator, the estimate depends on both η and cz and thus the spread (and thus kurtosis) of the observed radial velocity distributions are altered by the selection function of the mock survey.

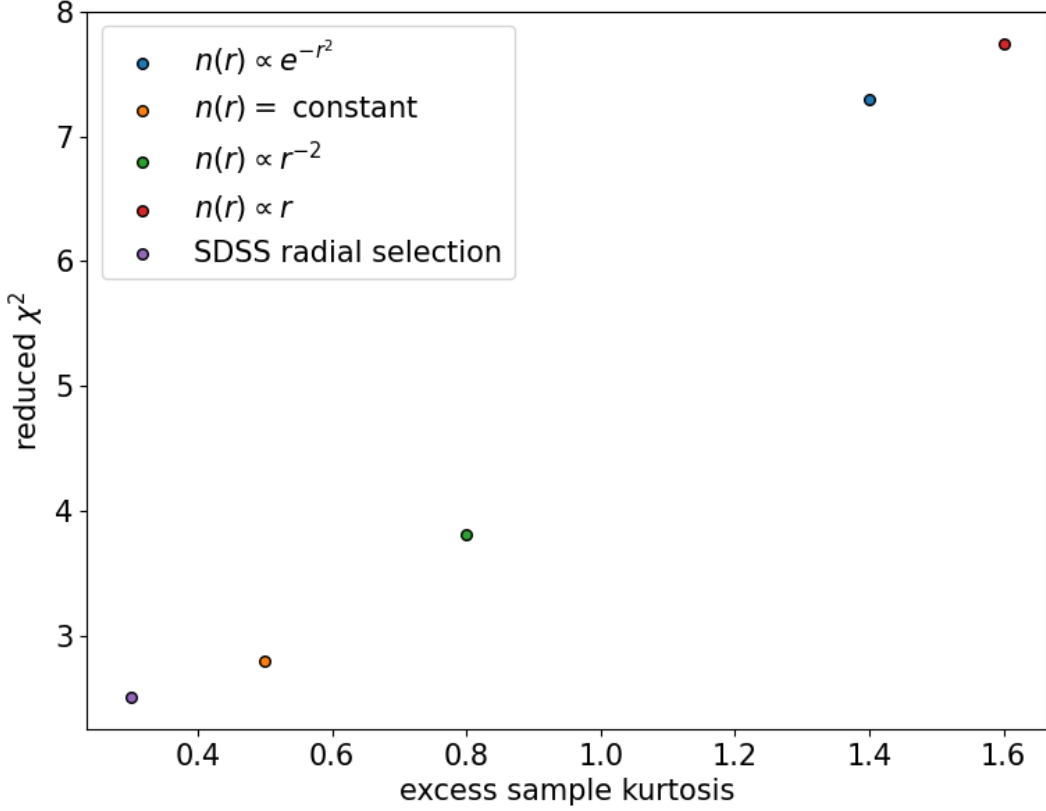


Figure 18: Correlation between the reduced χ^2 of each fit for the recovered bulk flows to the true bulk flows for sets of mocks with results shown in Figures 12, 13, 14, 15, 16 and the kurtosis of each observed velocity distribution for these geometries, shown in Figure 17.

Figures 19, 20, 21, 22, 23 show the same results as in Figures 12, 13, 14, 15, 16, but when applying the Nusser MLE approach instead of the Kaiser MLE. In the plots here for the Nusser MLE, the error shown on the bulk flow moments are exact, but for the bulk flow amplitude in the panels furthest to the right the error bars are given by approximating the correlations between the bulk flow moments as zero (which makes only a small difference to the error bars visually and we have not used this approximation in our χ^2 calculations).

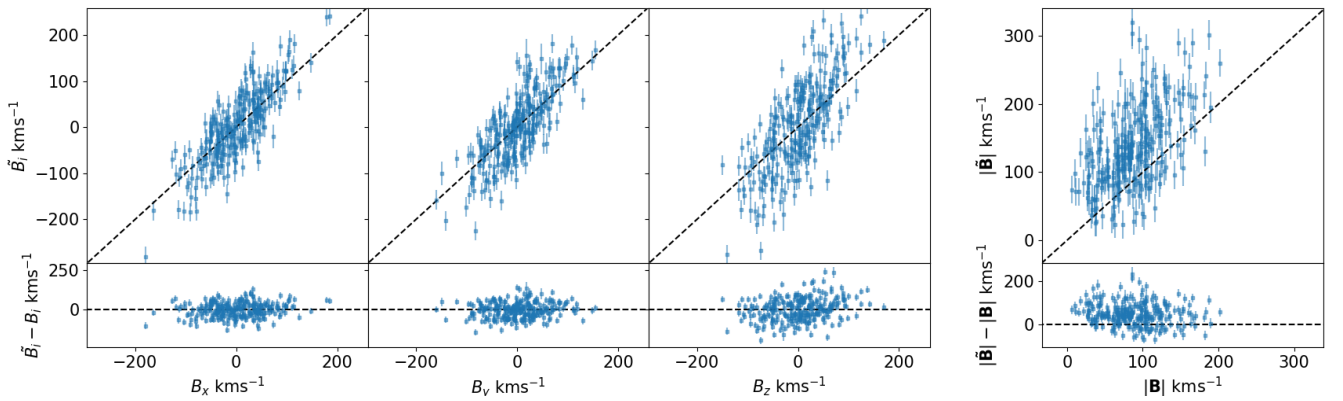


Figure 19: Recovered bulk flow using the Nusser MLE approach for 256 Zeldovich mocks with approximately 34000 objects. The geometry has a spherical sky mask and a uniform radial selection function. The last panels show the bulk flow amplitude compared to the true amplitude.

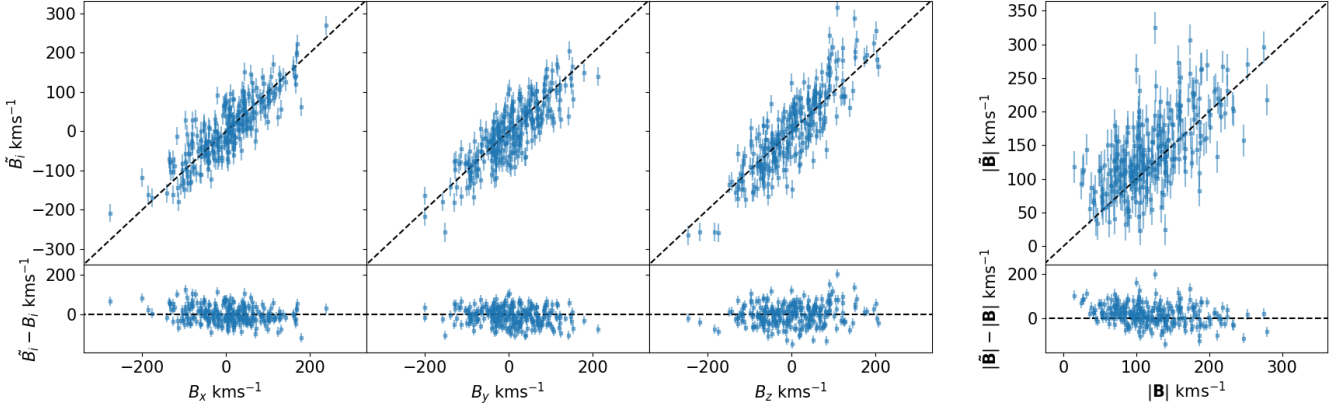


Figure 20: The same as in Figure 19, but for mocks with a gaussian radial selection function.

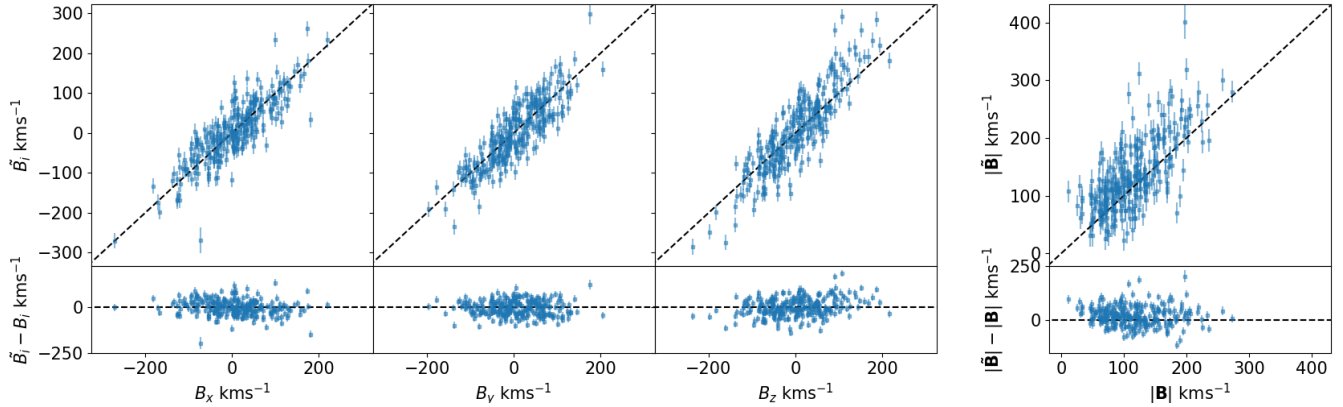


Figure 21: The same as in Figure 19, but for mocks with a selection function that has $n(r) \propto r^{-2}$.

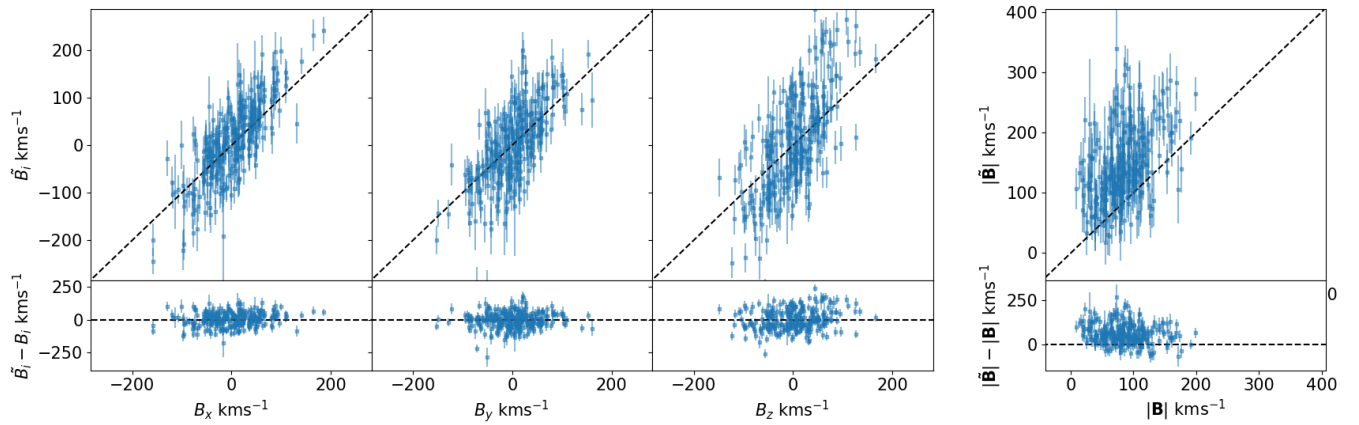


Figure 22: The same as in Figure 19, but for mocks with a selection function that has $n(r) \propto r^1$.

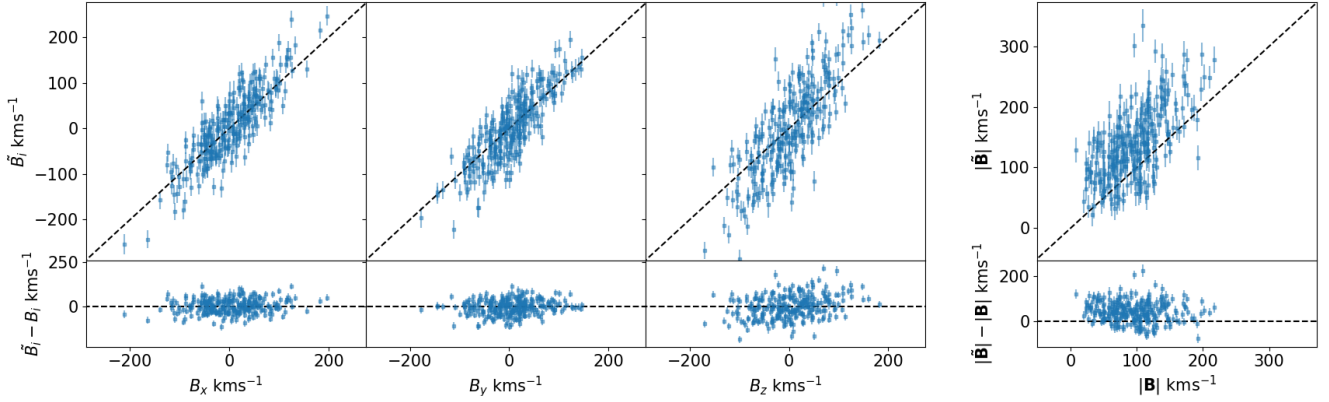


Figure 23: The same as in Figure 19, but for mocks with the radial selection function of the SDSSv mocks.

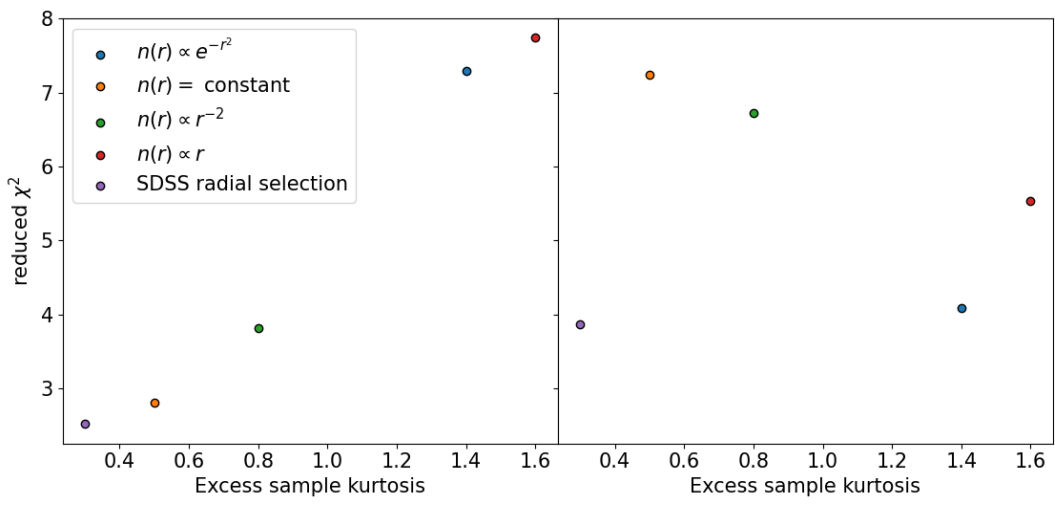


Figure 24: Left panel: Results shown in Figure 18. Right panel: the same, but for the results shown in Figures 19, 20, 21, 22, 23 using the Nusser MLE.

MLE and MVE tests on Zeldovich mocks with varying geometry, 5000 objects

In all calculations, the results for 256 mocks each have 5000 objects, the ideal survey has 1500 objects, the value for $\sigma_* = 300 \text{ kms}^{-1}$.

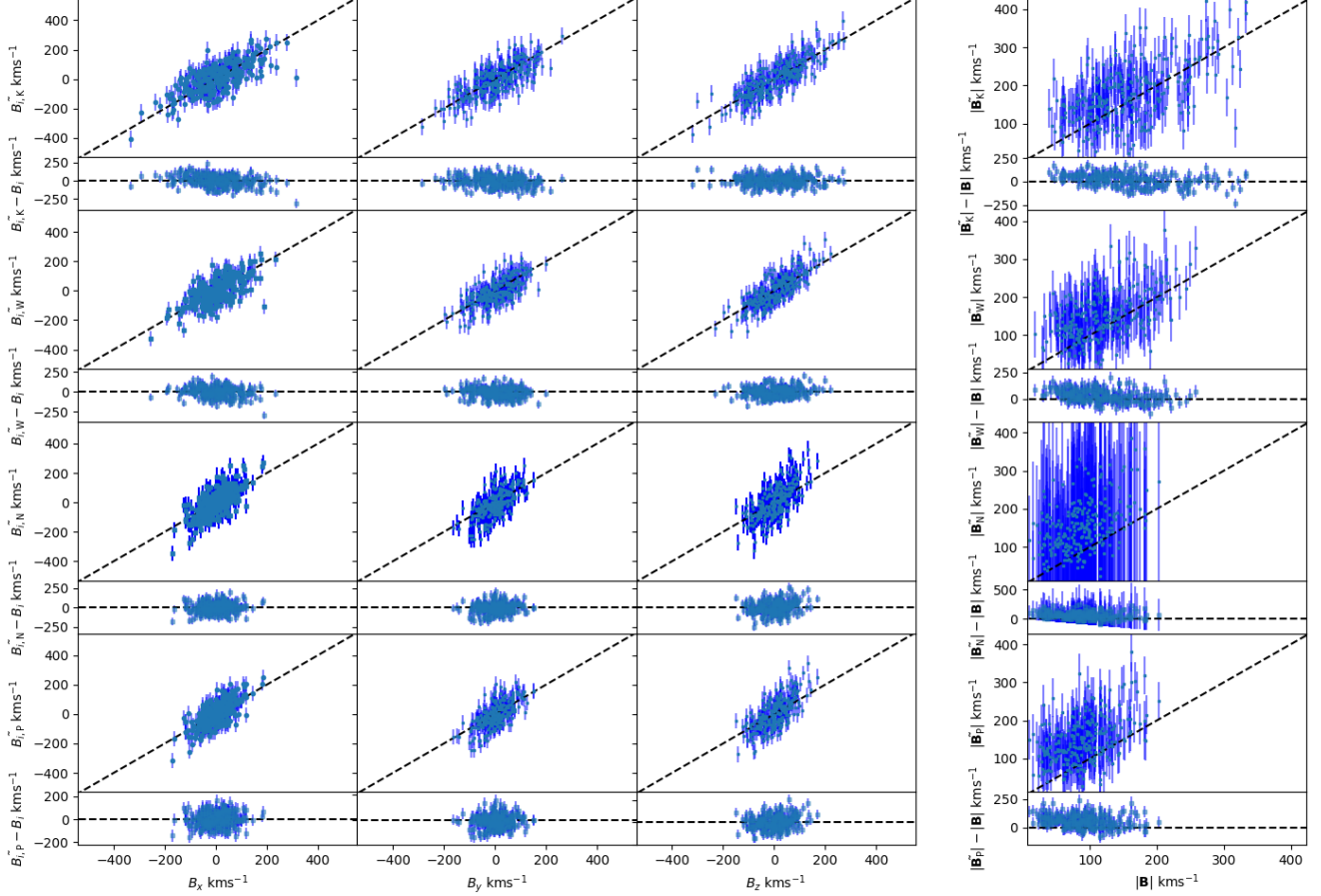


Figure 25: Recovered bulk flows from applying the Watkins MVE (top panels), the Kaiser MLE (second row), the Nusser MLE (third row) and the Peery MVE (last row) to spherical mocks with a uniform radial distribution of objects. From left to right shows the results for each coordinate direction and then the bulk flow amplitude and residuals are also shown. It should be noted that in each case, depending on the estimator the definition of the truth bulk flow varies. For each estimator the reduced χ^2 is 2.3, 1.8, 1.9 and 1.7.

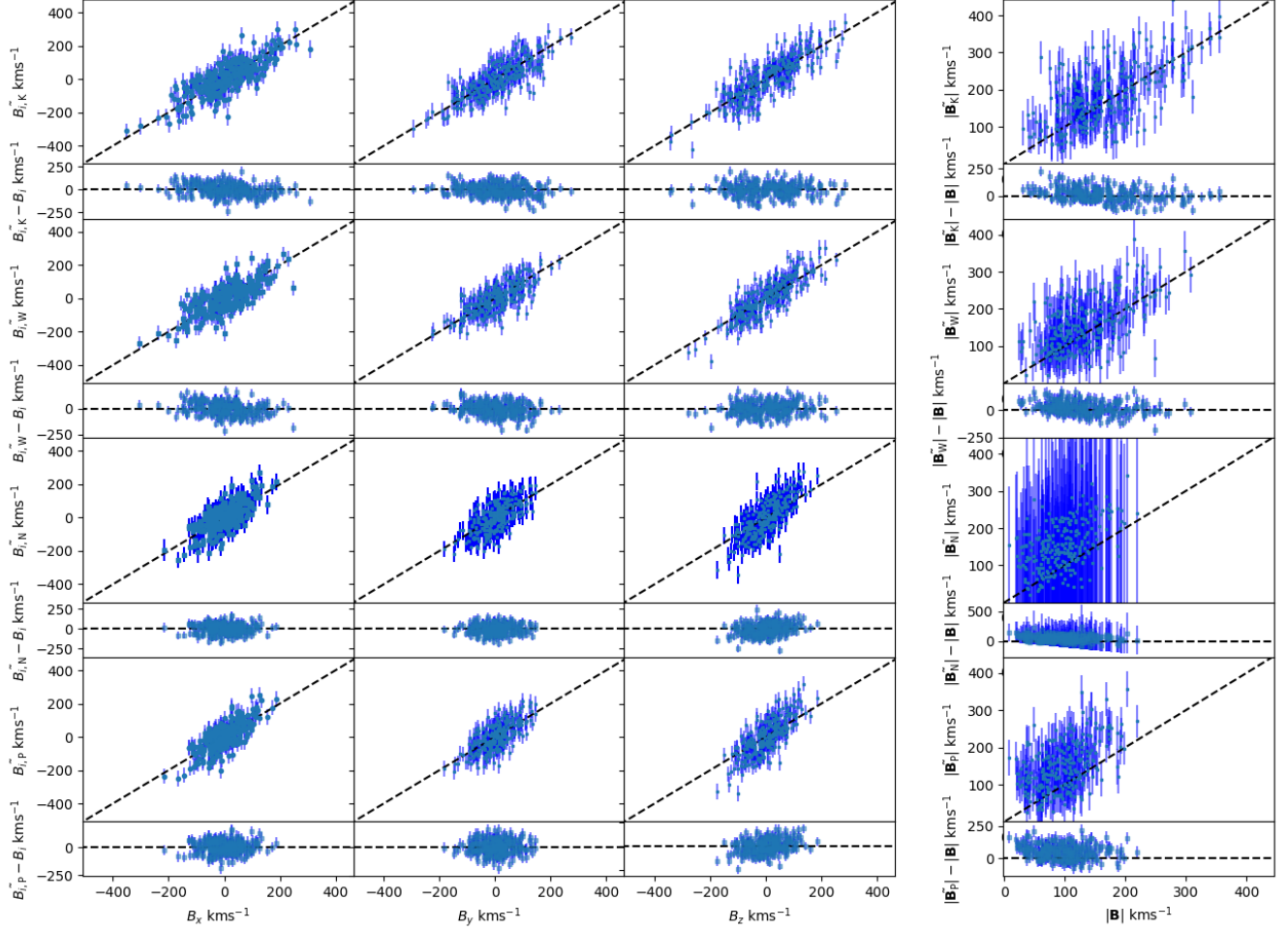


Figure 26: Recovered bulk flows from applying the Watkins MVE (top panels), the Kaiser MLE (second row), the Nusser MLE (third row) and the Peery MVE (last row) to spherical mocks with a distribution of objects that follows the SDSS selection function. From left to right shows the results for each coordinate direction and then the bulk flow amplitude and residuals are also shown. It should be noted that in each case, depending on the estimator the definition of the truth bulk flow varies. For each estimator the reduced χ^2 is 2.8, 2.2, 1.8 and 1.9.

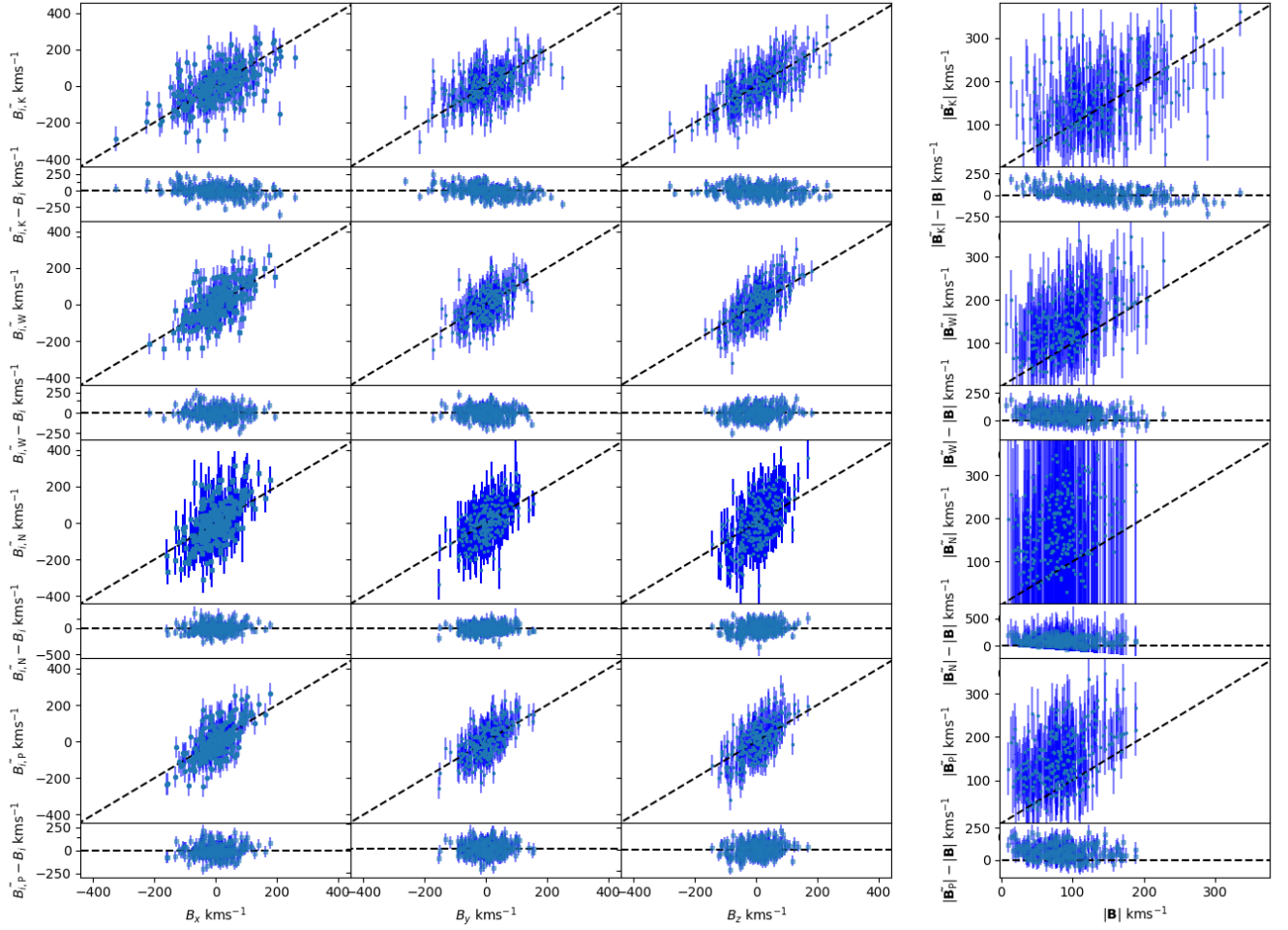


Figure 27: Recovered bulk flows from applying the Watkins MVE (top panels), the Kaiser MLE (second row), the Nusser MLE (third row) and the Peery MVE (last row) to spherical mocks with a distribution of objects that follows $n(r) \propto r^1$. From left to right shows the results for each coordinate direction and then the bulk flow amplitude and residuals are also shown. It should be noted that in each case, depending on the estimator the definition of the truth bulk flow varies. For each estimator the reduced χ^2 is 1.5, 1.5, 1.4 and 1.5.

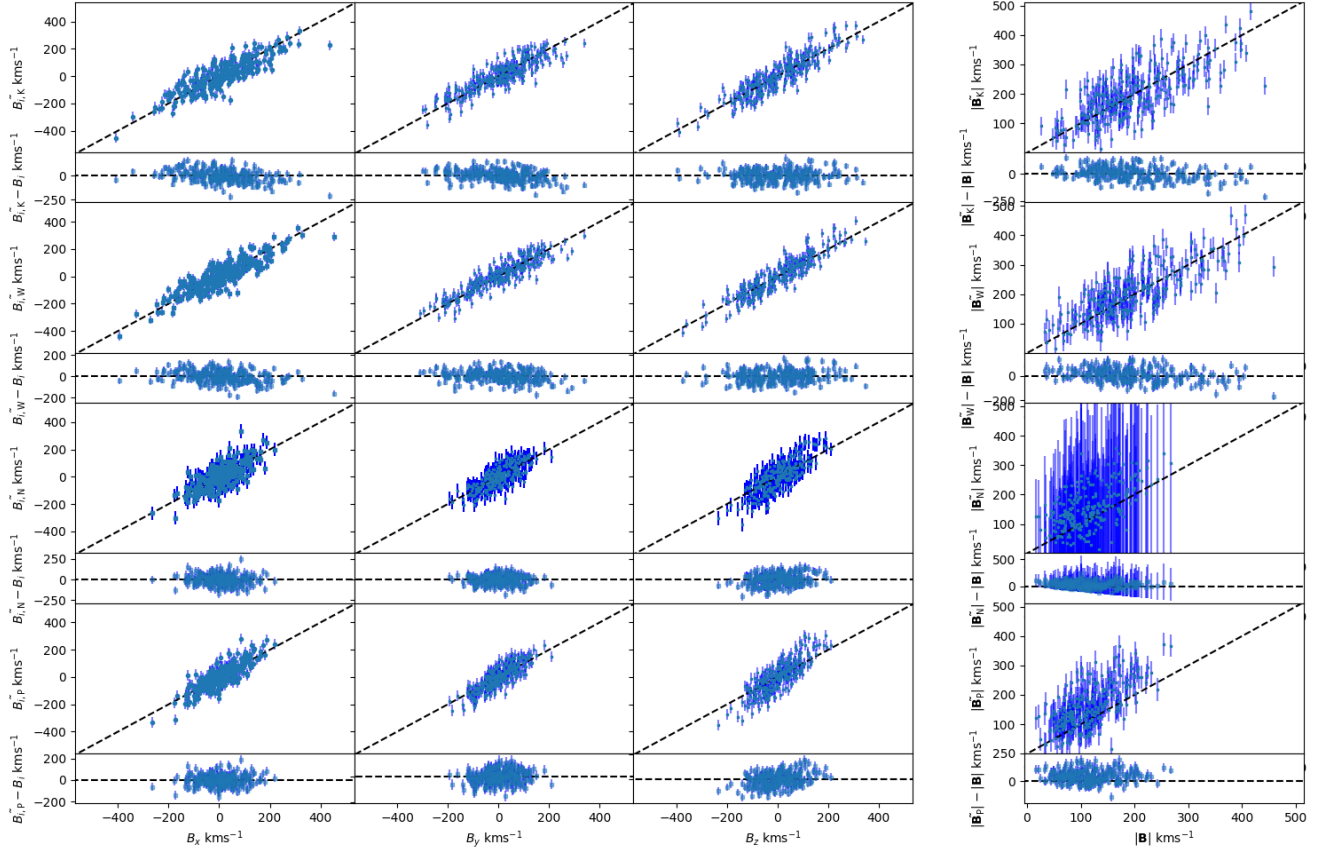


Figure 28: Recovered bulk flows from applying the Watkins MVE (top panels), the Kaiser MLE (second row), the Nusser MLE (third row) and the Peery MVE (last row) to spherical mocks with a distribution of objects that follows $n(r) \propto r^{-2}$. From left to right shows the results for each coordinate direction and then the bulk flow amplitude and residuals are also shown. It should be noted that in each case, depending on the estimator the definition of the truth bulk flow varies. For each estimator the reduced χ^2 is 5.2, 6.5, 1.6 and 2.2.

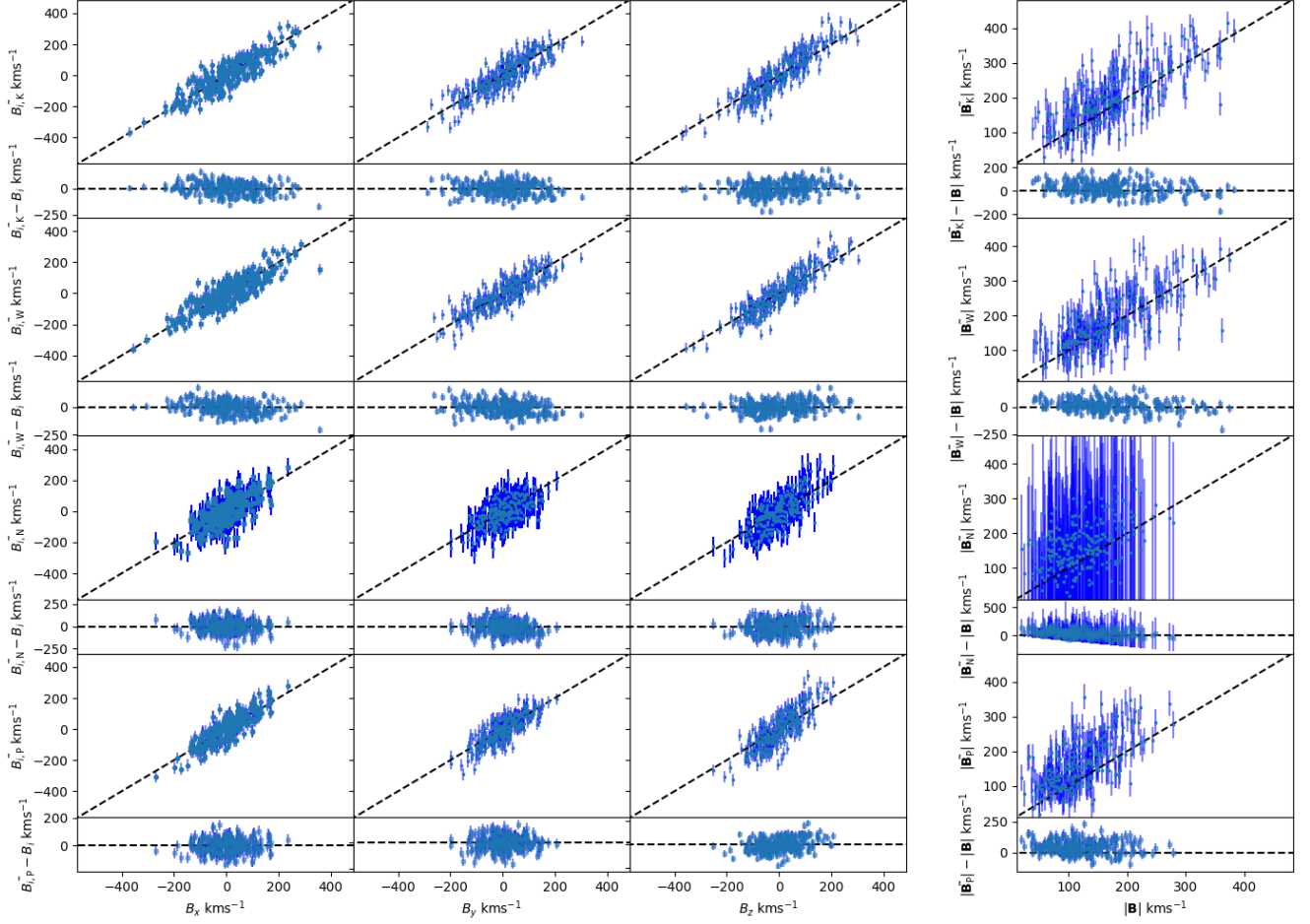


Figure 29: Recovered bulk flows from applying the Watkins MVE (top panels), the Kaiser MLE (second row), the Nusser MLE (third row) and the Peery MVE (last row) to spherical mocks with a gaussian radial distribution of objects. From left to right shows the results for each coordinate direction and then the bulk flow amplitude and residuals are also shown. It should be noted that in each case, depending on the estimator the definition of the truth bulk flow varies. For each estimator the reduced χ^2 is 4.9, 4.5, 1.4 and 2.5.

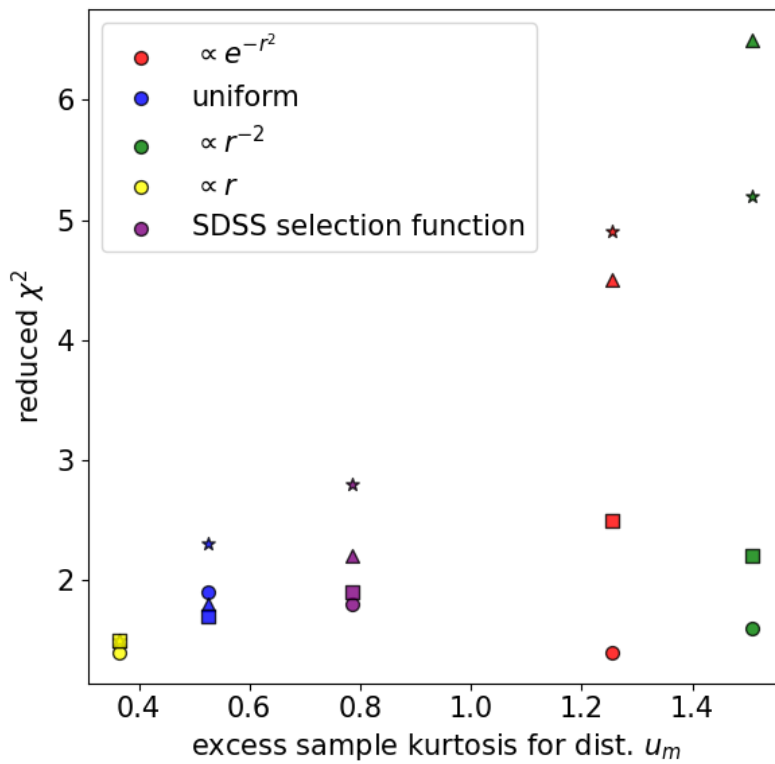


Figure 30: Results showing the trend between the reduced χ^2 from fitting the recovered bulk flows to the true bulk flows in Figures 25, 26, 27, 28 and 29 vs kurtosis of the observed velocity distribution for the mocks. The triangles show the results for the Kaiser MLE applied to the mocks, the circles for the Nusser MLE, the stars for the Watkins MVE and the squares for the Peery MVE. The colors of the markers correspond to the legend which shows the radial selection function of the mocks.

Conclusions from tests with Zeldovich mocks:

- The assumption of a constant bulk flow across the volume of a survey (which is generally not true) affects the precision of the Kaiser MLE and the Peery MVE.
- This magnitude of this effect is strongly dependent on survey geometry.
- In the case of a spherically symmetric selection function/survey geometry, the Nusser MLE approach and the updated MVE approach in Peery et al (2018) corrects for this assumption and provides a more precise estimate of the bulk flow modes, although it is clear in some cases that the bulk amplitude can appear to be larger than expected with these methods, because you may be more likely to find an overestimated bulk flow amplitude in general due to the fact the amplitude takes an absolute value when squared.

Tests on realistic mocks for CosmicFlows–4

Initial application of BF estimators to CF4 mocks

Results from initial application of three bulk flow estimators to the CF4 mock data (512 mocks). The results are presented in arbitrary coordinates. The mocks contain approximately 50,000 objects that capture the geometry and selection effects of the real data. The Nusser estimator clearly overestimates the bulk flow and is biased, likely due to the fact the real CF4 data does not have the spherical symmetry that is assumed in the derivation for the method. The Kaiser estimator appears to give the best correlation between the true bulk flow and the recovered bulk flow, although both the Kaiser MLE and the Peery MVE slightly underestimate the bulk flow compared to the truth. The Peery estimator obtains the best fit with a reduced $\chi^2 \sim 3.4$, the Kaiser estimator obtains $\chi^2 \sim 23$, the error bars are significantly underestimated. Although the Nusser estimator obtains $\chi^2 \sim 1.3$, it is clear that the results are poorly correlated with the truth and appear to have a significant bias, such that this doesn't indicate a good fit to the true bulk flows of the mocks. All estimator results here have a slight bias, but the Peery MVE appears to have the least bias when applied to mocks. Possibly this is because unlike the Kaiser estimator, the Peery method involves less assumptions about the nature of the survey geometry or peculiar velocity field that could create systematics in the results. While this is also true for the Nusser MLE, the Nusser MLE like the Kaiser MLE neglects correlations between PVs and assumes spherical symmetry in the number density of objects across the survey volume. For the purpose of the initial test with the Peery estimator, we choose the ideal survey to have a radius of $345 \text{ Mpc} h^{-1}$ and 10000 objects in the ideal survey. In this plot, the error shown on the bulk flow moments are exact, but for the bulk flow amplitude shown in the panels in the column furthest to the right the error bars are given by approximating the correlations between the bulk flow moments as zero (which makes only a small difference to the error bars visually and we have not used this approximation in our χ^2 calculations). In all following plots, the error on the bulk flow amplitude is given exactly.

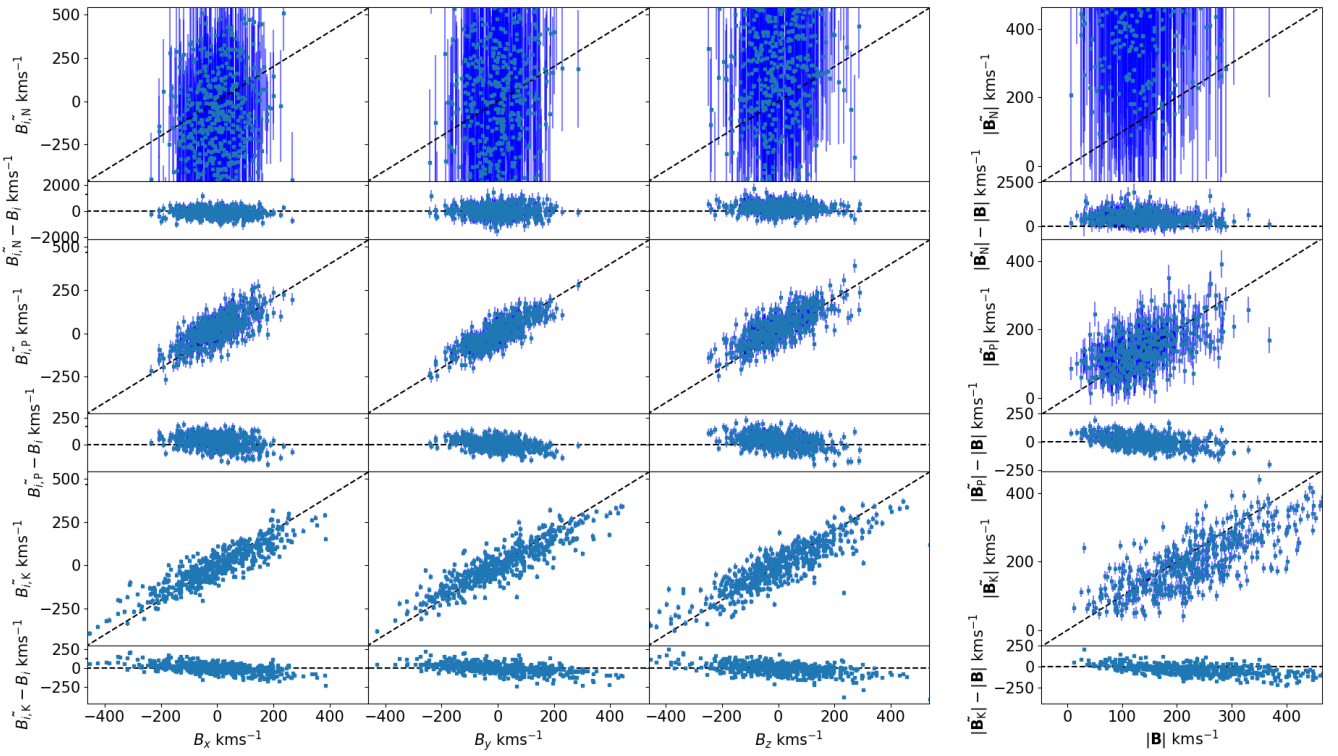


Figure 31: Recovered bulk flows from 512 realistic mocks for the CF4 catalogue. The top panels show results from the Nusser MLE, then the second row of panels shows the Peery MVE, and finally the last row shows the Kaiser MLE.

Peery MVE Results with CF4 mocks: varying ideal survey radius

Here we show results for the CF4 mocks again, but with the Peery estimator applied with 10,000 objects in the ideal survey and where results are given for varying choices of the ideal survey radius. The results are given in Supergalactic coordinates. We also show results when the true PVs of each galaxy have been used rather than the observations with non-zero uncertainties, to investigate the performance on the estimator further.

In general the results indicate the performance of the Peery estimator works better for this dataset for an ideal survey with larger radii of at least 170 Mpc h^{-1} given the χ^2 , but there is a bias that results in a slightly underestimated bulk flow (see the linear regression in each plot) which is present at all choices of ideal survey radii. The reduced χ^2 goodness of fit improves with increasing size of the ideal survey radius. For each radii shown in ascending order the χ^2 for the fit between the mocks bulk flow and true bulk flow is 6.78, 6.51, 5.07, 4.23, 3.78, 3.54, 3.43, 3.39, 3.39, 3.39.

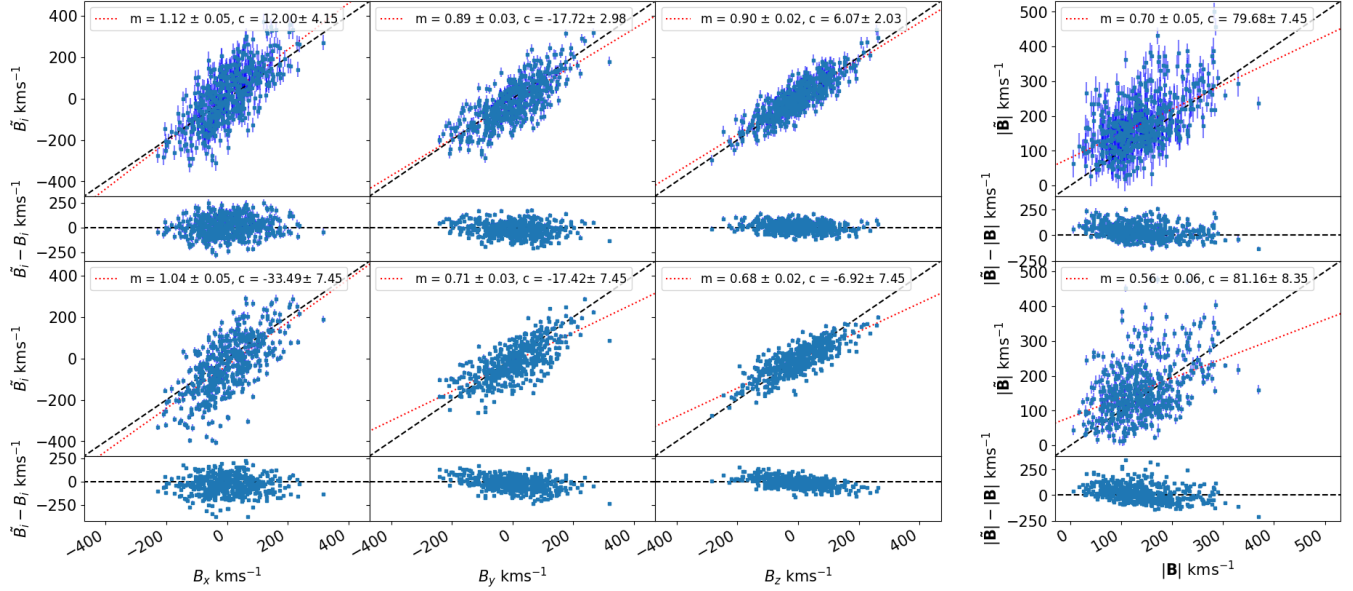


Figure 32: Results from applying the Peery estimator with an ideal survey of radius 69 Mpc h^{-1} . The top rows show the results when using the observed log-distance ratios for the estimator, the bottom panel for the true PVs with zero uncertainty. The red dashed line in the panel for the amplitude measured gives the gradient m and y-intercept c for a linear regression to the data.

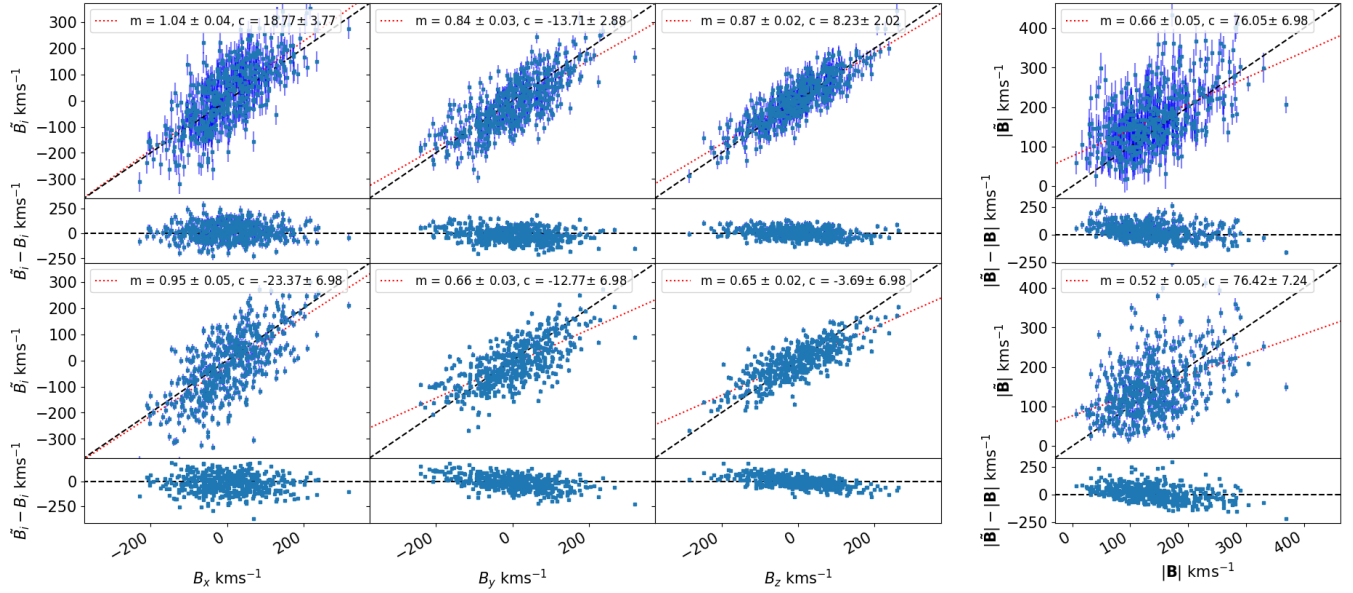


Figure 33: Same as in Figure 32, with where the ideal survey has a radius of $\sim 100 \text{ Mpc } h^{-1}$.

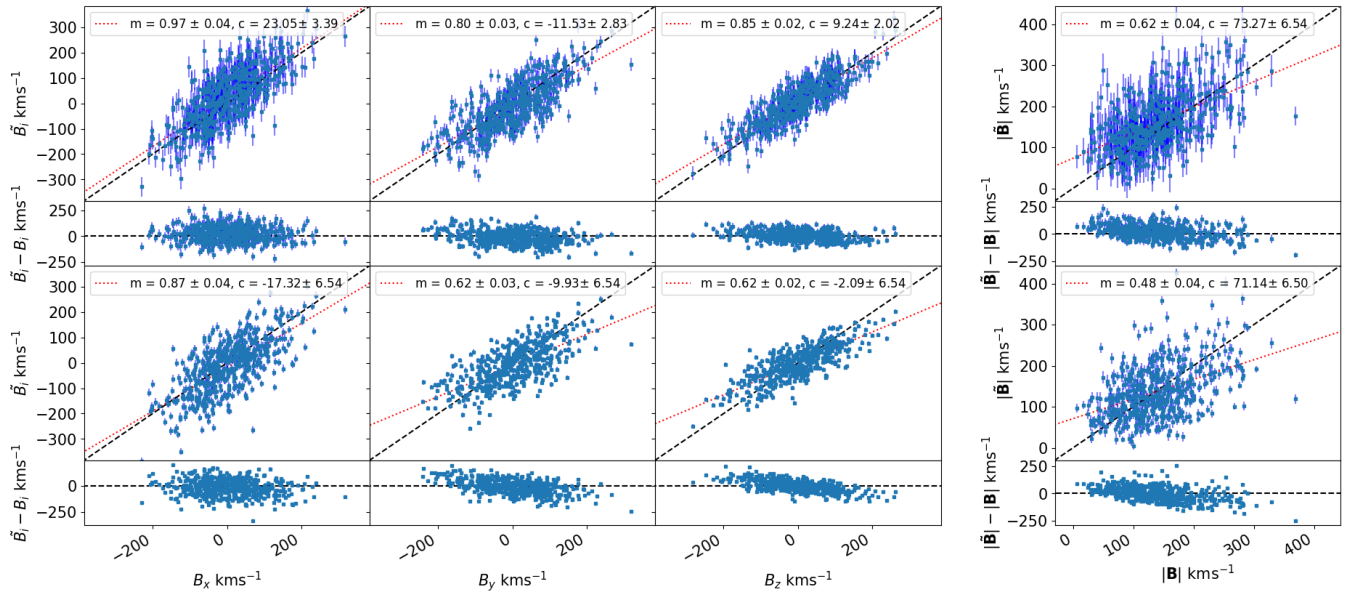


Figure 34: Same as in Figure 32, with where the ideal survey has a radius of $\sim 140 \text{ Mpc } h^{-1}$.

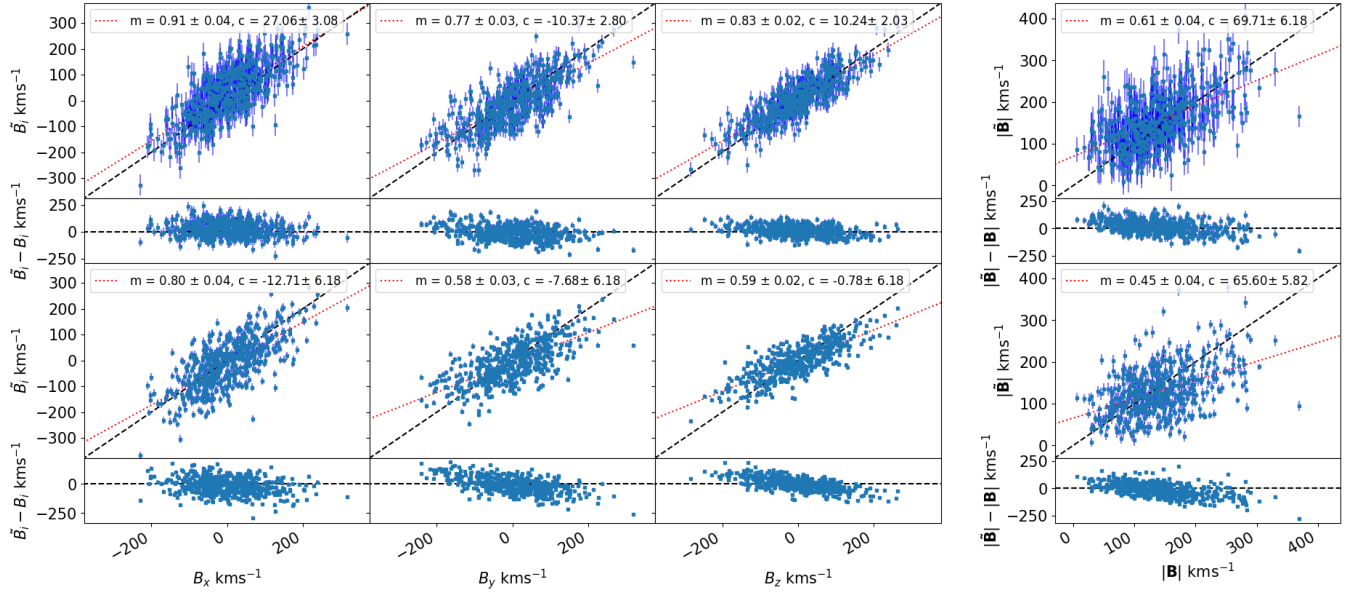


Figure 35: Same as in Figure 32, with where the ideal survey has a radius of $\sim 170 \text{ Mpc } h^{-1}$.

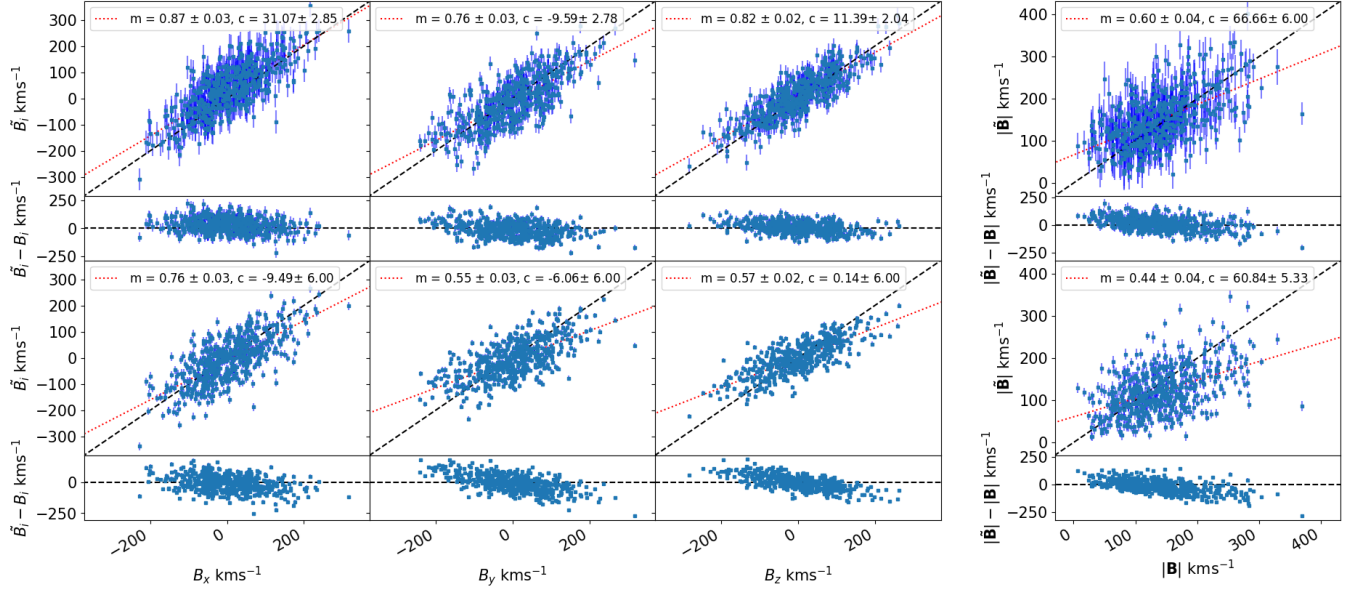


Figure 36: Same as in Figure 32, with where the ideal survey has a radius of $\sim 210 \text{ Mpc } h^{-1}$.

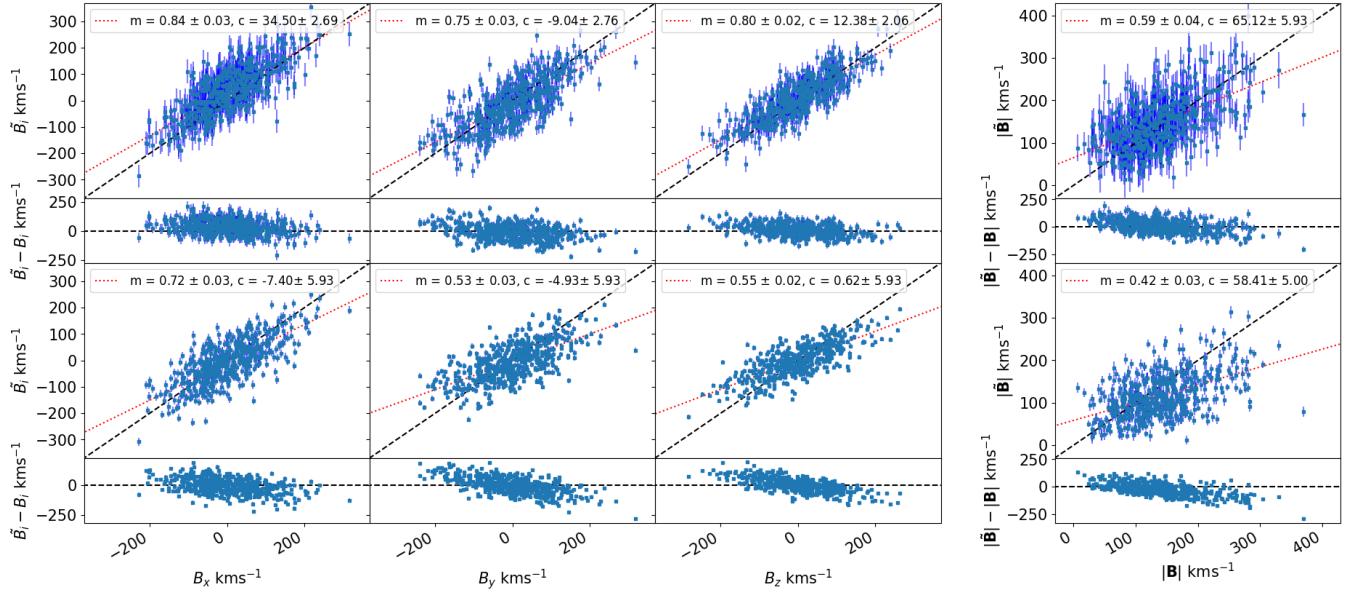


Figure 37: Same as in Figure 32, with where the ideal survey has a radius of $\sim 240 \text{ Mpc } h^{-1}$.

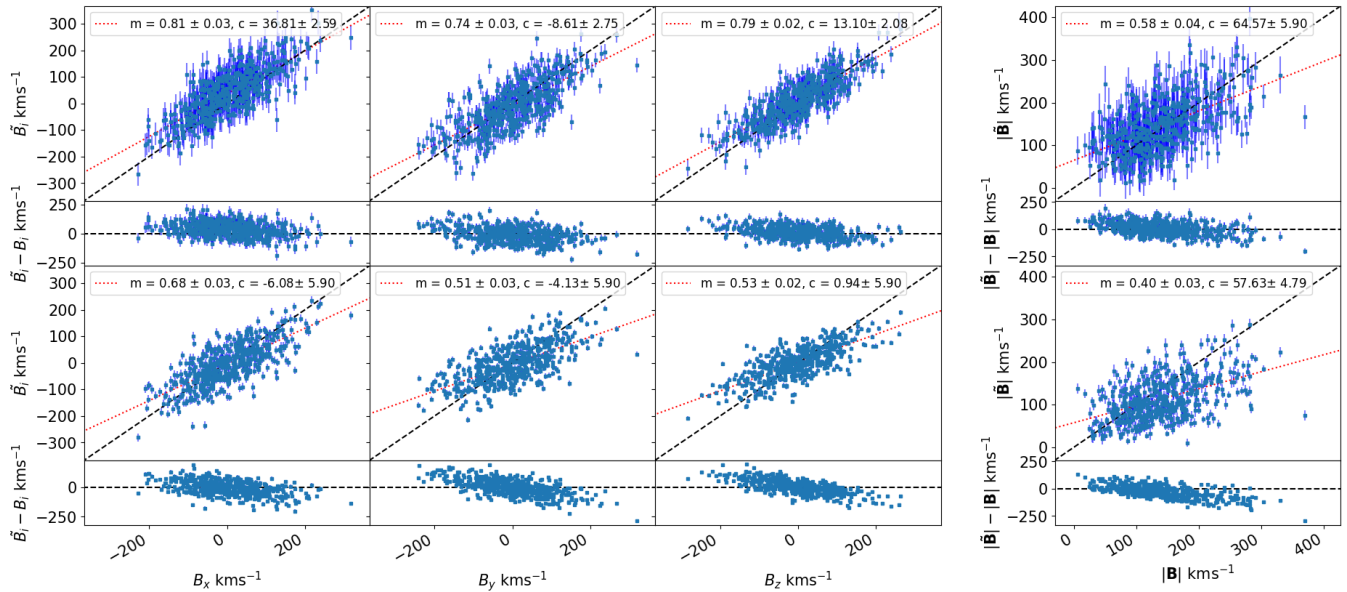


Figure 38: Same as in Figure 32, with where the ideal survey has a radius of $\sim 280 \text{ Mpc } h^{-1}$.

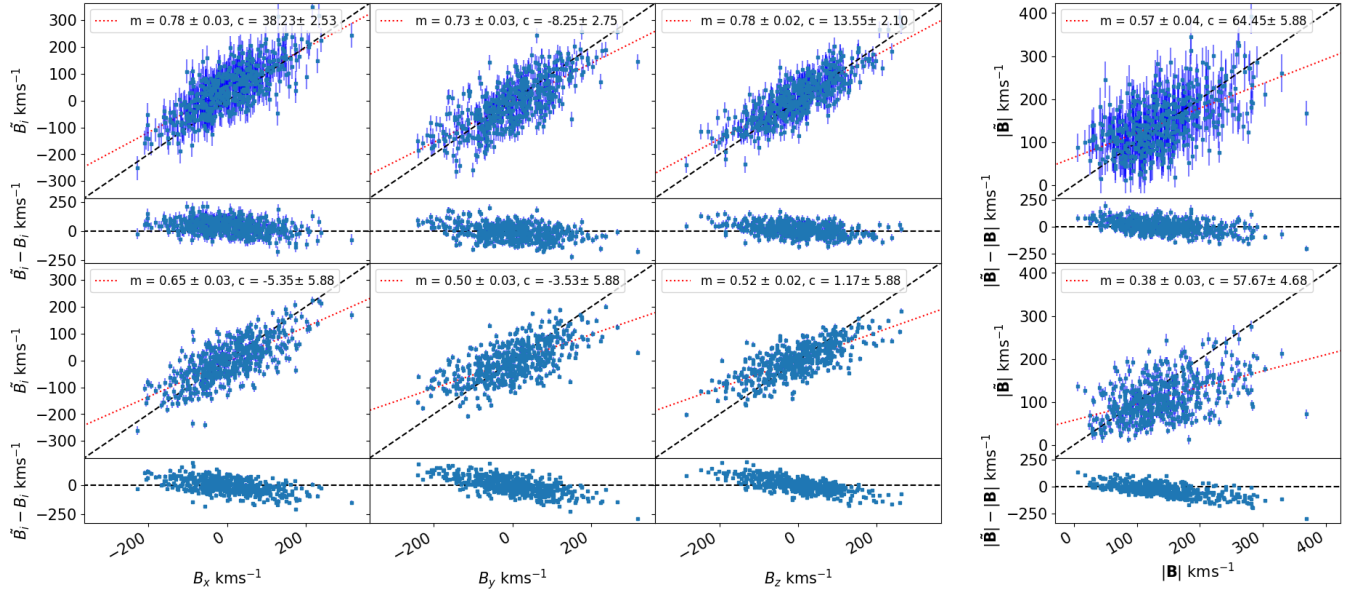


Figure 39: Same as in Figure 32, with where the ideal survey has a radius of ~ 310 Mpc h^{-1} .

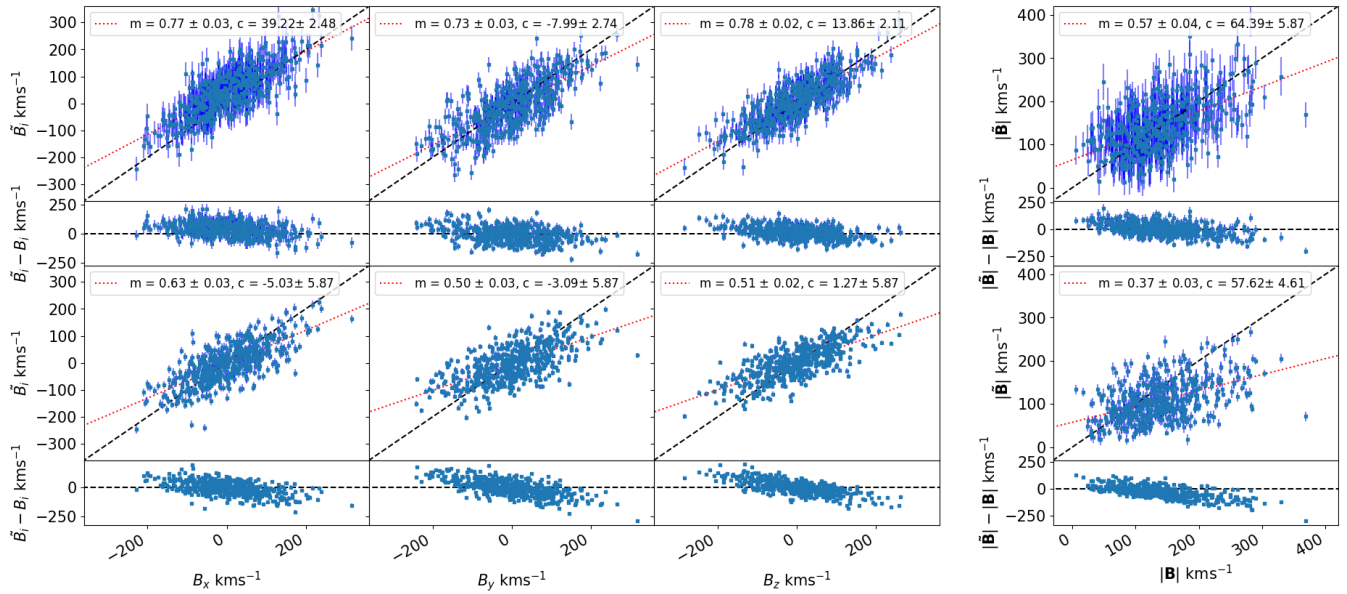


Figure 40: Same as in Figure 32, with where the ideal survey has a radius of ~ 340 Mpc h^{-1} .

Kaiser MLE Results with CF4 mocks: radial cuts to data

Results for the CF4 mocks when applying the Kaiser estimator. The results are shown here in Supergalactic coordinates. The data has been cut at various radii to include only objects at distances below or equal to the specified cut-off scale r_c , to look at the effect of the estimator and bulk flow measurements on different portions of the data, as we expect there may be some difference in the results at smaller radii where the data is more uniformly distributed across the sky compared to larger radii where the SDSS data dominates.

In all cases the $\chi^2 \sim 23$ (regardless of the cut to the data). There is also some bias in the Kaiser estimator result, and it is fairly constant with the amount of data cut.

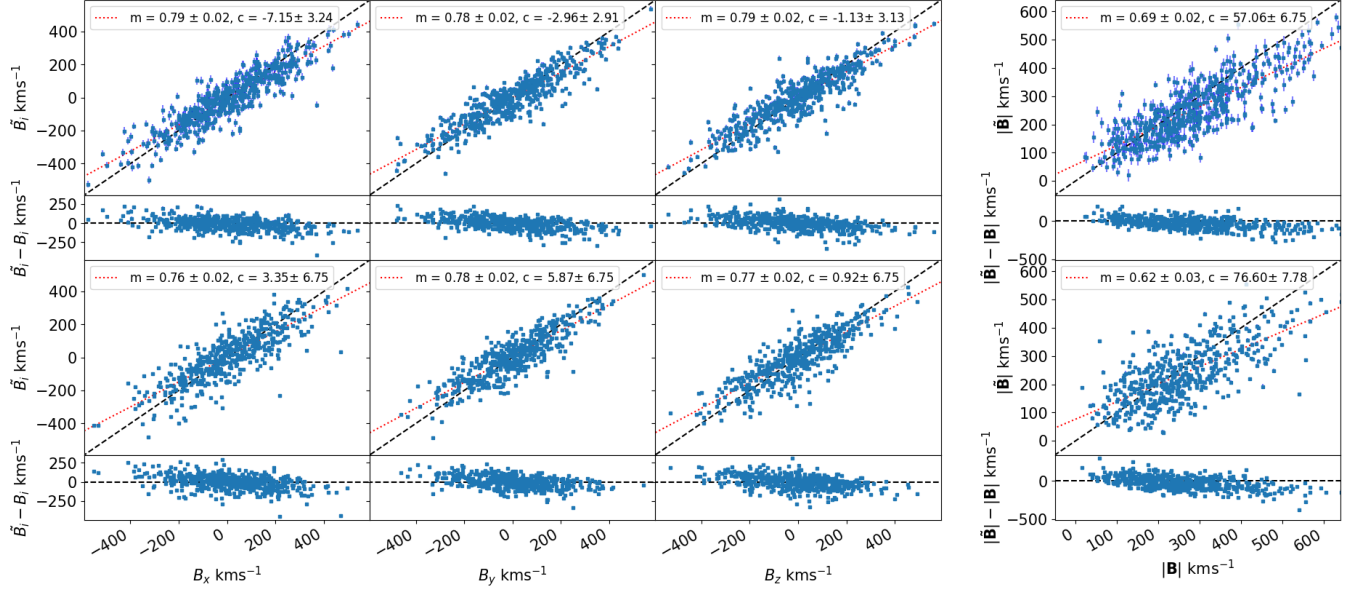


Figure 41: Results from applying the Kaiser estimator with data that lies at distances $\geq 69 \text{ Mpc } h^{-1}$ not included, $r_c = 69 \text{ Mpc } h^{-1}$. The top rows show the results when using the observed log-distance ratios for the estimator, the bottom panel for the true PVs with zero uncertainty. The red dashed line in the panel for the amplitude measured gives the gradient m and y-intercept c for a linear regression to the data.

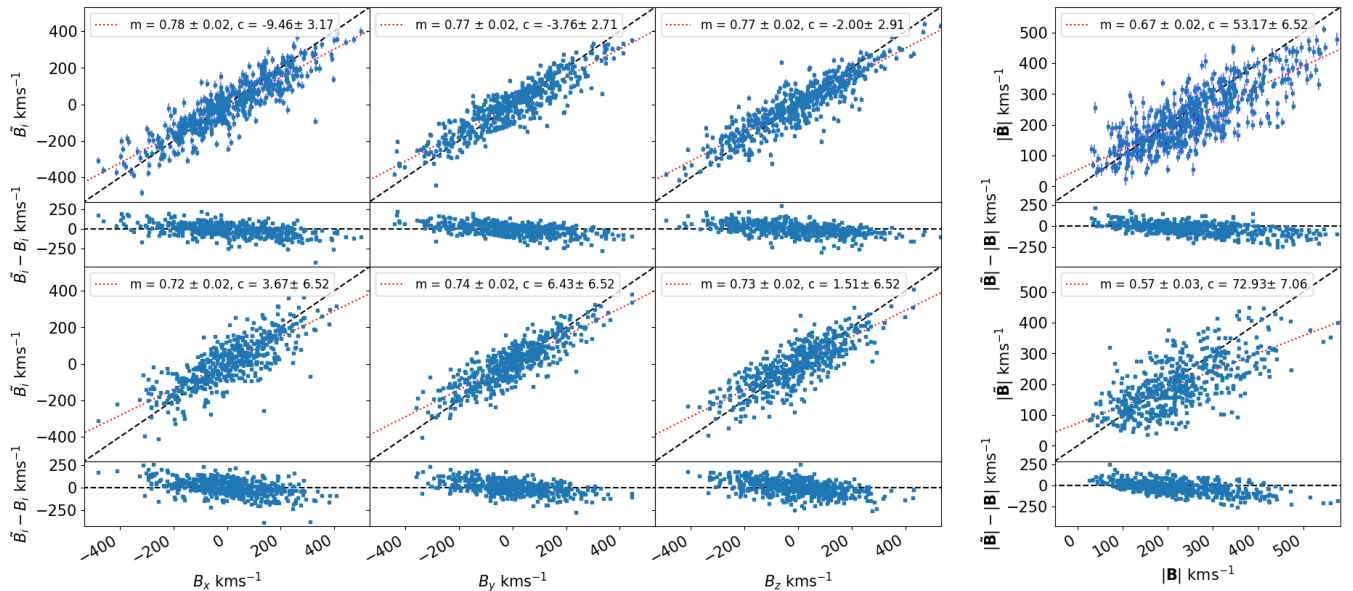


Figure 42: Same as Figure 41, but when $r_c \sim 100 \text{ Mpc } h^{-1}$.

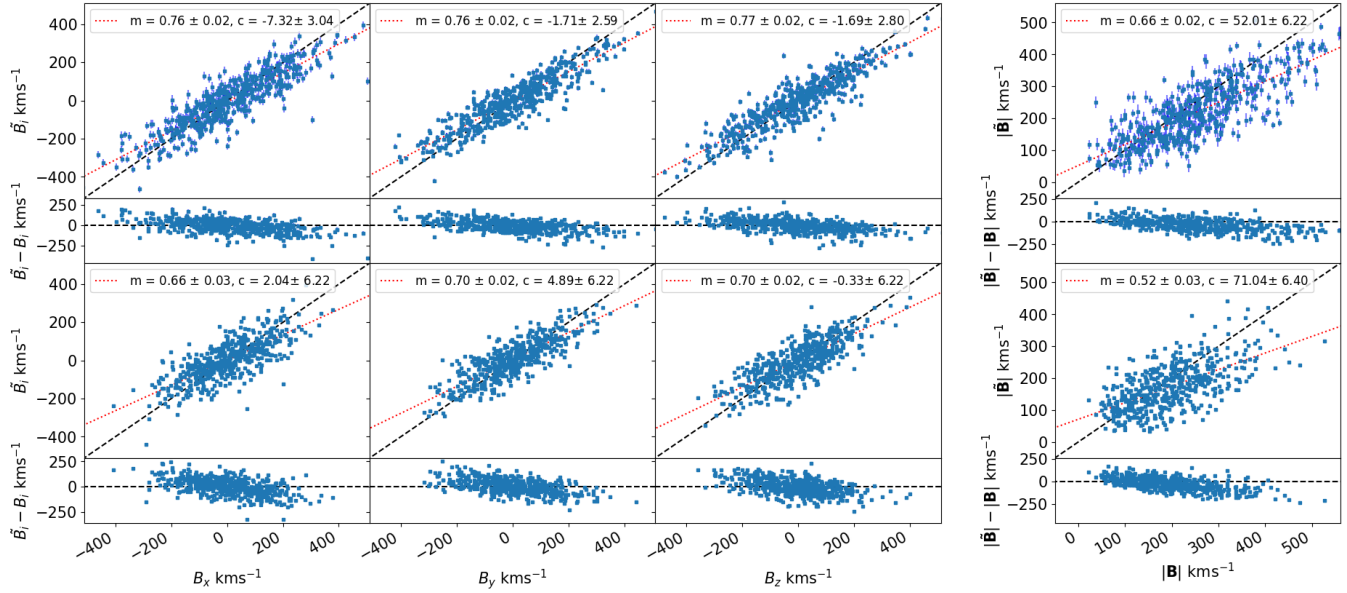


Figure 43: Same as Figure 41, but when $r_c \sim 140 \text{ Mpc } h^{-1}$.

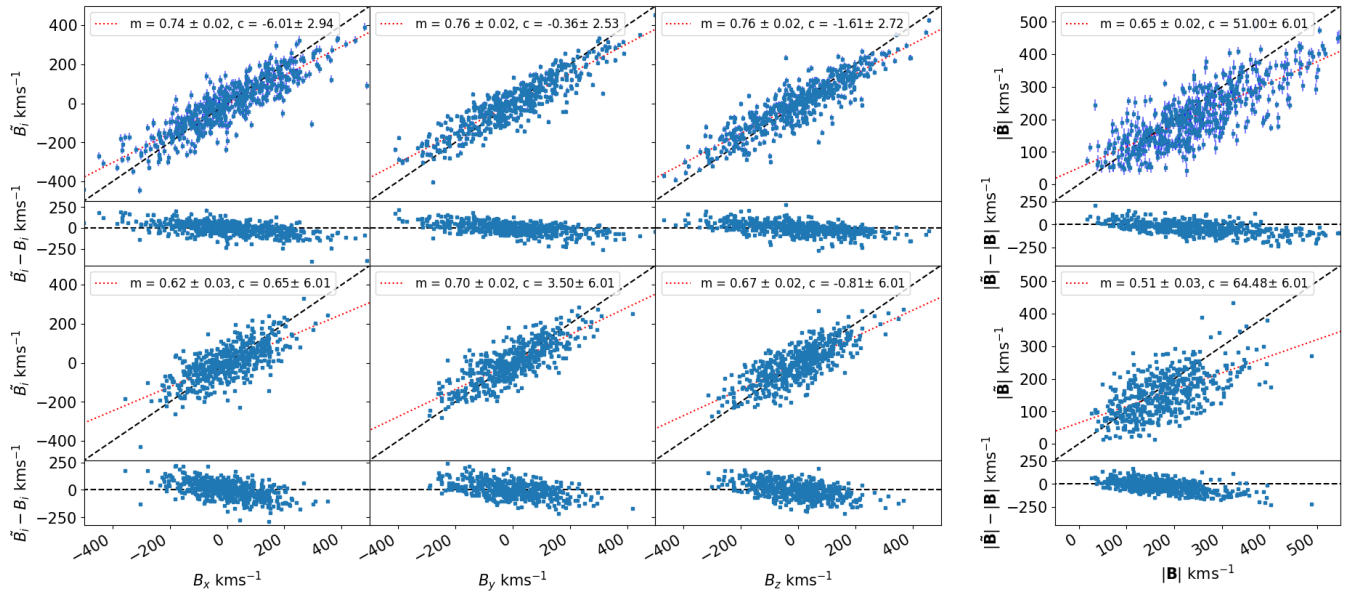


Figure 44: Same as Figure 41, but when $r_c \sim 170 \text{ Mpc } h^{-1}$.

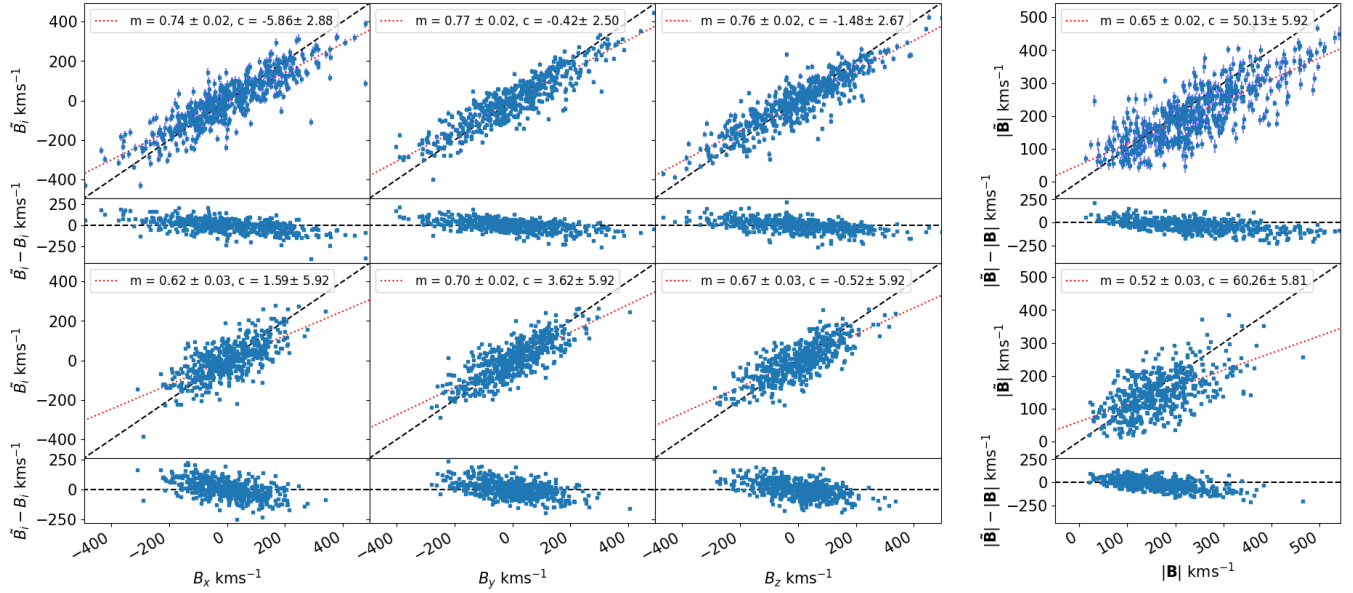


Figure 45: Same as Figure 41, but when $r_c \sim 210 \text{ Mpc } h^{-1}$.

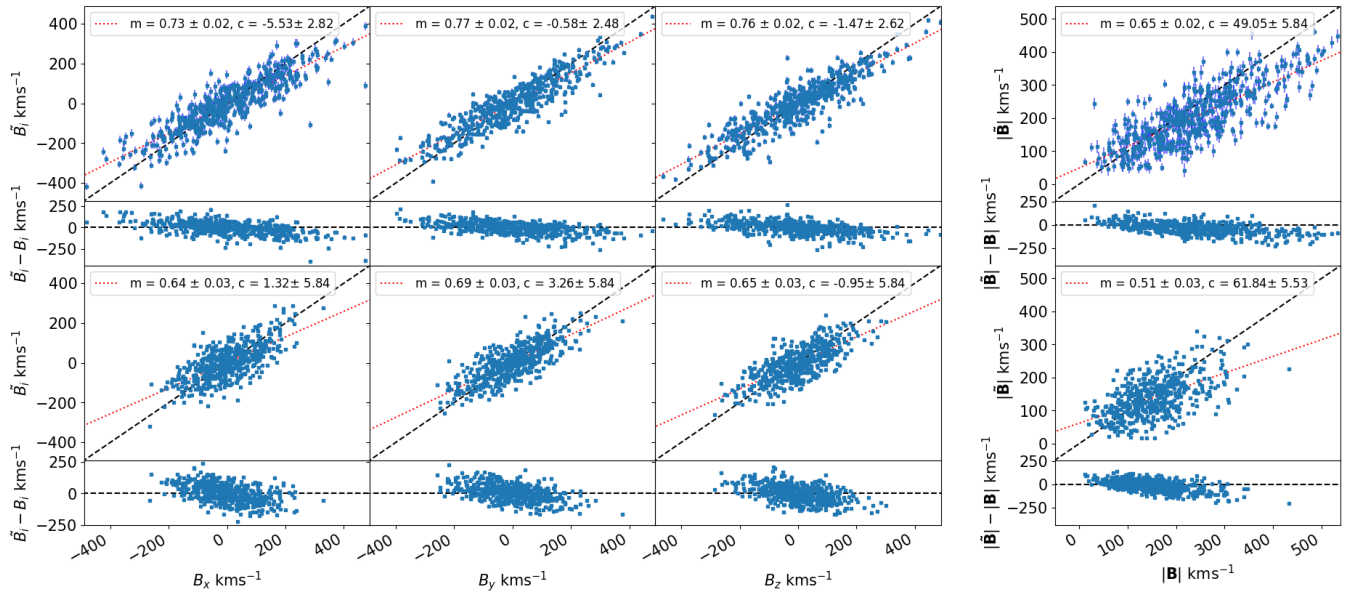


Figure 46: Same as Figure 41, but when $r_c \sim 240 \text{ Mpc } h^{-1}$.

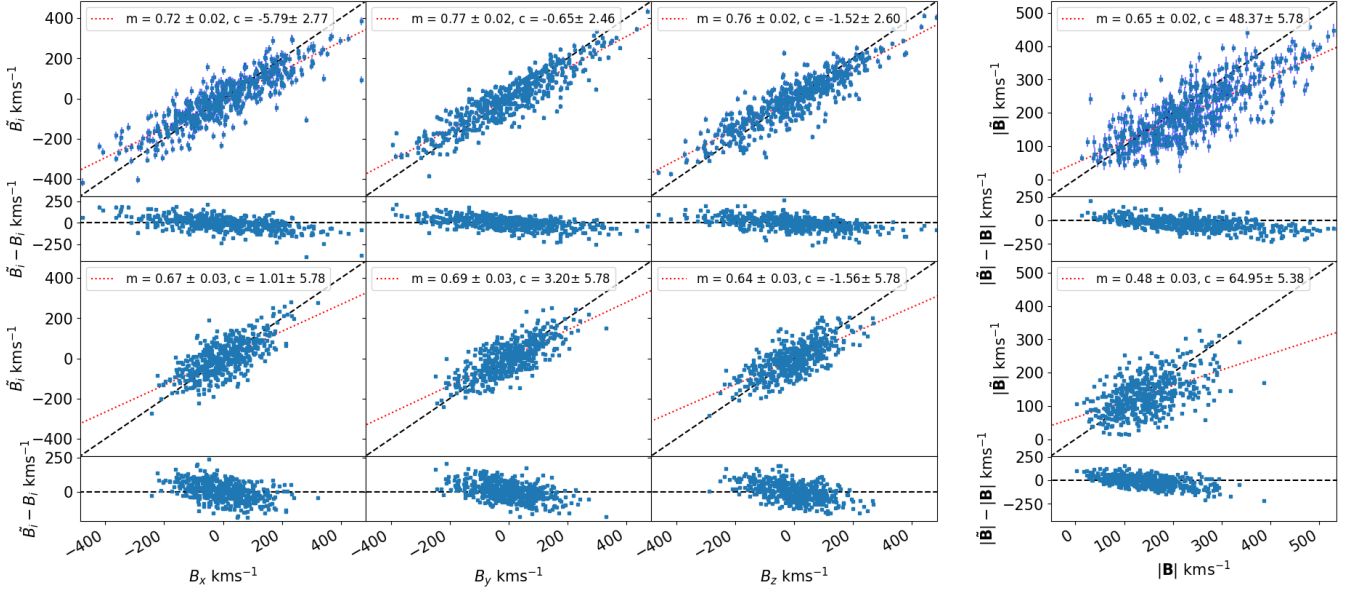


Figure 47: Same as Figure 41, but $r_c \sim 280 \text{ Mpc } h^{-1}$.

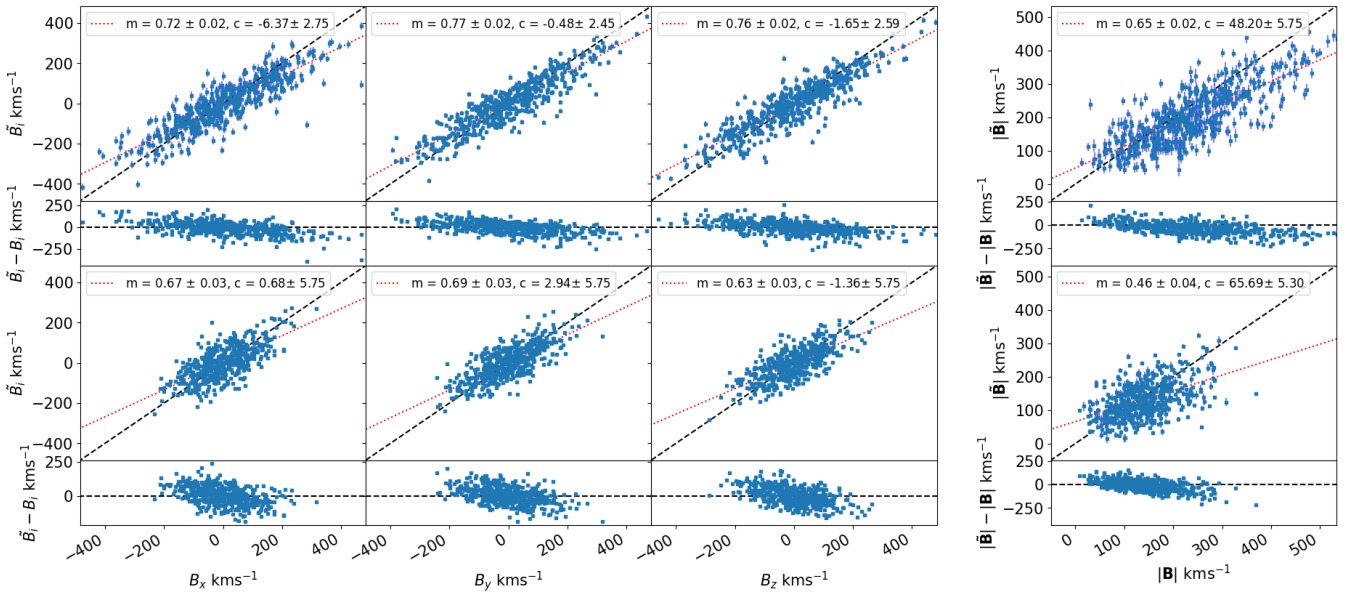


Figure 48: Same as Figure 41, but when $r_c \sim 310 \text{ Mpc } h^{-1}$.

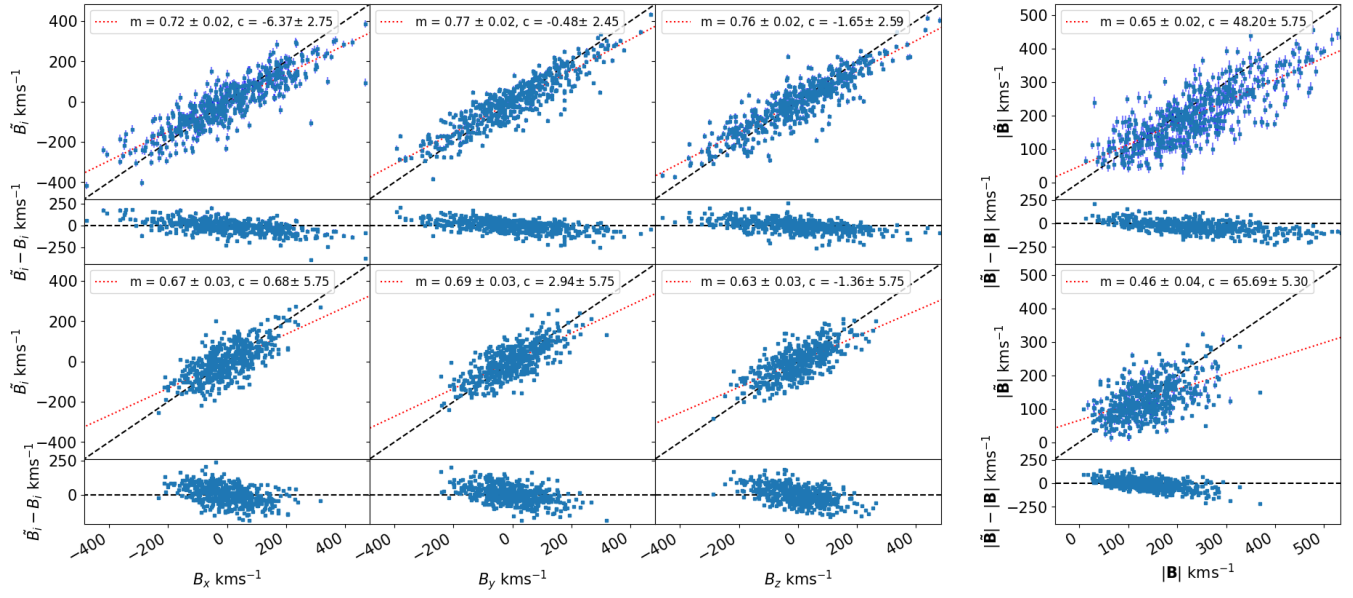


Figure 49: Same as Figure 41, but when $r_c \sim 340 \text{ Mpc } h^{-1}$.

Results in SG coordinates + testing ZP offsets

Kaiser MLE

Here the results when applying the Kaiser MLE to the CF4 mocks are shown again for the full data in each mock. The results have been computed in the Supergalactic coordinate frame here also for better comparison to the results from the real data, which is also presented in Supergalactic coordinates in our paper. Results when applying varying errors to the zero-point of the data set are shown also.

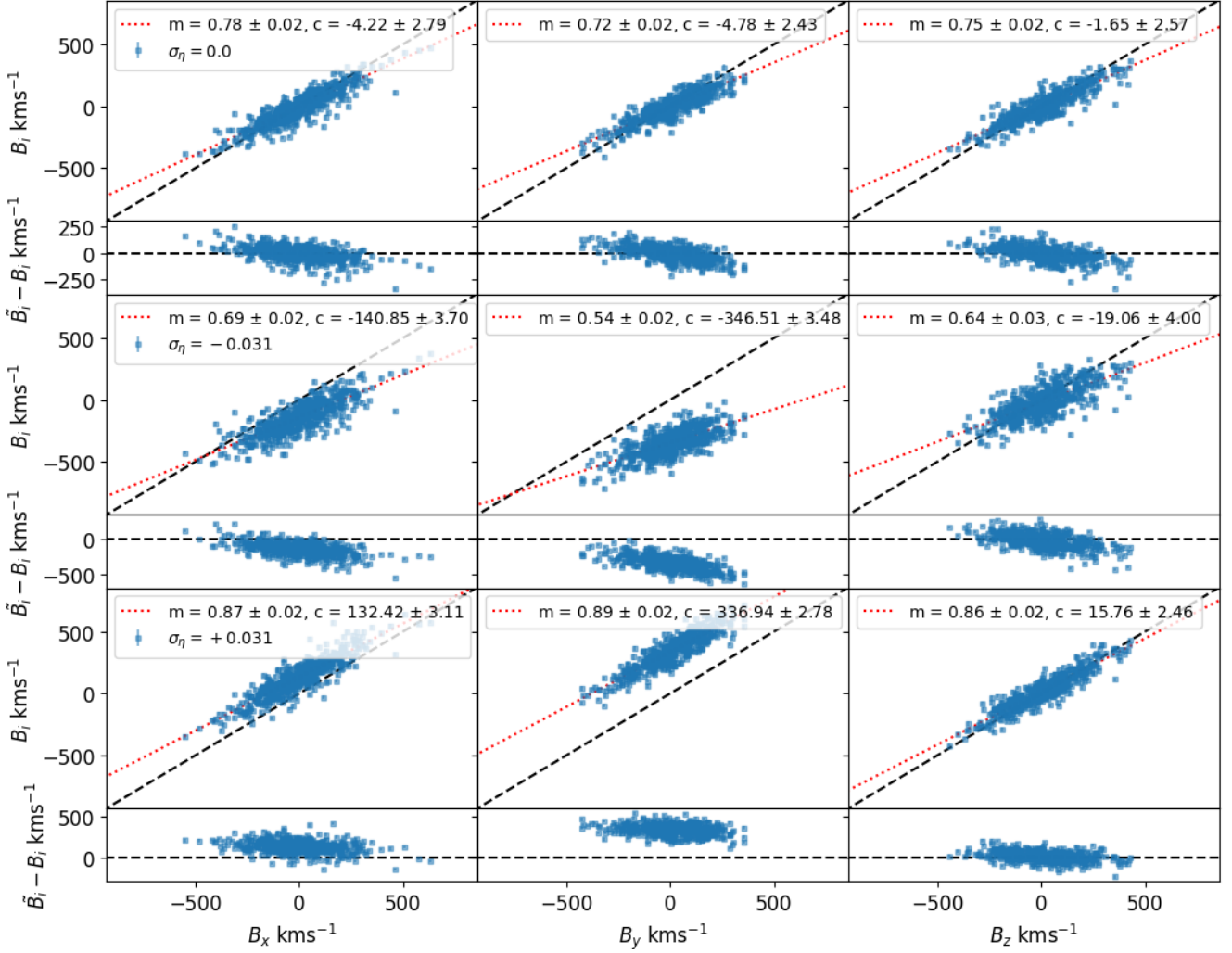


Figure 50: Top panels: recovered bulk flows from the Kaiser MLE in Supergalactic coordinates. Second row of panels: the same, except when a global zero-point offset of -0.031 (corresponding to a H_0 error of $\sim 5 \text{ kms}^{-1} \text{Mpc}^{-1}$) has been introduced in the mock data. Third row of panels: the same as the second row except the global zero-point offset is $+0.031$.

Conclusions:

- adding a global offset has a large effect on the results of the Kaiser method, resulting in large shifts in the bulk flow amplitude that is estimated; the best fitting linear regression has significant variation in the slope and y-intercept compared to the case where there is no zero-point offsets
- adding a relative offset to the CF4TF or 6dFGSv dataset doesn't affect the slope of the best fit linear regression strongly for the Kaiser method, but it does affect the intercept slightly (although much less strongly)
- overall an error in the global zero-point (essentially a H_0 error) has a strong effect on the Kaiser MLE results, and only a small effect is introduced by relative systematic offsets between datasets that make up CF4

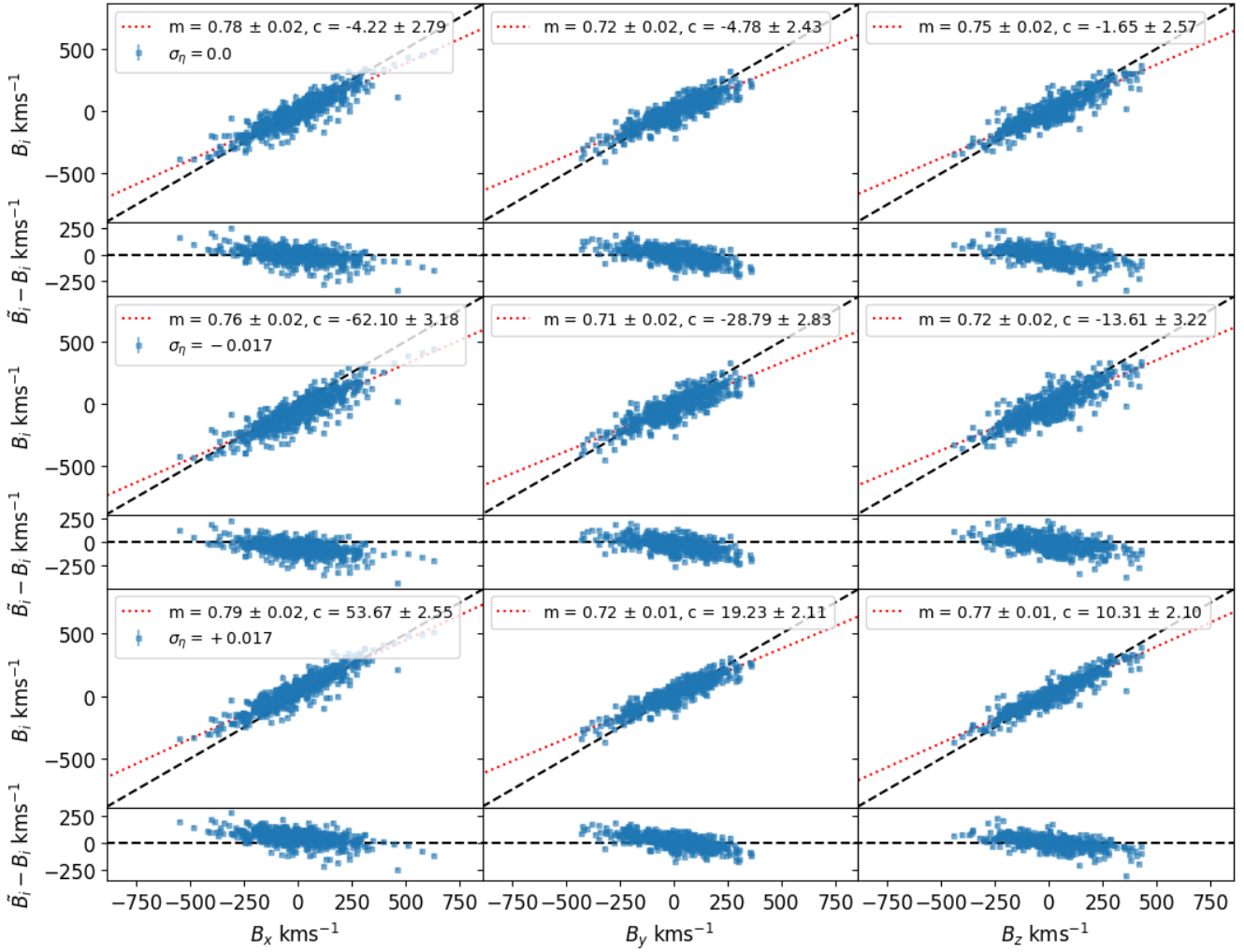


Figure 51: Top panels: recovered bulk flows from the Kaiser MLE in Supergalactic coordinates. Second row of panels: the same, except when a relative zero-point offset of -0.017 has been introduced in the CF4TF data for the mock. Third row of panels: the same as the second row except the relative zero-point offset is $+0.017$.

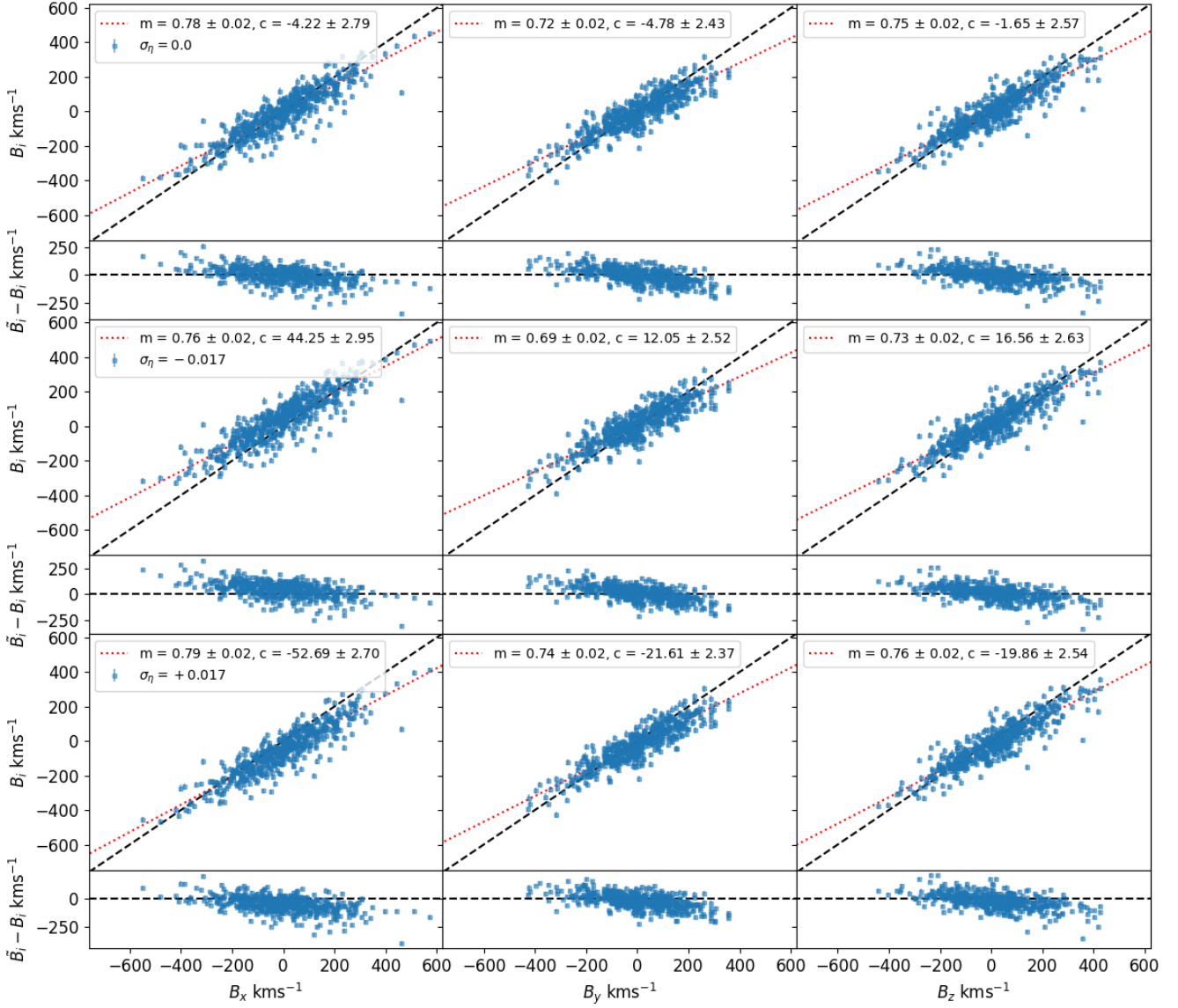


Figure 52: Top panels: recovered bulk flows from the Kaiser MLE in Supergalactic coordinates. Second row of panels: the same, except when a relative zero-point offset of -0.017 has been introduced in the 6dFGSv data for the mock. Third row of panels: the same as the second row except the relative zero-point offset is $+0.017$.

Peery MVE

Here the results when applying the Peery MVE to the CF4 mocks are shown again for the full data in each mock. The results have been computed in the Supergalactic coordinate frame for comparison to the results from the real data, which is also presented in Supergalactic coordinates. Results when applying varying errors to the zero-point of the data set are shown also.

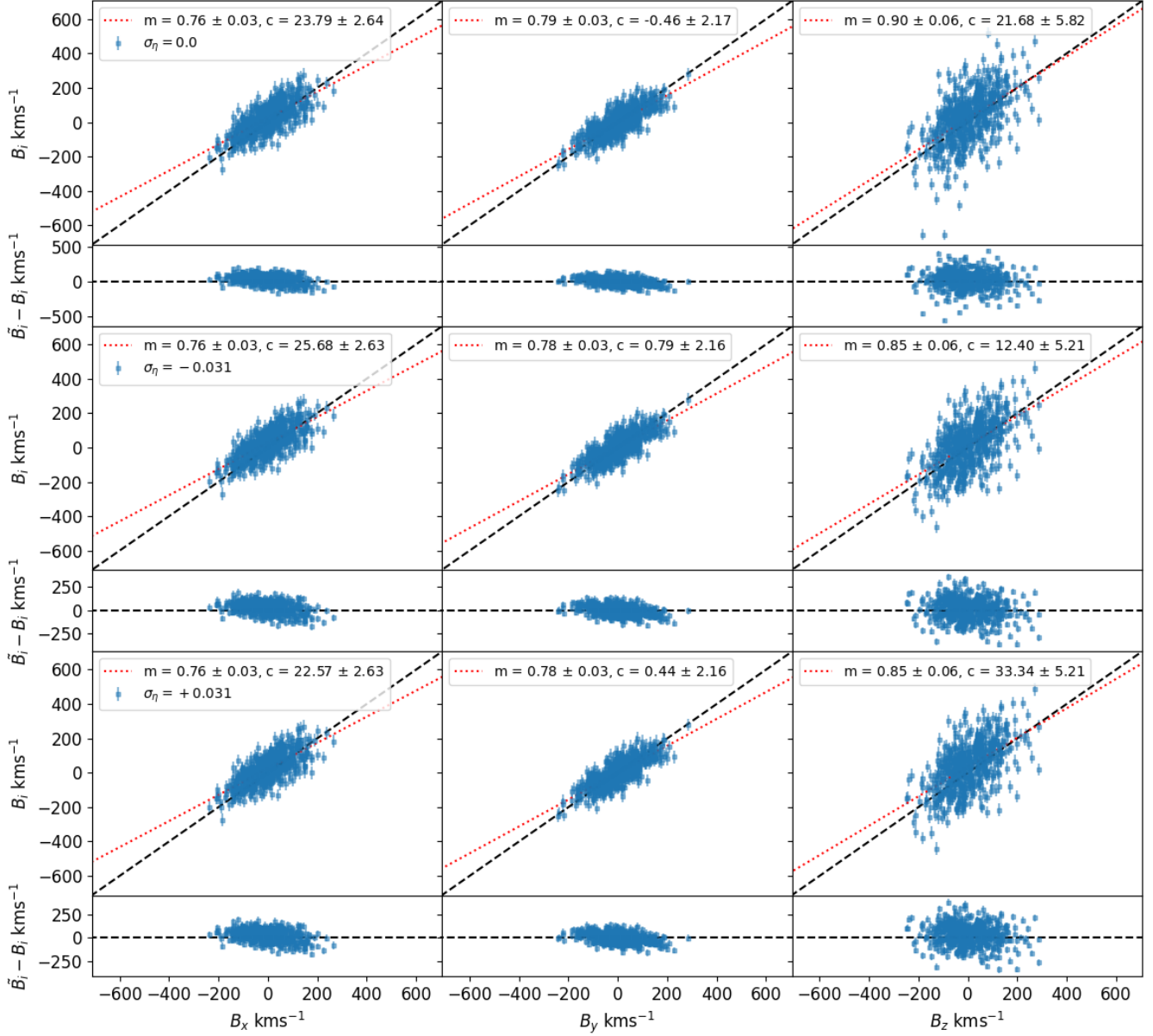


Figure 53: Top panels: recovered bulk flows from the Peery MVE in Supergalactic coordinates. Second row of panels: the same, except when a global zero-point offset of -0.031 (corresponding to a H_0 error of $\sim 5 \text{km s}^{-1} \text{Mpc}^{-1}$) has been introduced in the mock data. Third row of panels: the same as the second row except the global zero-point offset is $+0.031$.

Conclusions:

- adding a global offset has almost effect on the results of the Peery method; the best fitting linear regression has little significant variation in the slope and y-intercept compared to the case where there is no zero-point offsets

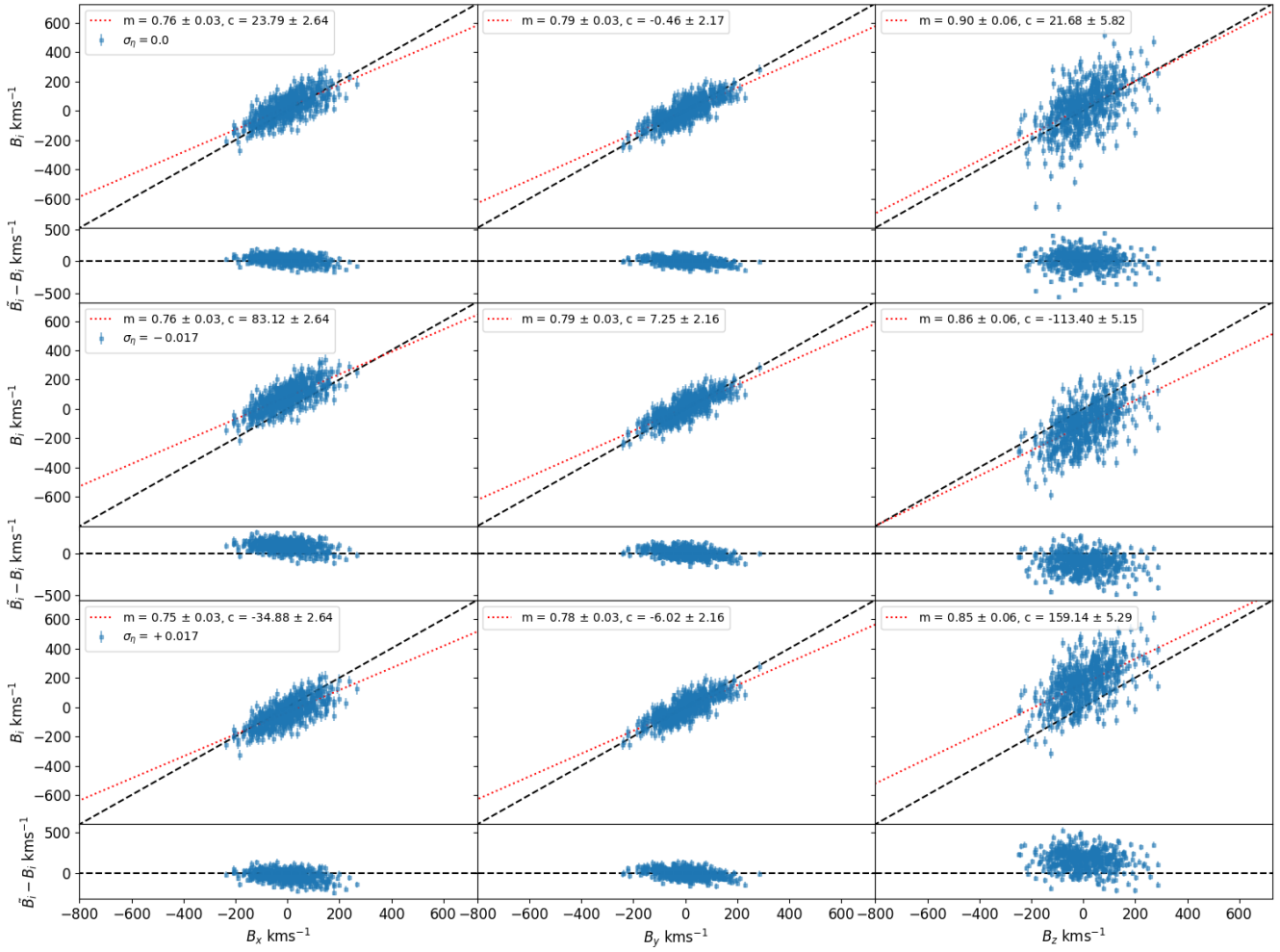


Figure 54: Top panels: recovered bulk flows from the Peery MVE in Supergalactic coordinates. Second row of panels: the same, except when a relative zero-point offset of -0.017 has been introduced in the CF4TF data for the mock. Third row of panels: the same as the second row except the relative zero-point offset is $+0.017$.

- adding a relative offset to the CF4TF or 6dFGSv dataset doesn't affect the slope of the best fit linear regression strongly for the Peery method, but it does affect the intercept significantly for the x and z modes of the bulk flow

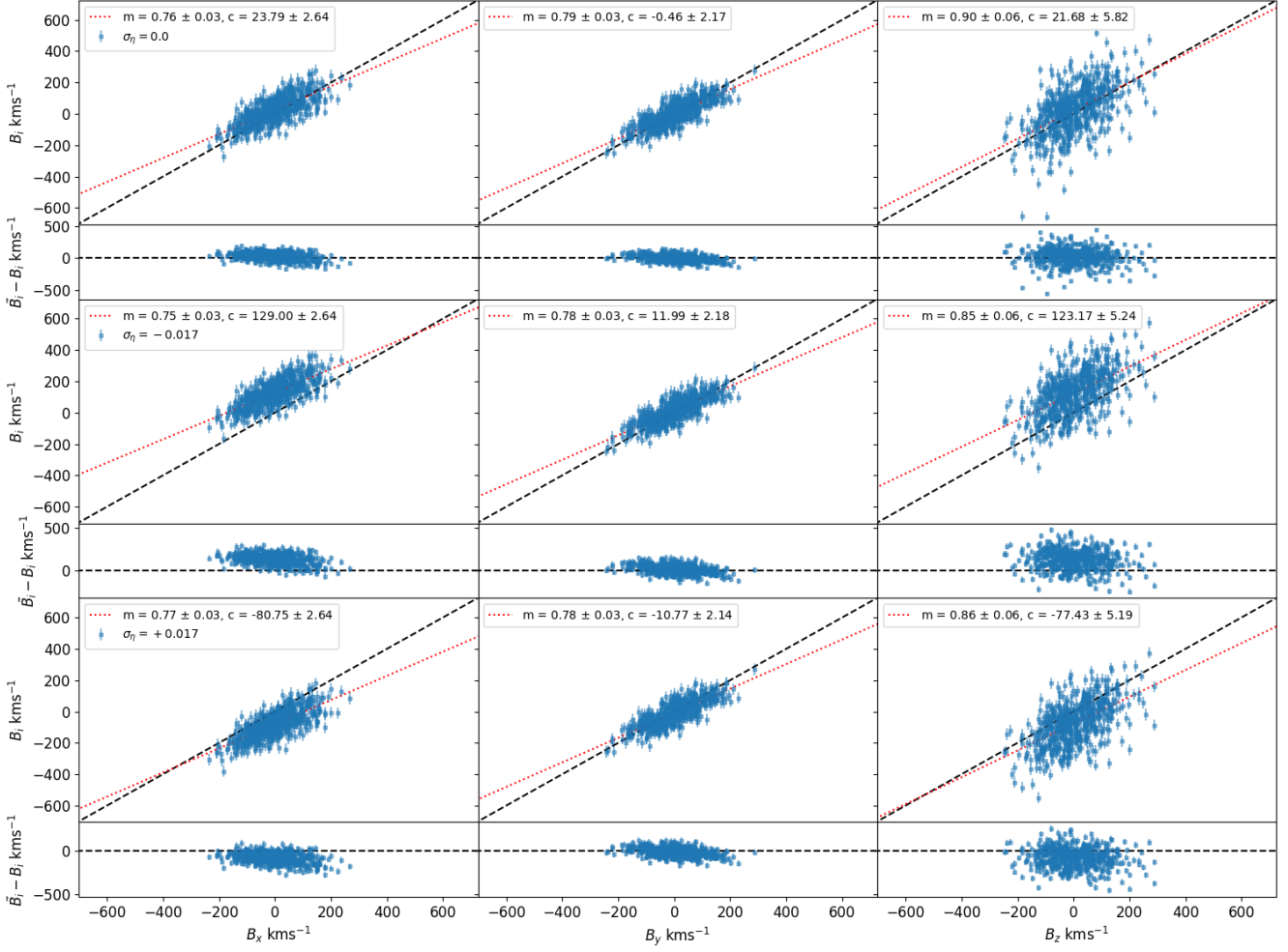


Figure 55: Top panels: recovered bulk flows from the Peery MVE in Supergalactic coordinates. Second row of panels: the same, except when a relative zero-point offset of -0.017 has been introduced in the 6dFGSv data for the mock. Third row of panels: the same as the second row except the relative zero-point offset is $+0.017$.

Results for subsamples of the mocks in SG coordinates

In this section results are shown for the subsets of the stacked CF4 mocks (made by stacking the SDSSv, 6dFGSv and CF4TF mocks together). This is done with different radial cuts to the data (when applying the Kaiser MVE) and when using different radii for the ideal survey (when applying the MVE).

Kaiser MLE, CF4 mocks with $z \geq 0.02$ only

Results are shown here for the CF4 mocks when applying the Kaiser MLE, but when the mocks have been used while excluding the mock data below $z \leq 0.02$; this is done so it can be compared to the same analysis done on the real CF4 data. The $\chi^2 \sim 3.3, 7, 7.7, 7.8, 7.8, 7.8, 7.8, 7.8, 7.8$ for each radial cut to the data.

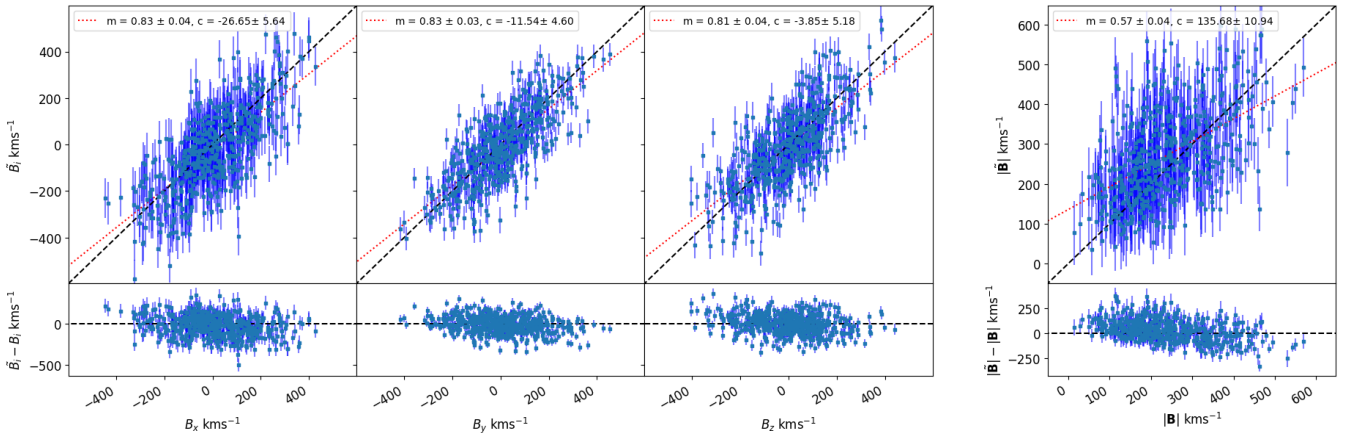


Figure 56: Results applying the Kaiser MLE approach to the CF4 mocks with $z \geq 0.02$ only included in the mock data, for 512 mocks. Only data at a radial distance that satisfied $\leq 69 \text{ Mpc } h^{-1}$ is included, i.e. $r_c = 69 \text{ Mpc } h^{-1}$.

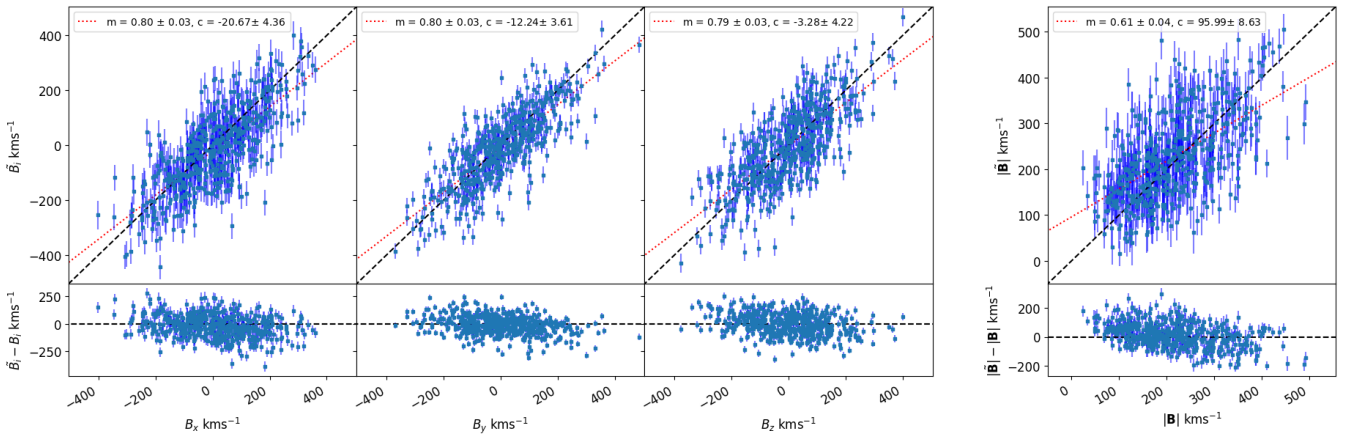


Figure 57: Same as Figure 56, but when $r_c \sim 100 \text{ Mpc } h^{-1}$.

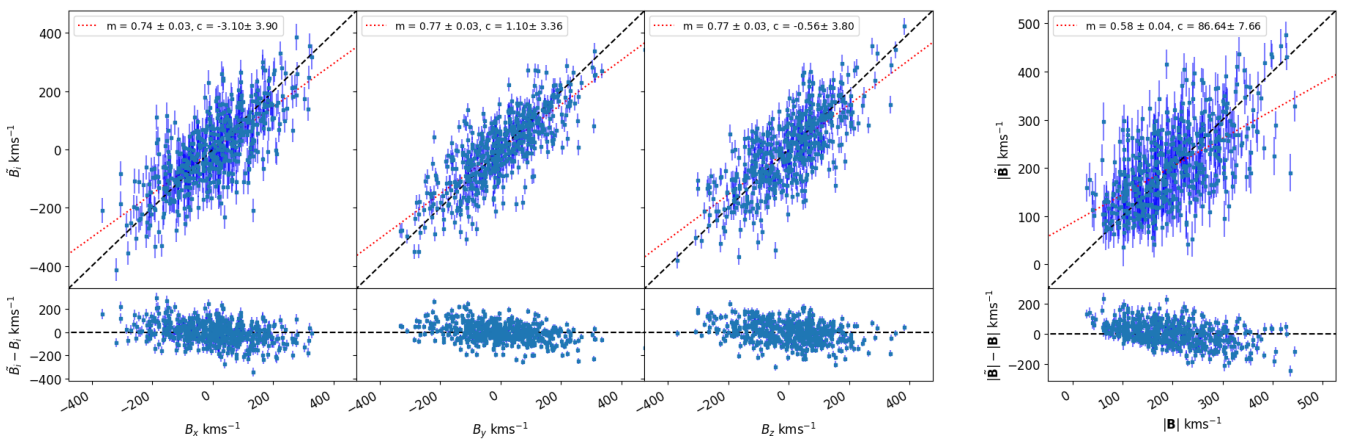


Figure 58: Same as Figure 56, but when $r_c \sim 140 \text{ Mpc } h^{-1}$.

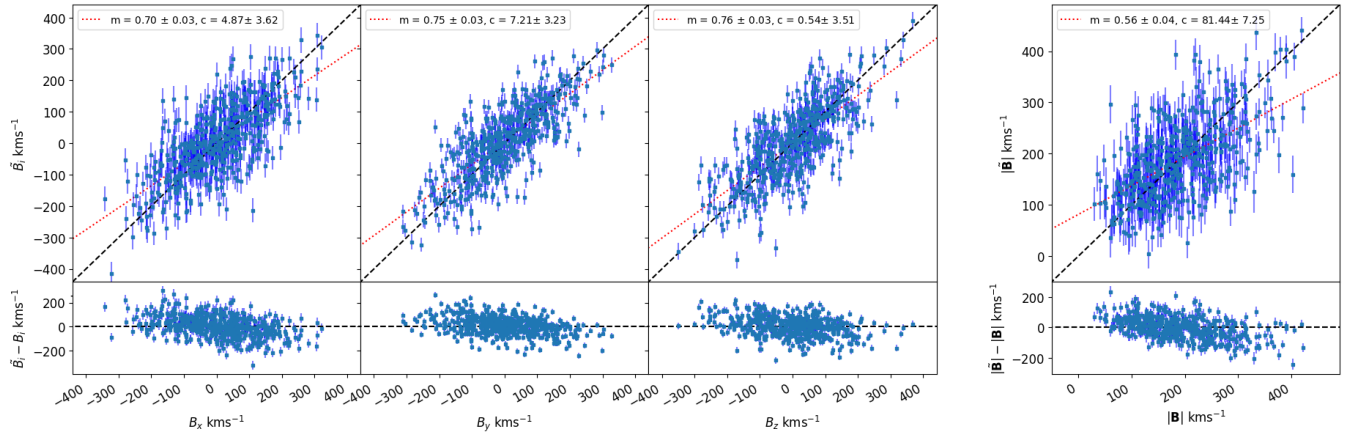


Figure 59: Same as Figure 56, but when $r_c \sim 170 \text{ Mpc} h^{-1}$.

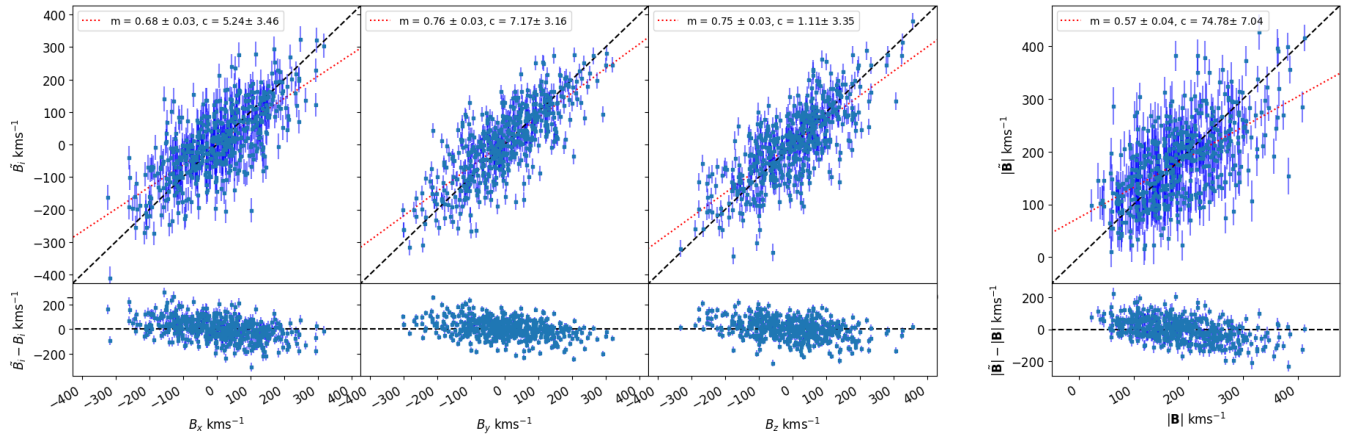


Figure 60: Same as Figure 56, but when $r_c \sim 210 \text{ Mpc} h^{-1}$.

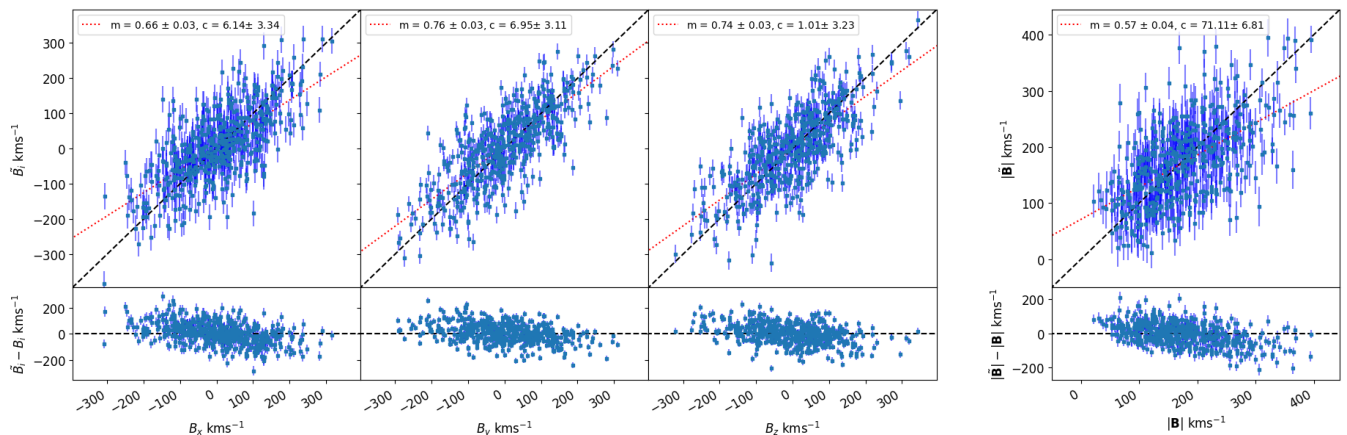


Figure 61: Same as Figure 56, but when $r_c \sim 240 \text{ Mpc} h^{-1}$.

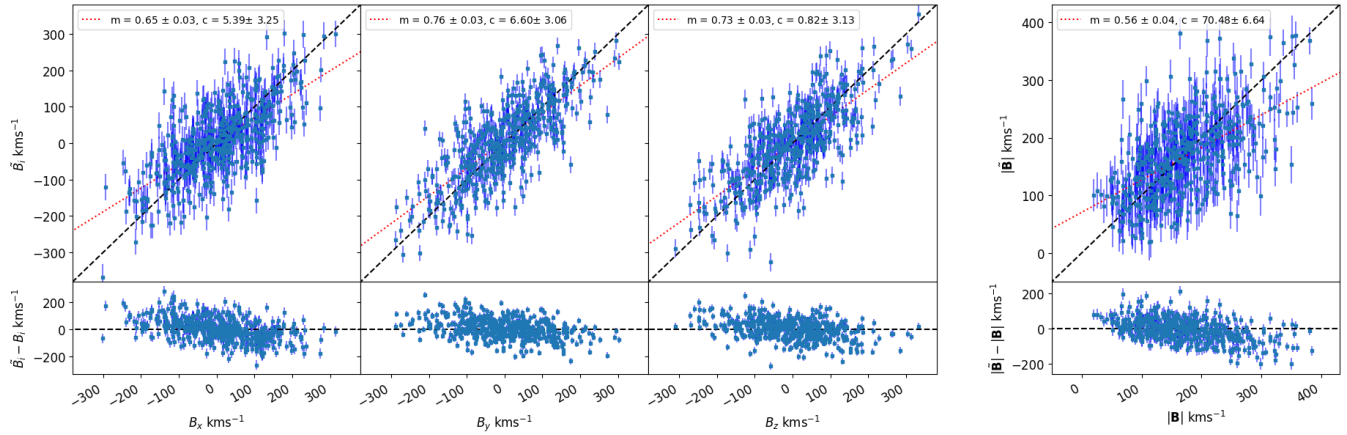


Figure 62: Same as Figure 56, but when $r_c \sim 275 \text{ Mpc} h^{-1}$.

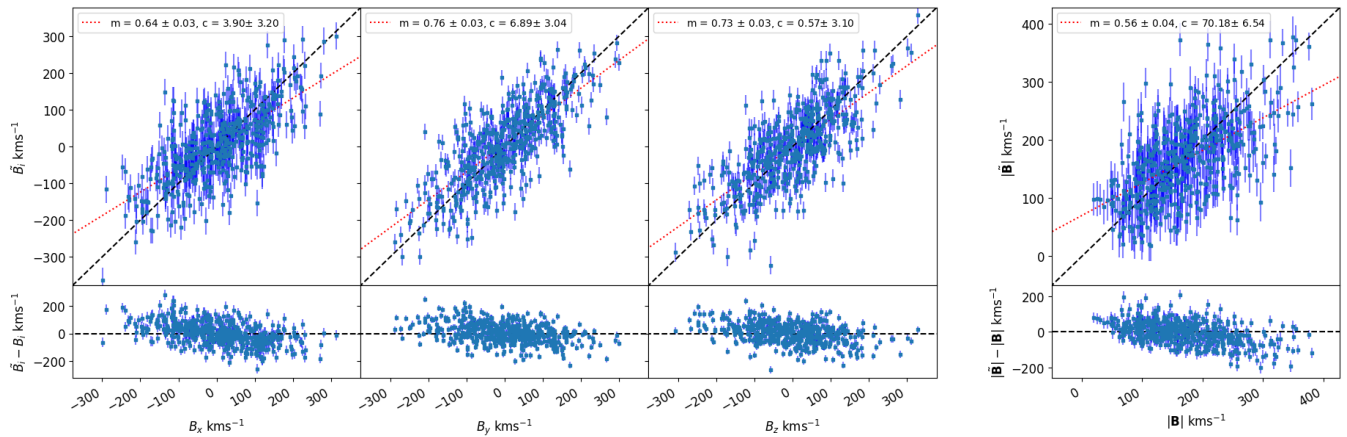


Figure 63: Same as Figure 56, but when $r_c \sim 310 \text{ Mpc} h^{-1}$.

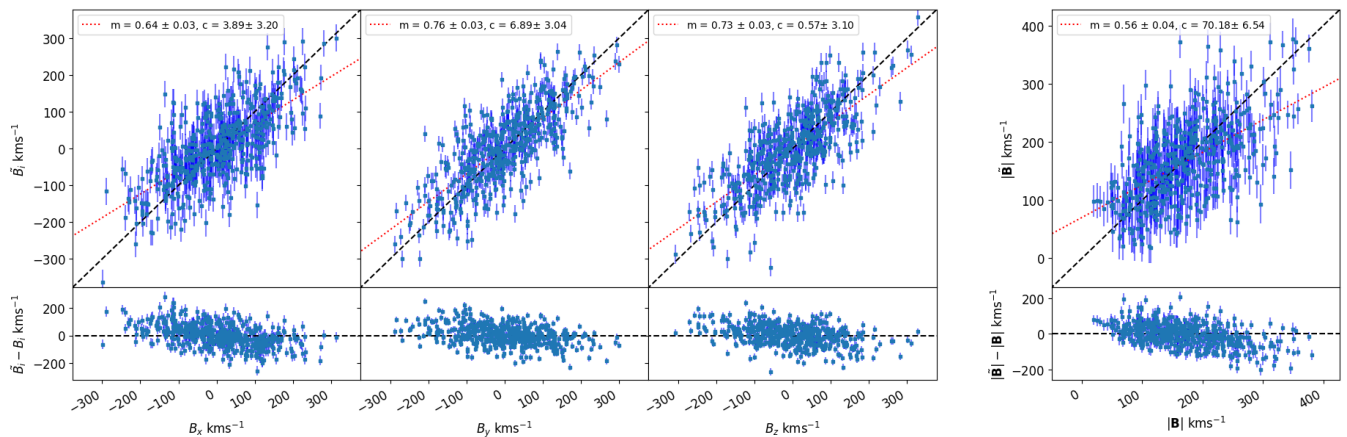


Figure 64: Same as Figure 56, but when $r_c \sim 345 \text{ Mpc} h^{-1}$.

Kaiser MLE, SDSS mock data only

Results are shown here for the SDSS mocks only when applying the Kaiser MLE, for comparison to the same analysis done on the SDSS part of the data included in the CF4 dataset only. The $\chi^2 \sim 2.2, 3.4, 3.9, 4.1, 4.2, 4.4, 4.4, 4.4, 4.4$ for each radial cut to the data.

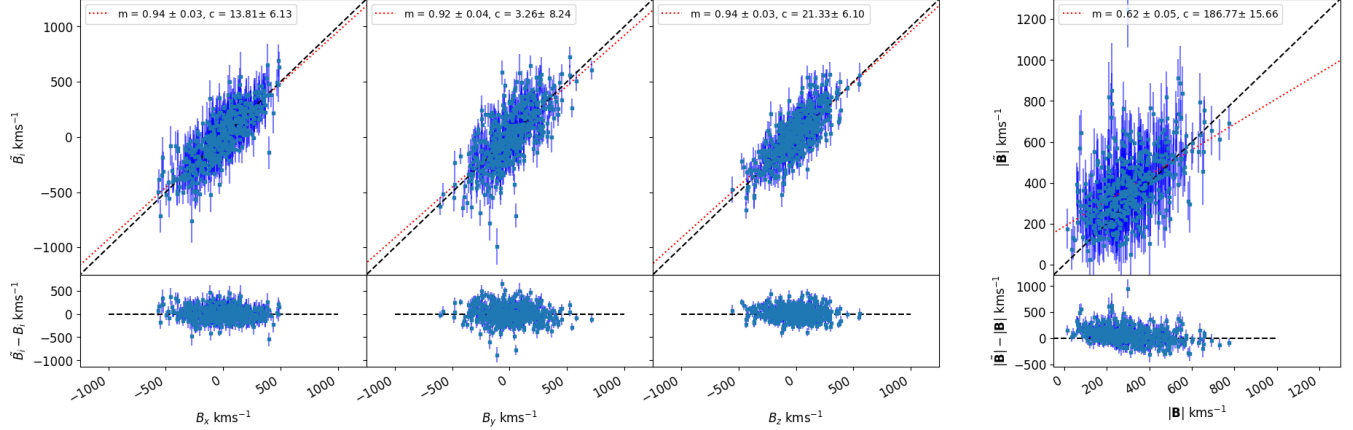


Figure 65: Results applying the Kaiser MLE approach to the SDSS part of the CF4 mocks in the mock data, for 512 mocks. Only data at a radial distance that satisfied $\leq 69 \text{ Mpc } h^{-1}$ is included, i.e. $r_c = 69 \text{ Mpc } h^{-1}$.

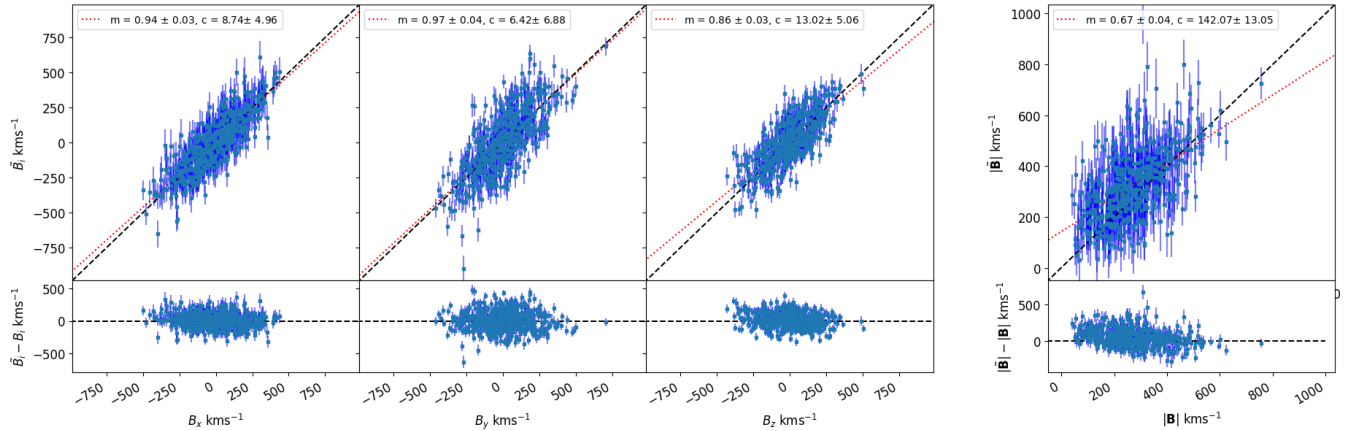


Figure 66: Same as Figure 65, but when $r_c \sim 100 \text{ Mpc } h^{-1}$.

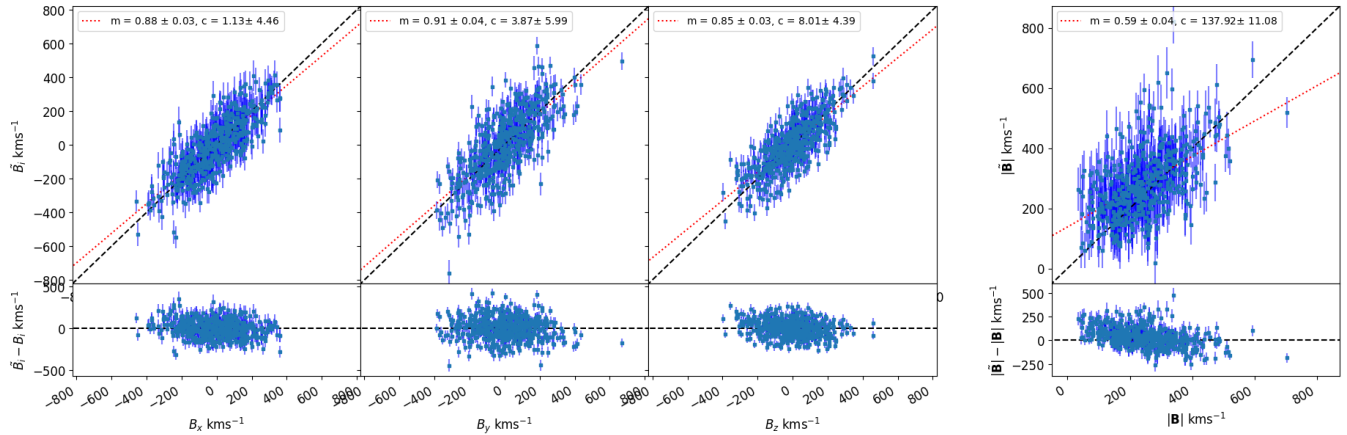


Figure 67: Same as Figure 65, but when $r_c \sim 140 \text{ Mpc} h^{-1}$.

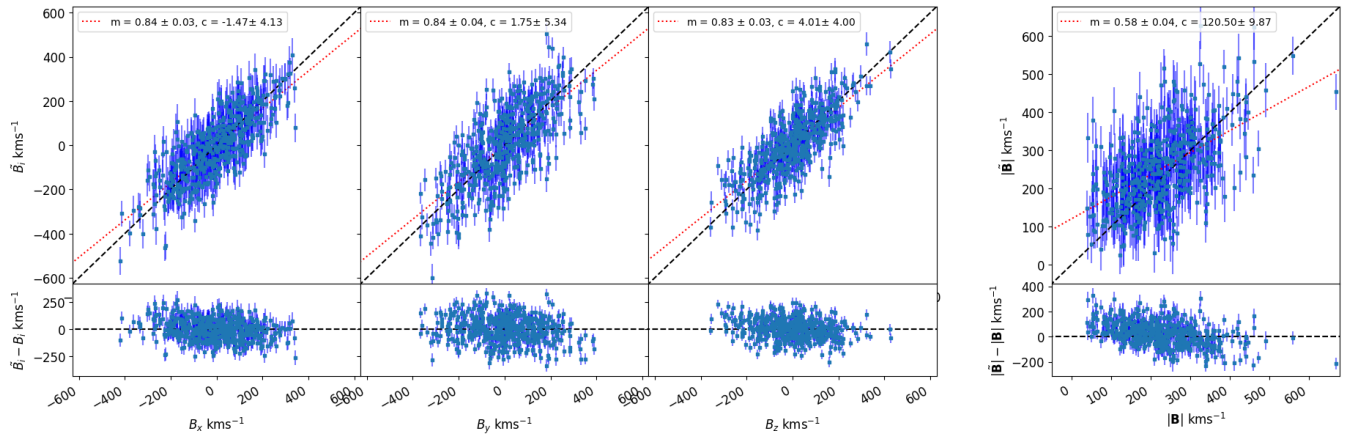


Figure 68: Same as Figure 65, but when $r_c \sim 170 \text{ Mpc} h^{-1}$.

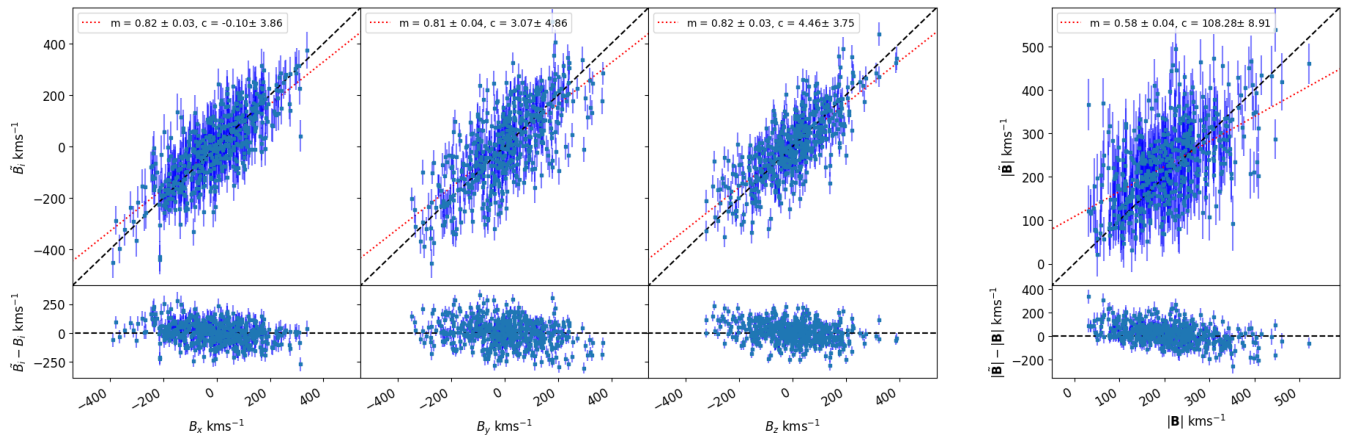


Figure 69: Same as Figure 65, but when $r_c \sim 210 \text{ Mpc} h^{-1}$.

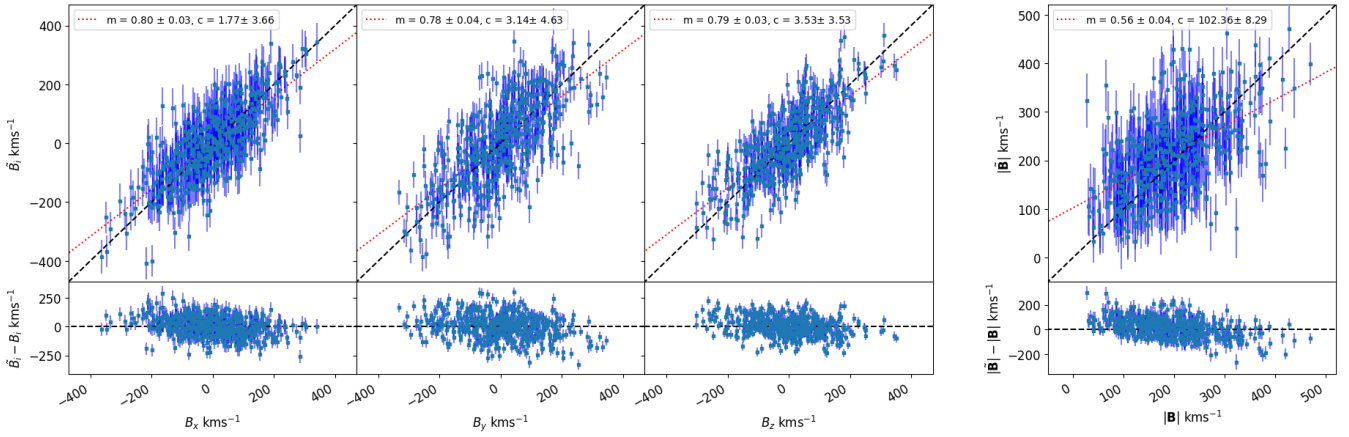


Figure 70: Same as Figure 65, but when $r_c \sim 240 \text{ Mpc} h^{-1}$.

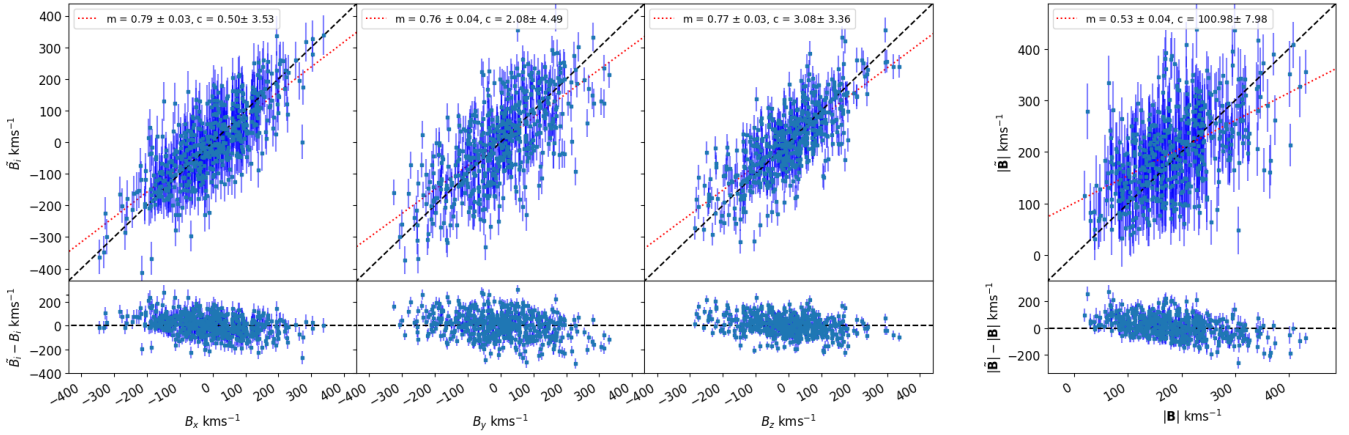


Figure 71: Same as Figure 65, but when $r_c \sim 275 \text{ Mpc} h^{-1}$.

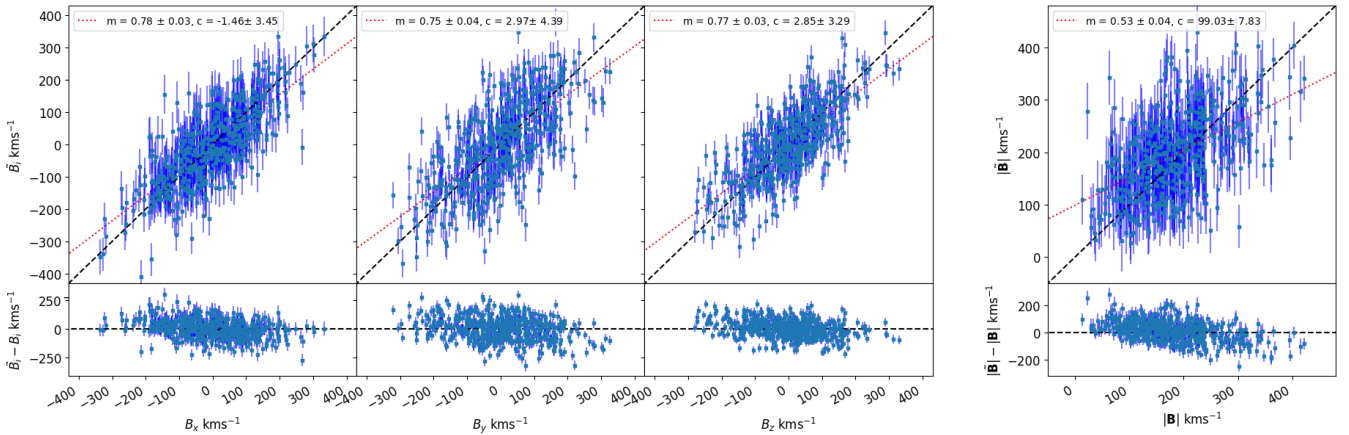


Figure 72: Same as Figure 65, but when $r_c \sim 310 \text{ Mpc} h^{-1}$.

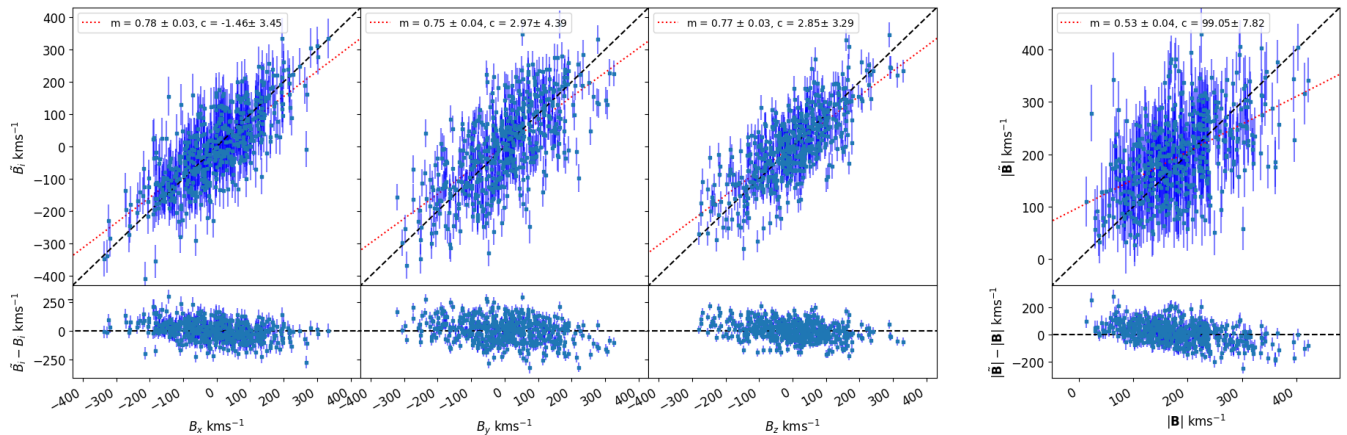


Figure 73: Same as Figure 65, but when $r_c \sim 345$ Mpc h^{-1} .

Kaiser MLE, CF4TF mock data only

Results are shown here for the CF4TF mocks only when applying the Kaiser MLE, for comparison to the same analysis done on the CF4TF part of the data included in the CF4 dataset only. The $\chi^2 \sim 21, 22, 22, 22, 22, 22, 22, 22, 22, 22$ for each radial cut to the data.

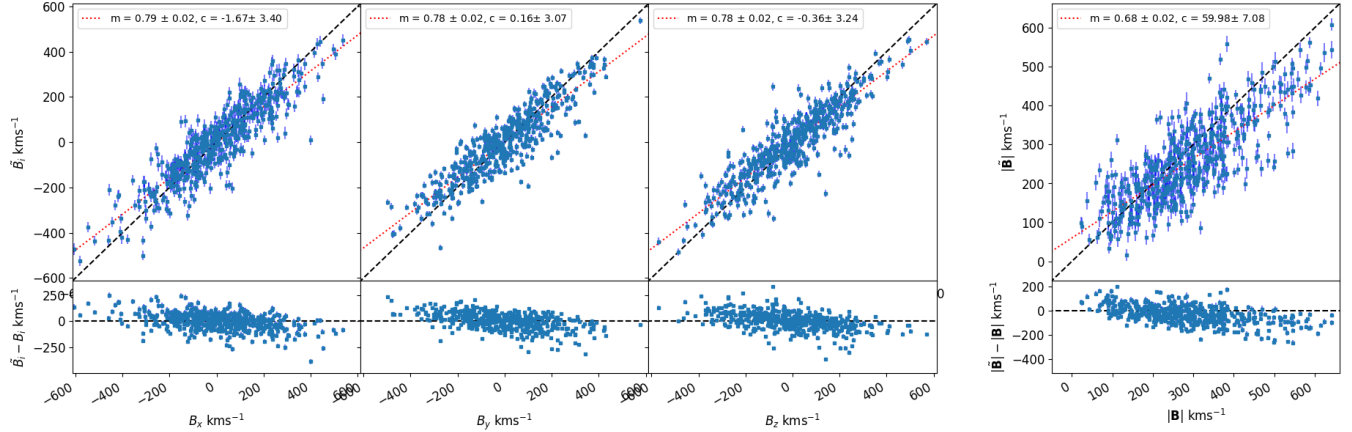


Figure 74: Results applying the Kaiser MLE approach to the CF4TF part of the CF4 mocks, for 512 mocks. Only data at a radial distance that satisfied $\leq 69 \text{ Mpc } h^{-1}$ is included, i.e. $r_c = 69 \text{ Mpc } h^{-1}$.

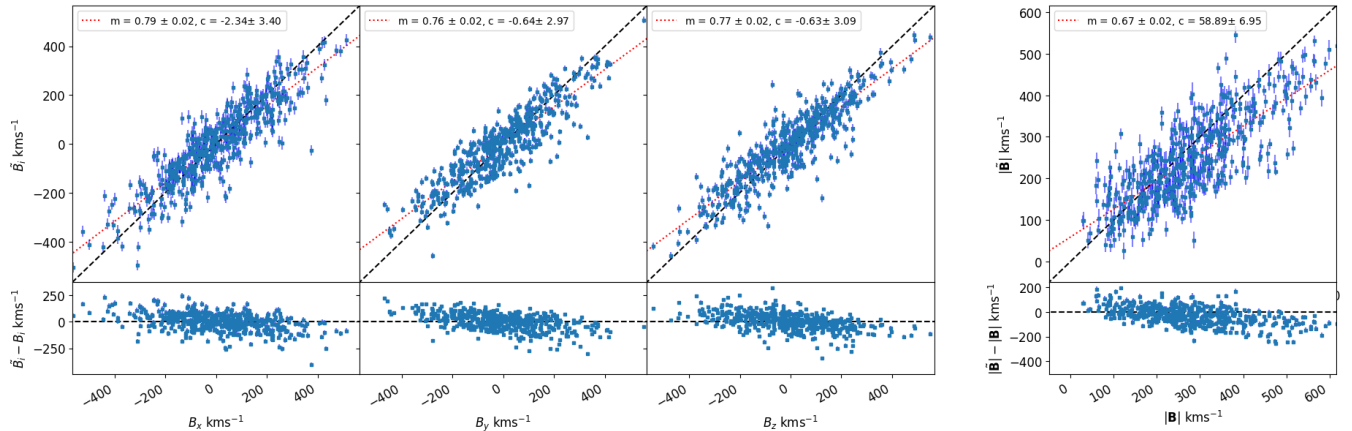


Figure 75: Same as Figure 74, but when $r_c \sim 100 \text{ Mpc} h^{-1}$.

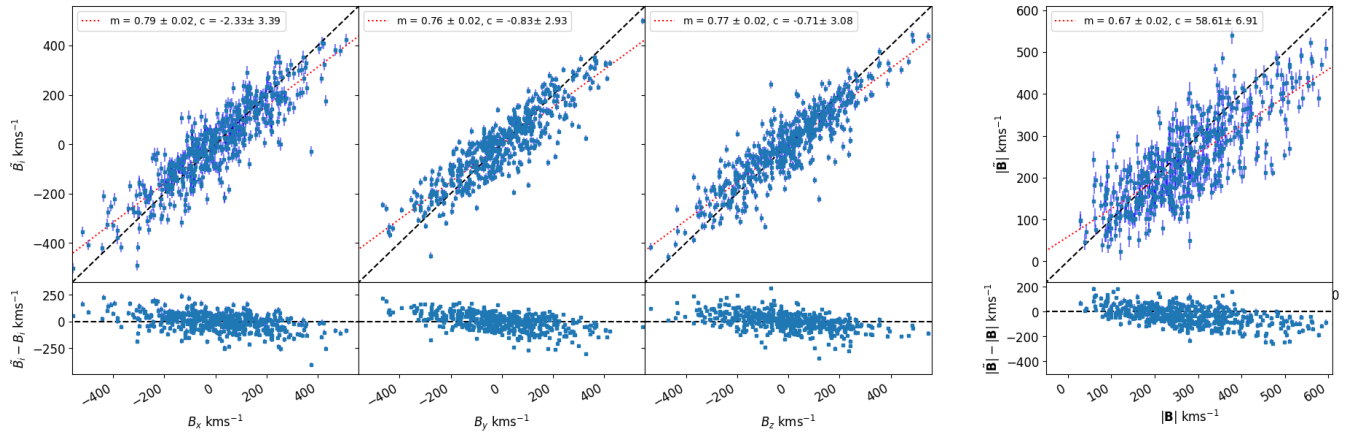


Figure 76: Same as Figure 74, but when $r_c \sim 140 \text{ Mpc} h^{-1}$.

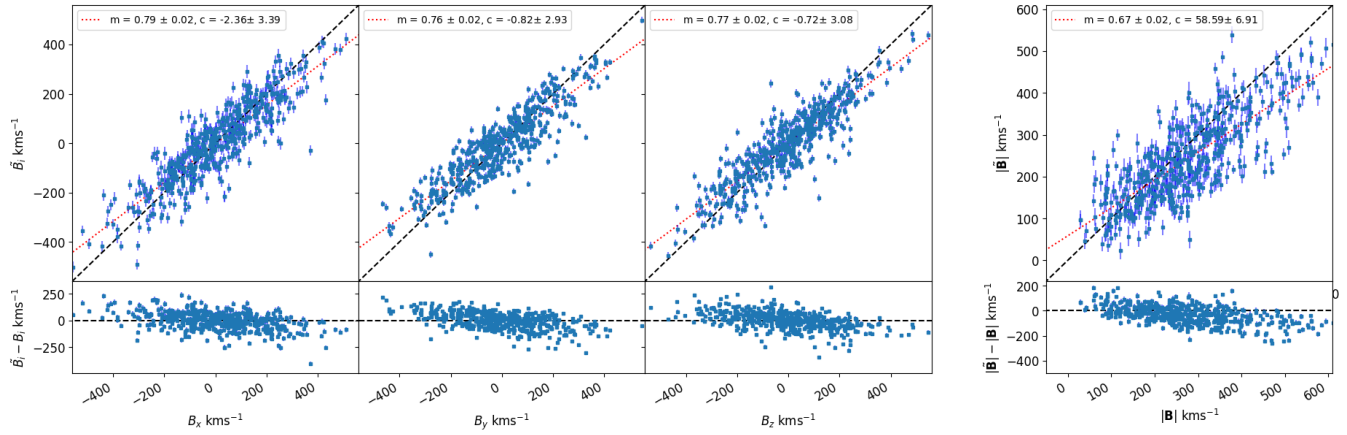


Figure 77: Same as Figure 74, but when $r_c \sim 170 \text{ Mpc} h^{-1}$.

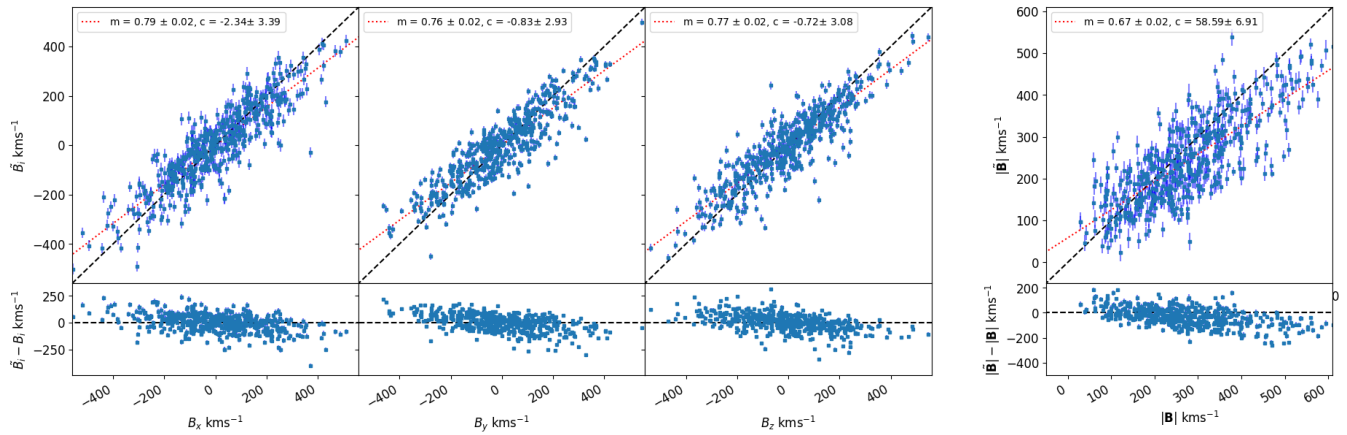


Figure 78: Same as Figure 74, but when $r_c \sim 210 \text{ Mpc} h^{-1}$.

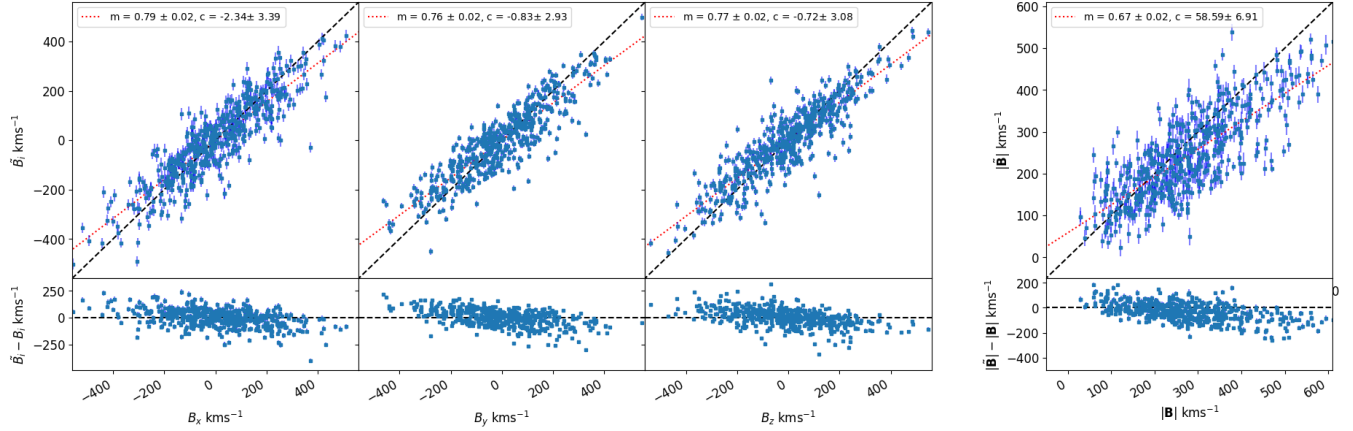


Figure 79: Same as Figure 74, but when $r_c \sim 240 \text{ Mpc} h^{-1}$.

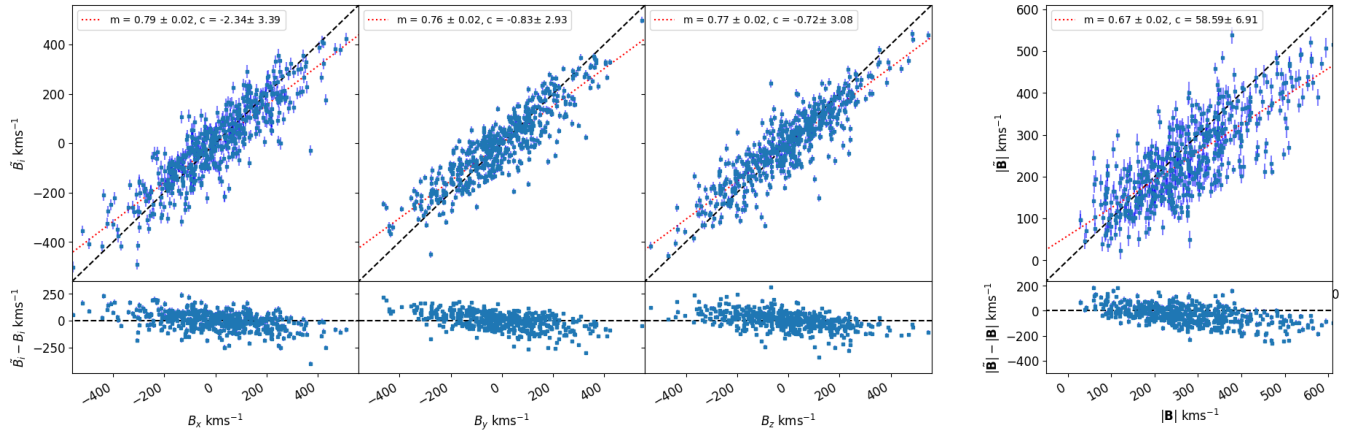


Figure 80: Same as Figure 74, but when $r_c \sim 275 \text{ Mpc} h^{-1}$.

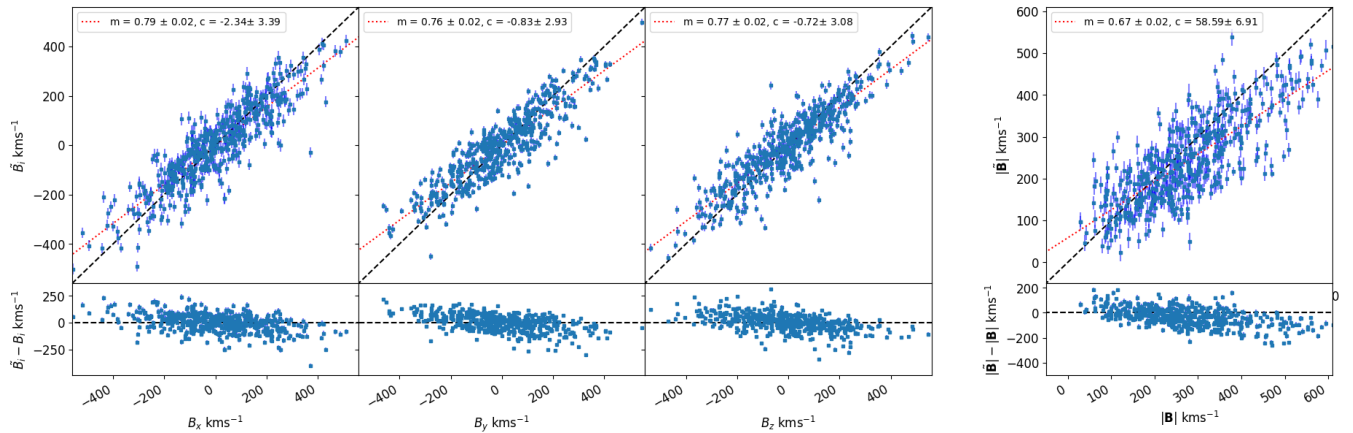


Figure 81: Same as Figure 74, but when $r_c \sim 310 \text{ Mpc} h^{-1}$.

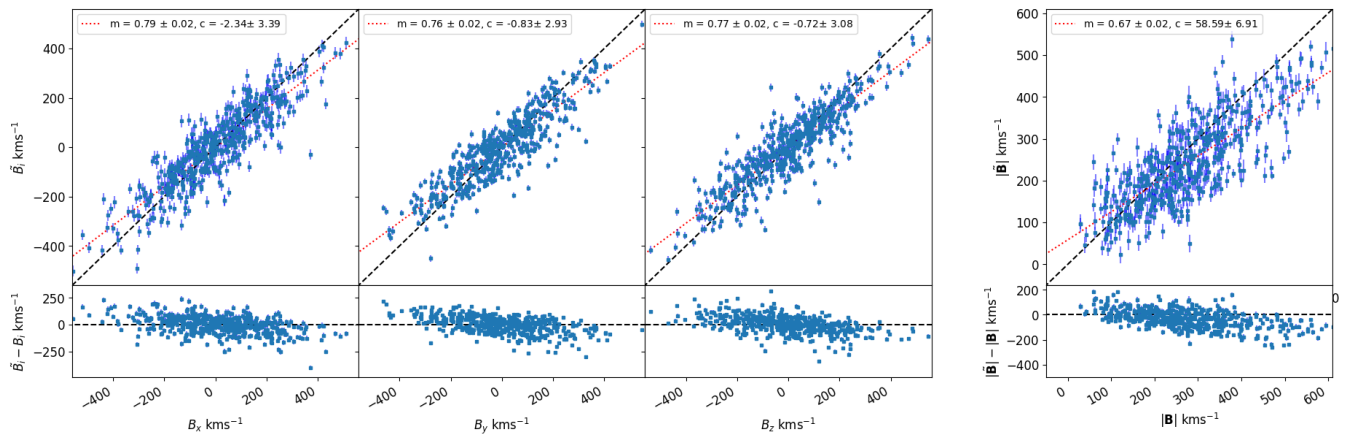


Figure 82: Same as Figure 74, but when $r_c \sim 345 \text{ Mpc} h^{-1}$.

Kaiser MLE, 6dFGSv mock data only

Results are shown here for the 6dFGSv mocks only when applying the Kaiser MLE, for comparison to the same analysis done on the 6dFGSv part of the data included in the CF4 dataset only. The $\chi^2 \sim 4, 5, 4.6, 4.5, 4.5, 4.5, 4.5, 4.5, 4.5$ for each radial cut to the data.

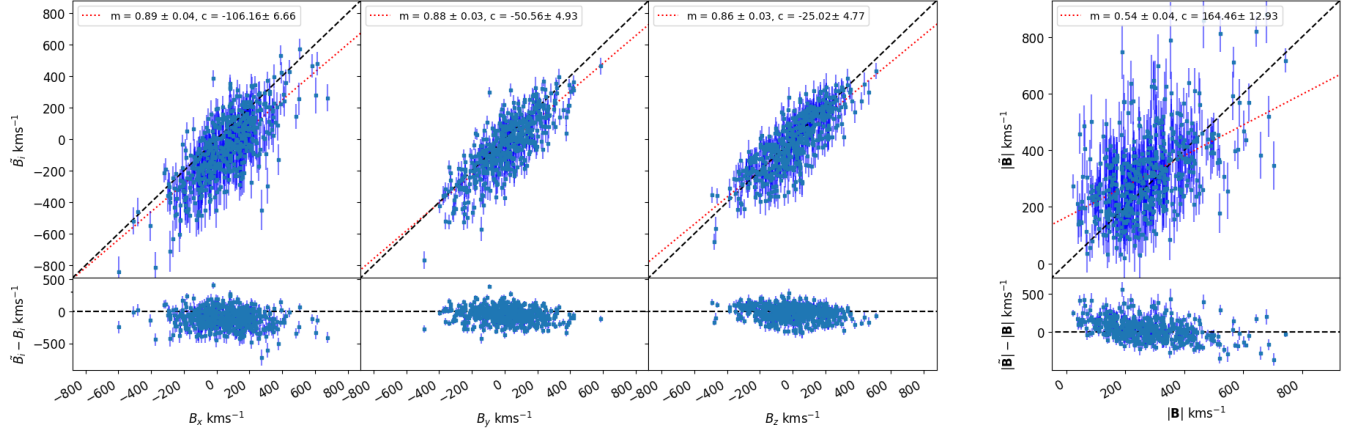


Figure 83: Results applying the Kaiser MLE approach to the 6dFGSv part of the CF4 mocks in the mock data, for 512 mocks. Only data at a radial distance that satisfied $\leq 69 \text{ Mpc } h^{-1}$ is included, i.e. $r_c = 69 \text{ Mpc } h^{-1}$.

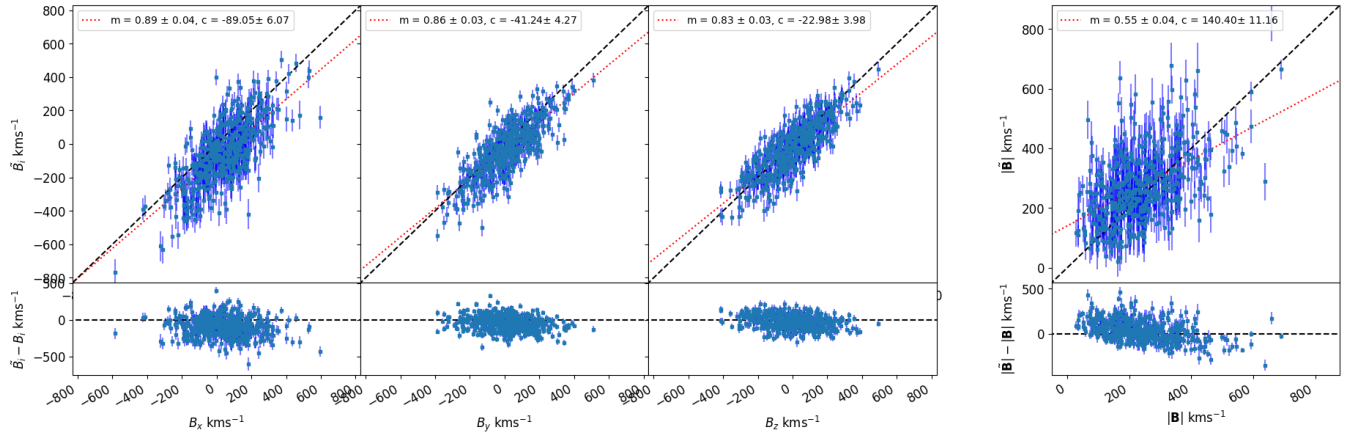


Figure 84: Same as Figure 83, but when $r_c \sim 100 \text{ Mpc} h^{-1}$.

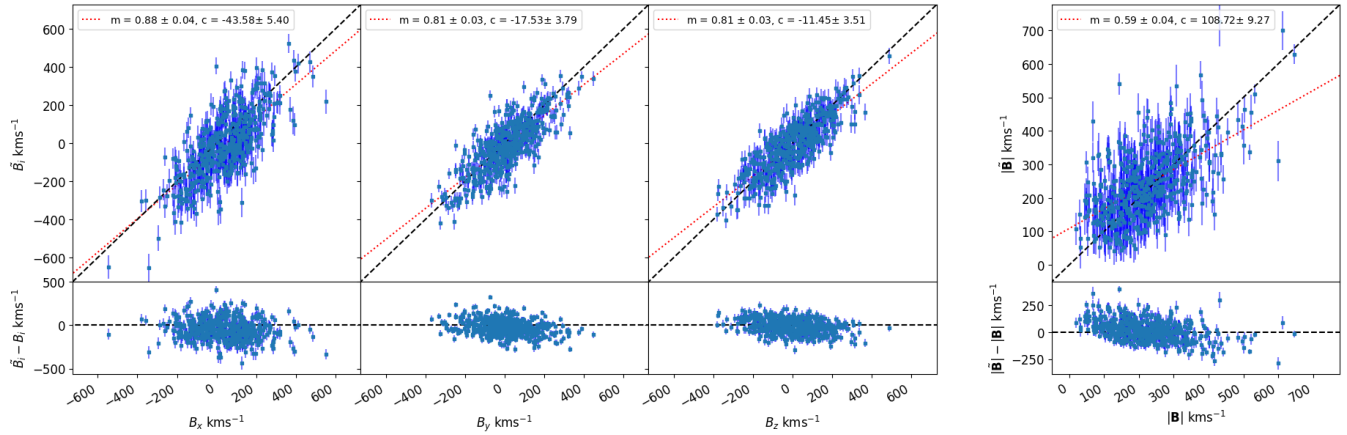


Figure 85: Same as Figure 83, but when $r_c \sim 140 \text{ Mpc} h^{-1}$.

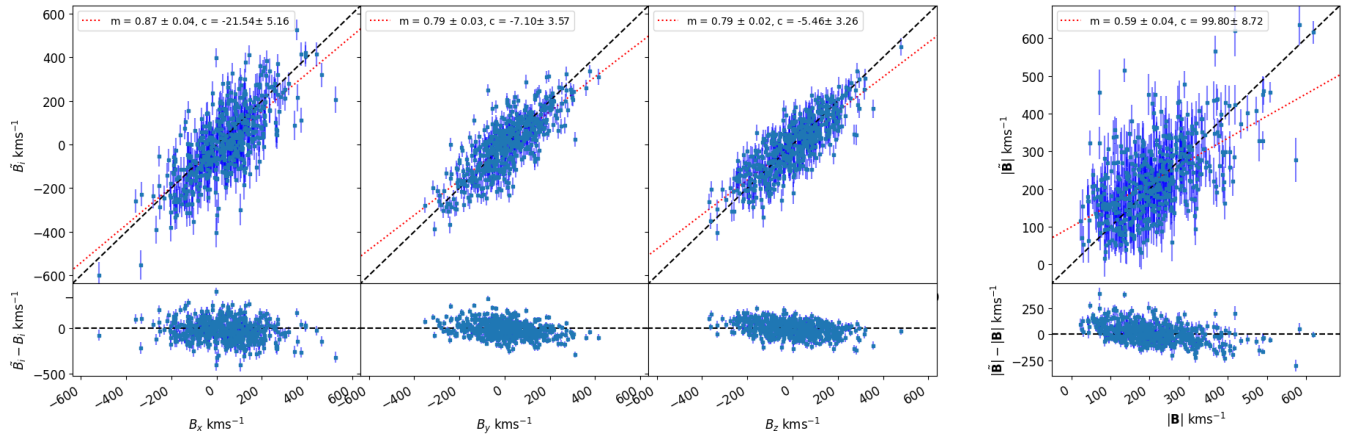


Figure 86: Same as Figure 83, but when $r_c \sim 170 \text{ Mpc} h^{-1}$.

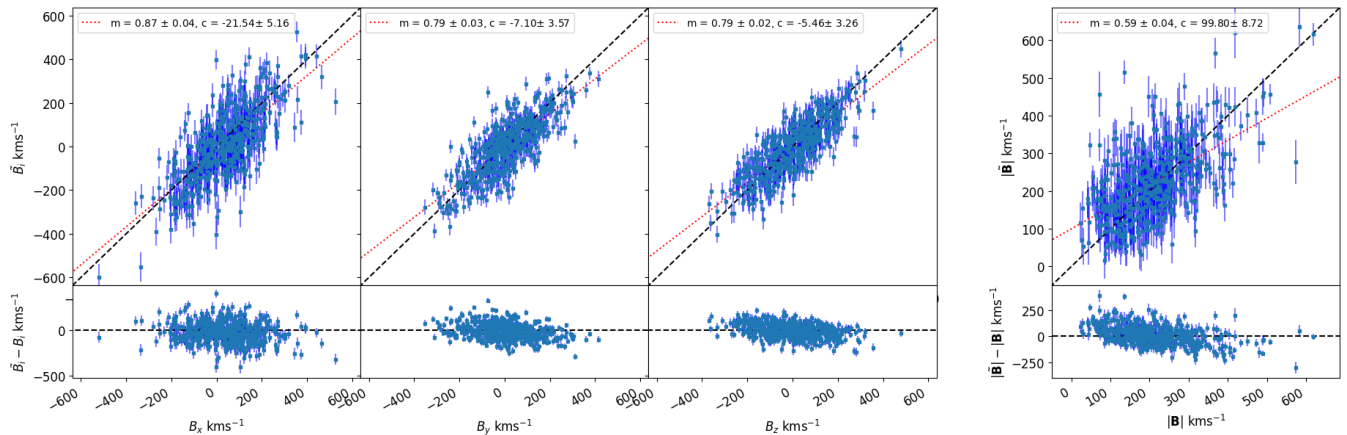


Figure 87: Same as Figure 83, but when $r_c \sim 210 \text{ Mpc} h^{-1}$.

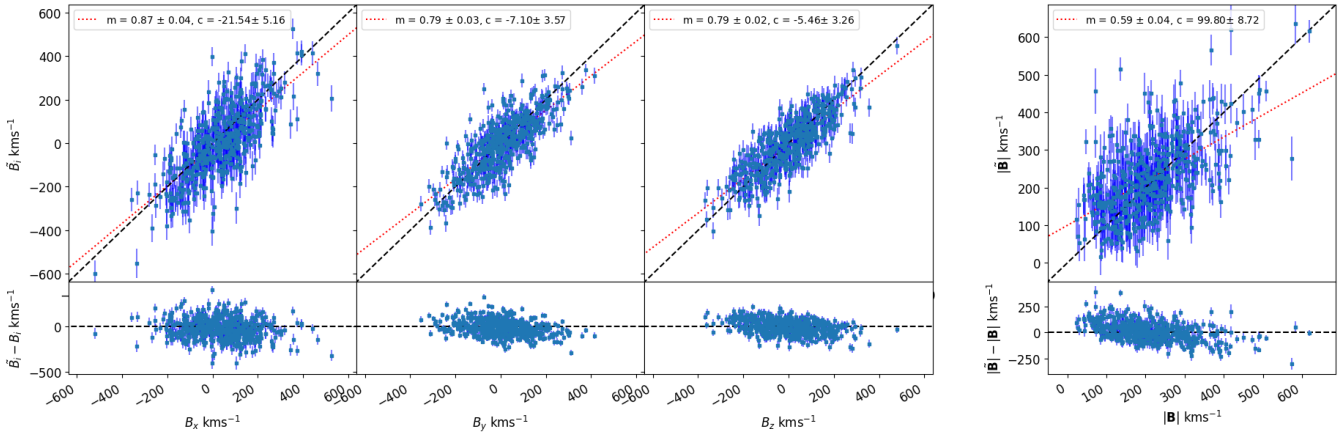


Figure 88: Same as Figure 83, but when $r_c \sim 240 \text{ Mpc} h^{-1}$.

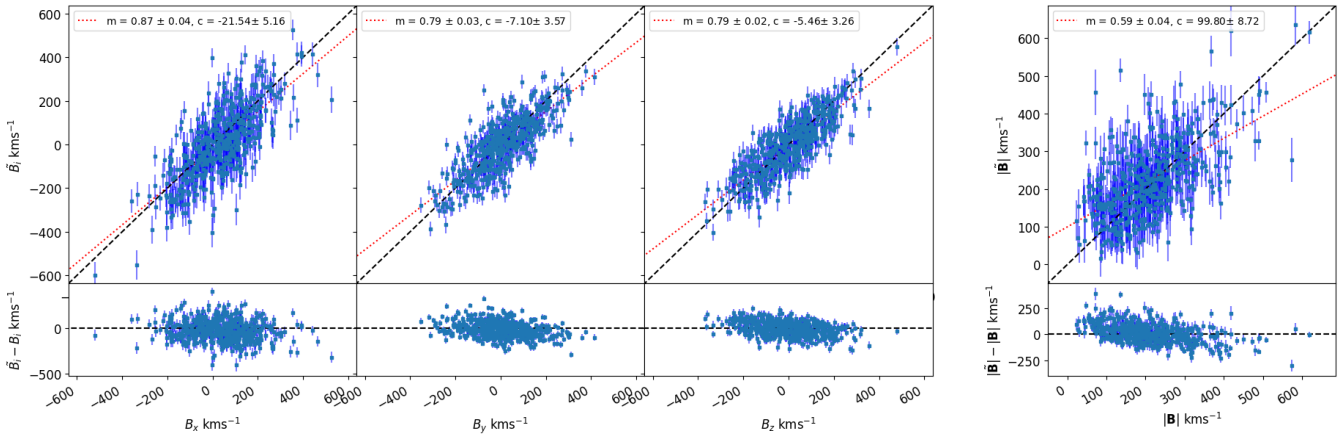


Figure 89: Same as Figure 83, but when $r_c \sim 275 \text{ Mpc} h^{-1}$.

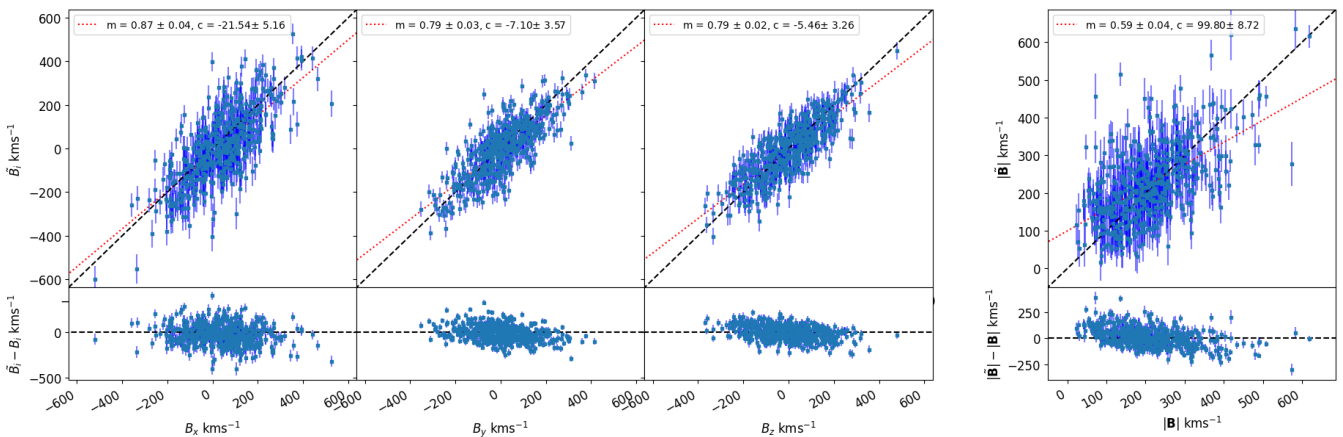


Figure 90: Same as Figure 83, but when $r_c \sim 310 \text{ Mpc} h^{-1}$.

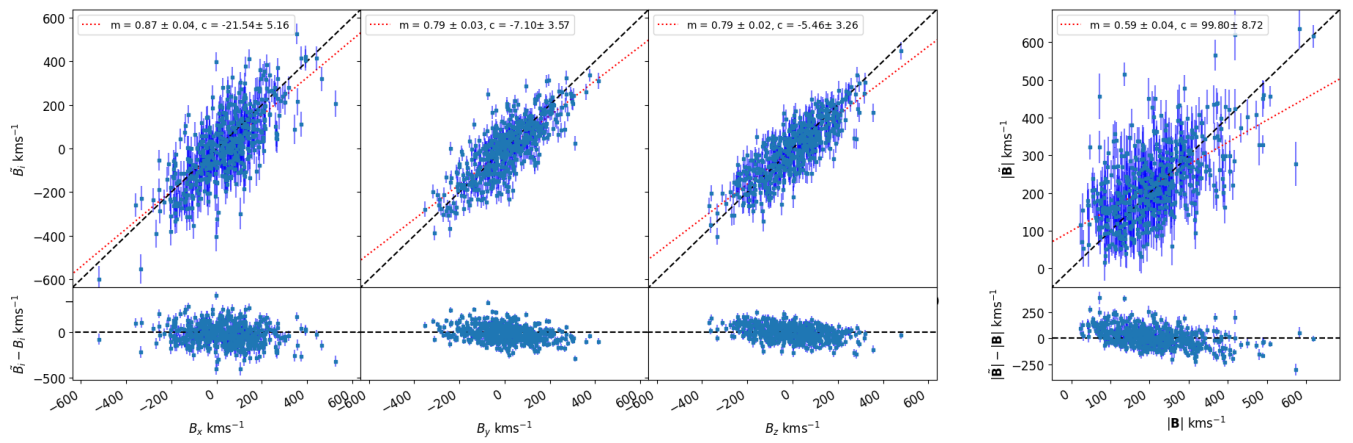


Figure 91: Same as Figure 83, but when $r_c \sim 345$ Mpc h^{-1} .

Peery MVE, SDSS mock data only

Results are shown here for the SDSS mocks only when applying the Peery MVE, for comparison to the same analysis done on the SDSS part of the data included in the CF4 dataset only. The $\chi^2 \sim 2.4, 2.4, 2.3, 2.3, 2.2, 2.1, 2.1, 2.1, 2.1$ for each ideal survey radii tested.

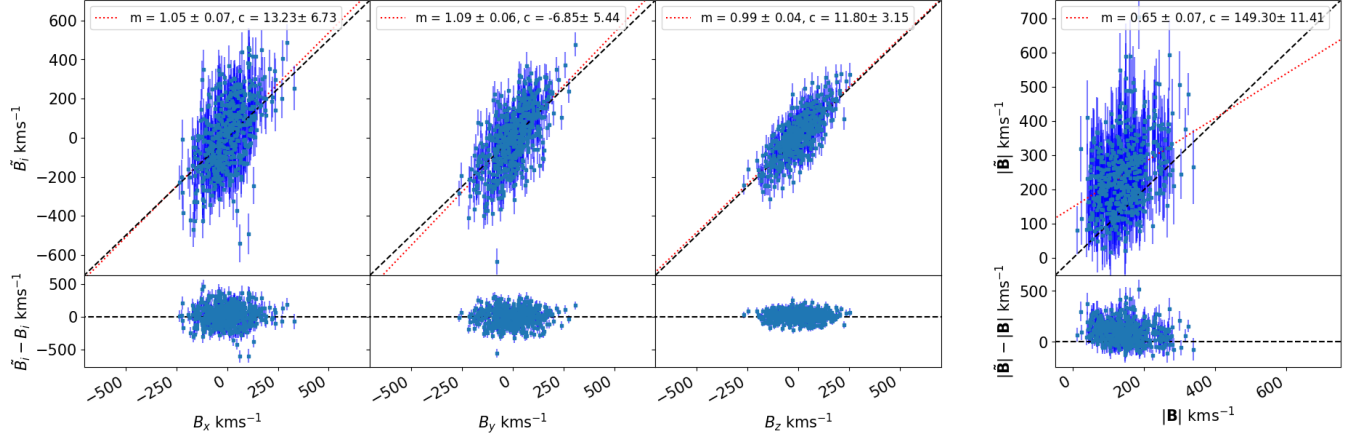


Figure 92: Results applying the Peery MVE approach to the SDSS part of the CF4 mocks in the mock data, for 512 mocks. A radius of $69 \text{ Mpc} h^{-1}$ for the ideal survey has been applied.

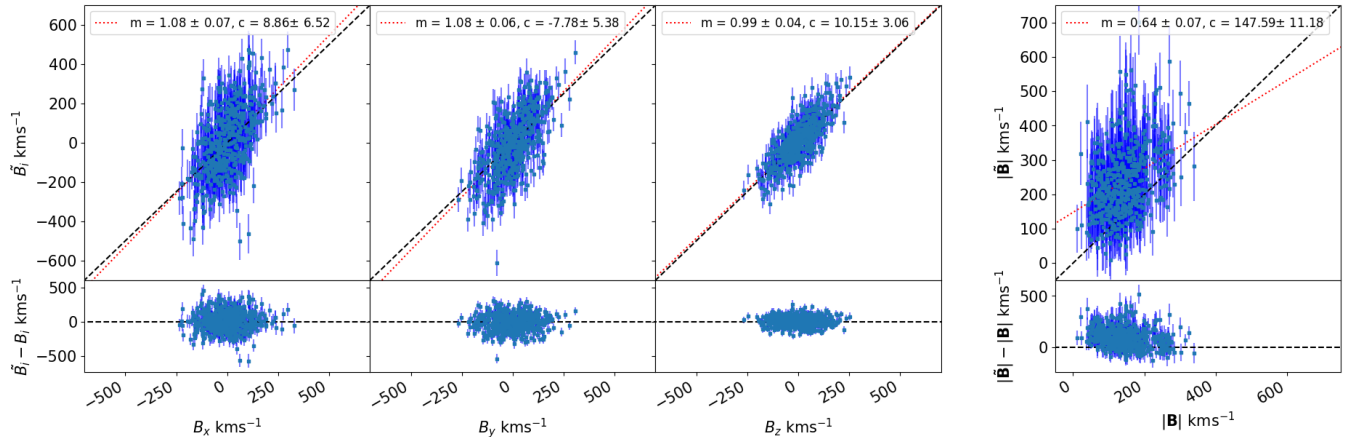


Figure 93: Same as Figure 92, but when a radius for the ideal survey of $100 \text{ Mpc} h^{-1}$ has been applied.

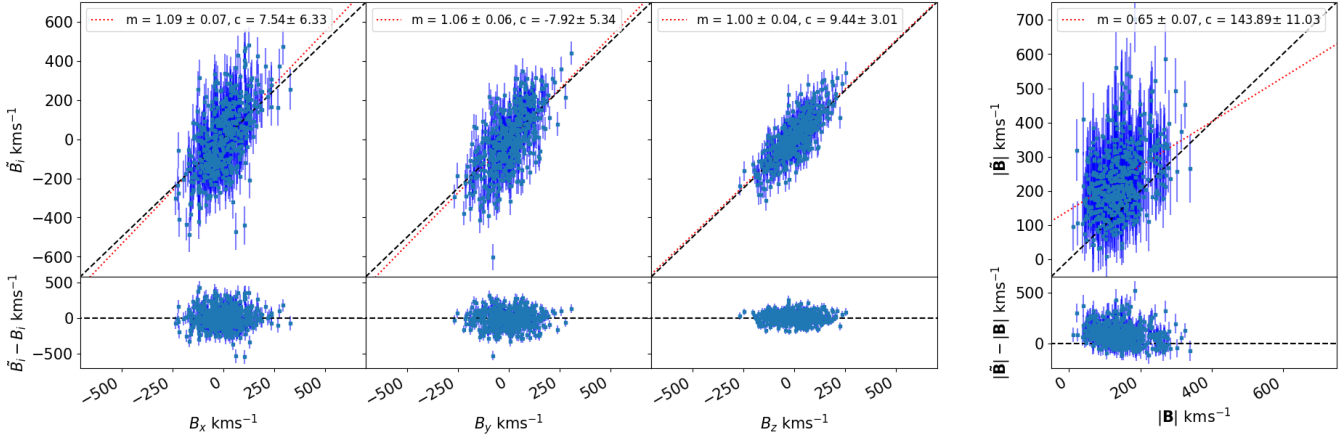


Figure 94: Same as Figure 92, but when a radius for the ideal survey of $140 \text{ Mpc}h^{-1}$ has been applied.

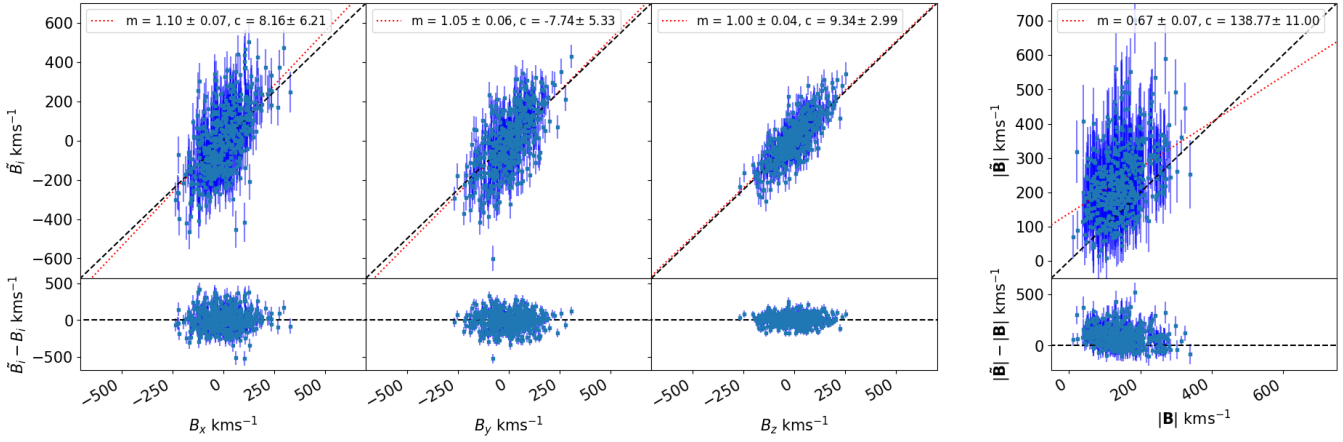


Figure 95: Same as Figure 92, but when a radius for the ideal survey of $170 \text{ Mpc}h^{-1}$ has been applied.

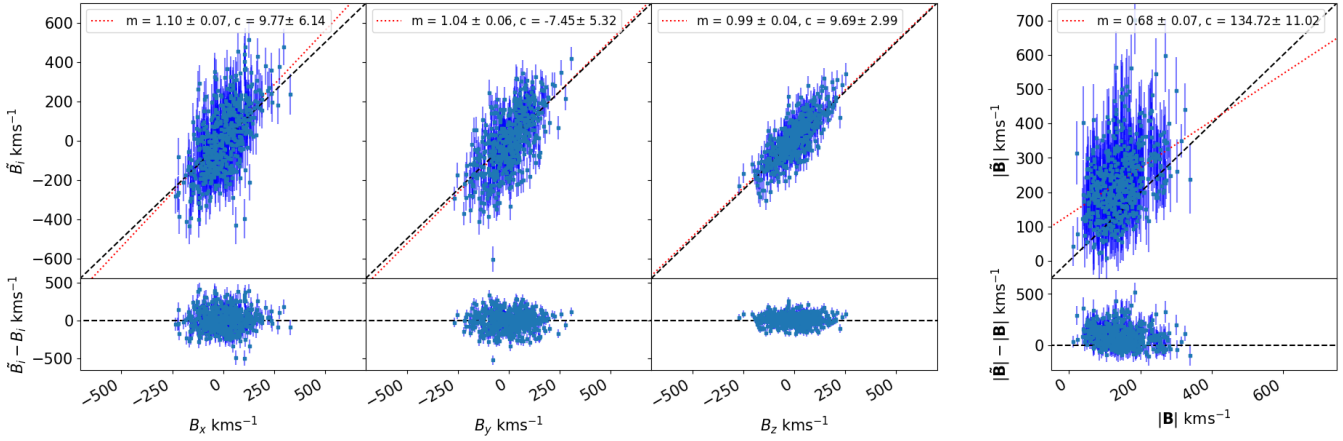


Figure 96: Same as Figure 92, but when a radius for the ideal survey of $210 \text{ Mpc}h^{-1}$ has been applied.

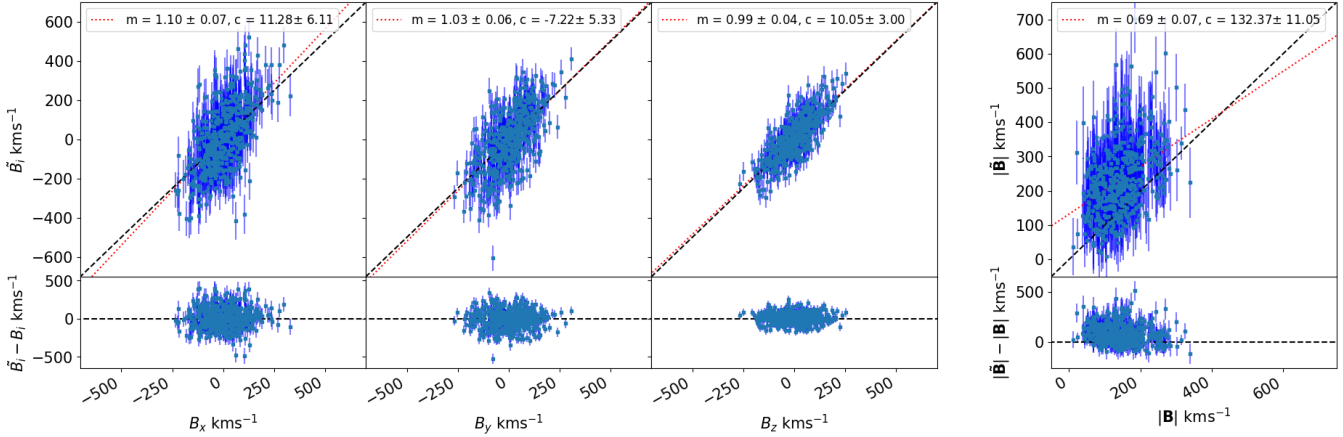


Figure 97: Same as Figure 92, but when a radius for the ideal survey of $240 \text{ Mpc} h^{-1}$ has been applied.

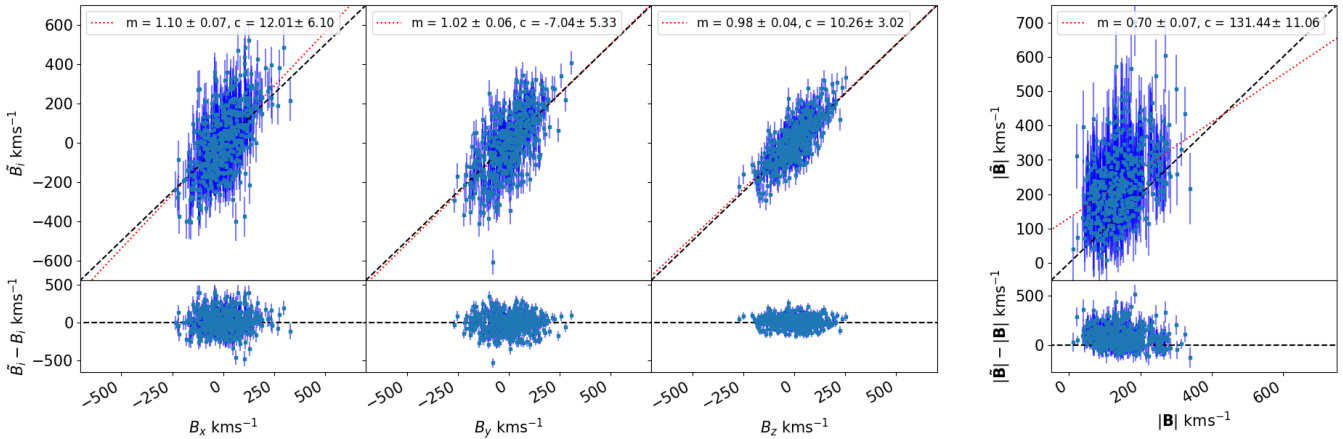


Figure 98: Same as Figure 92, but when a radius for the ideal survey of $275 \text{ Mpc} h^{-1}$ has been applied.

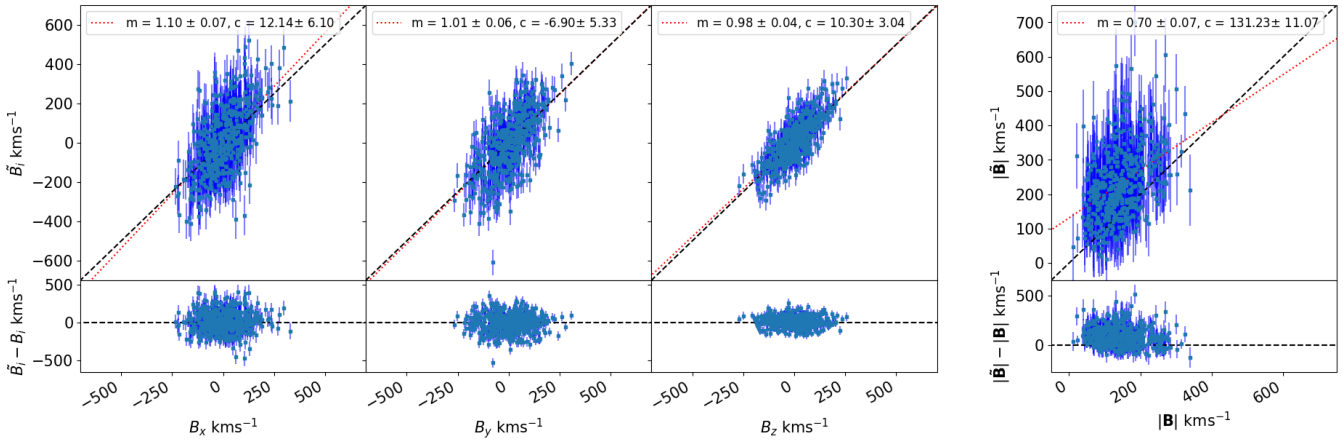


Figure 99: Same as Figure 92, but when a radius for the ideal survey of $310 \text{ Mpc} h^{-1}$ has been applied.

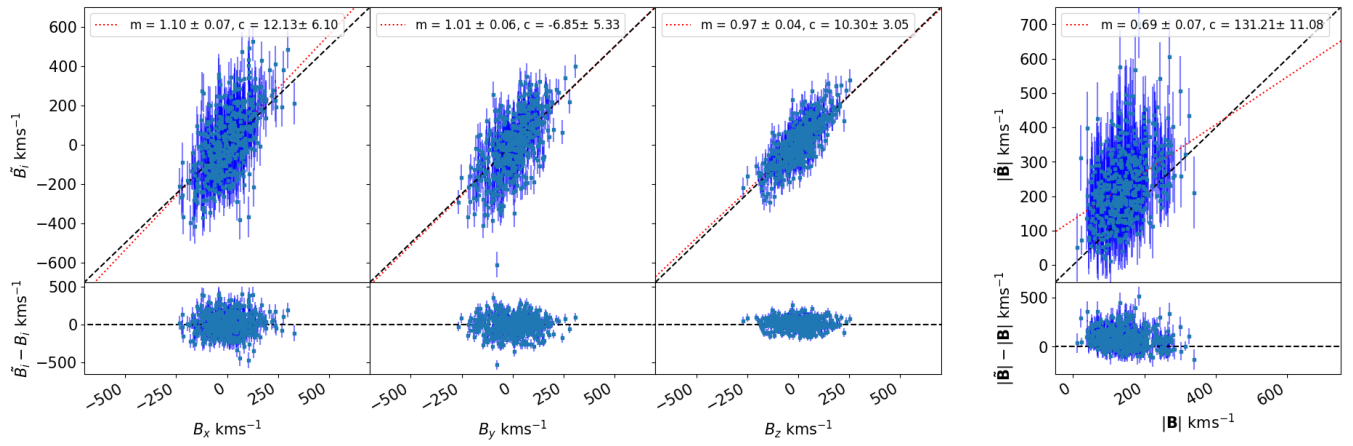


Figure 100: Same as Figure 92, but when a radius for the ideal survey of $345 \text{ Mpc} h^{-1}$ has been applied.

Peery MVE, CF4TF mock data only

Results are shown here for the CF4TF mocks only when applying the Peery MVE, for comparison to the same analysis done on the CF4TF part of the data included in the CF4 dataset only. The $\chi^2 \sim 4.3, 4.2, 4.1, 4.0, 4.0, 4.0, 4.0, 4.0, 4.0$ for each ideal survey radii tested.

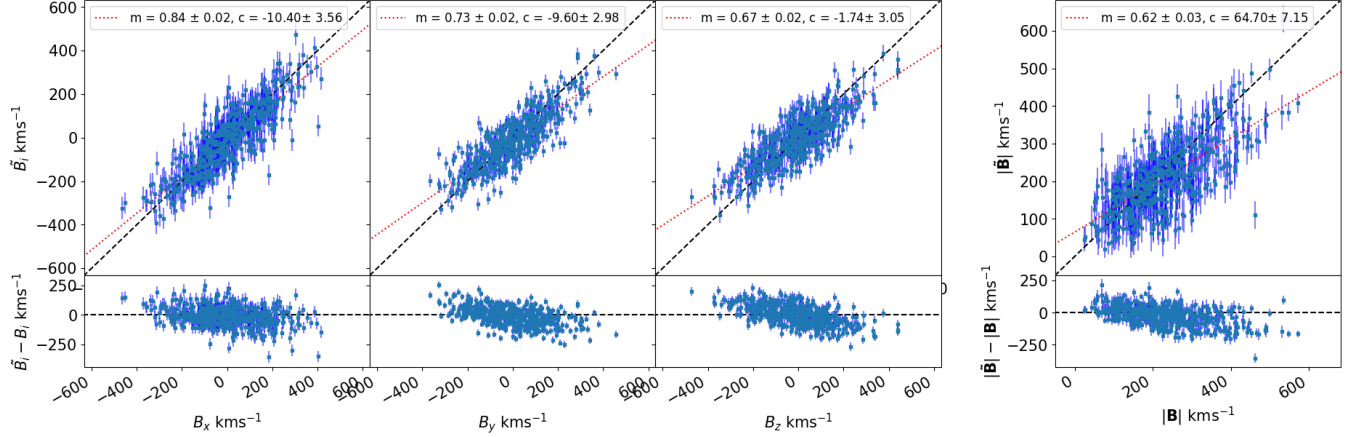


Figure 101: Results applying the Peery MVE approach to the CF4TF part of the CF4 mocks in the mock data, for 512 mocks. A radius of $69 \text{ Mpc} h^{-1}$ for the ideal survey has been applied.

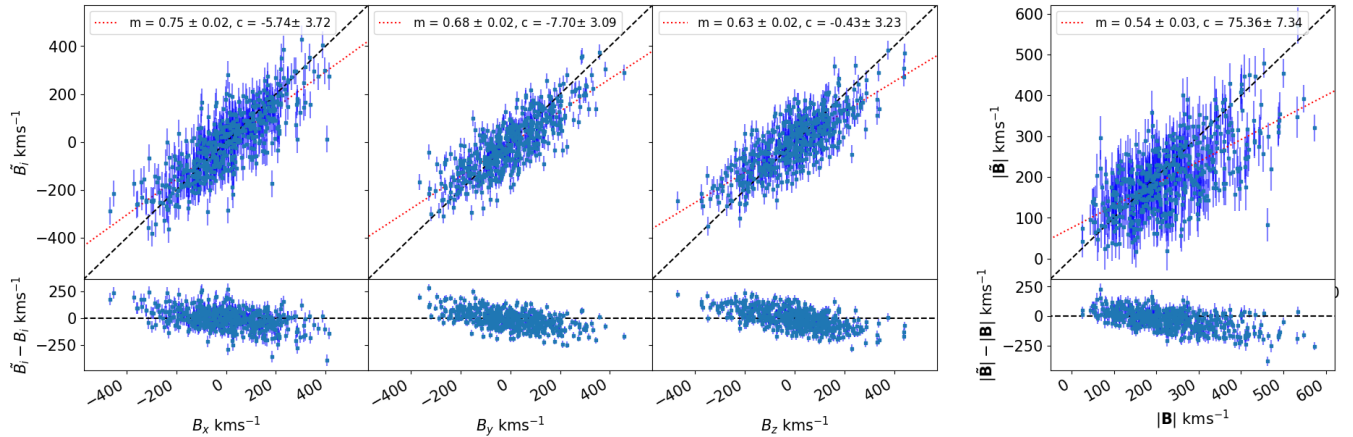


Figure 102: Same as Figure 101, but when a radius for the ideal survey of $100 \text{ Mpc} h^{-1}$ has been applied.

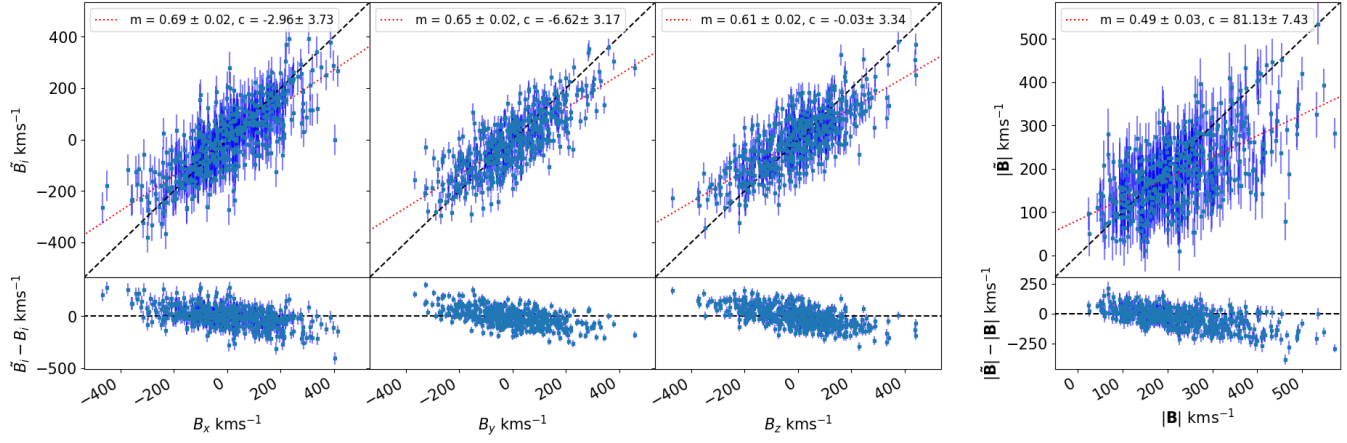


Figure 103: Same as Figure 101, but when a radius for the ideal survey of $140 \text{ Mpc} h^{-1}$ has been applied.

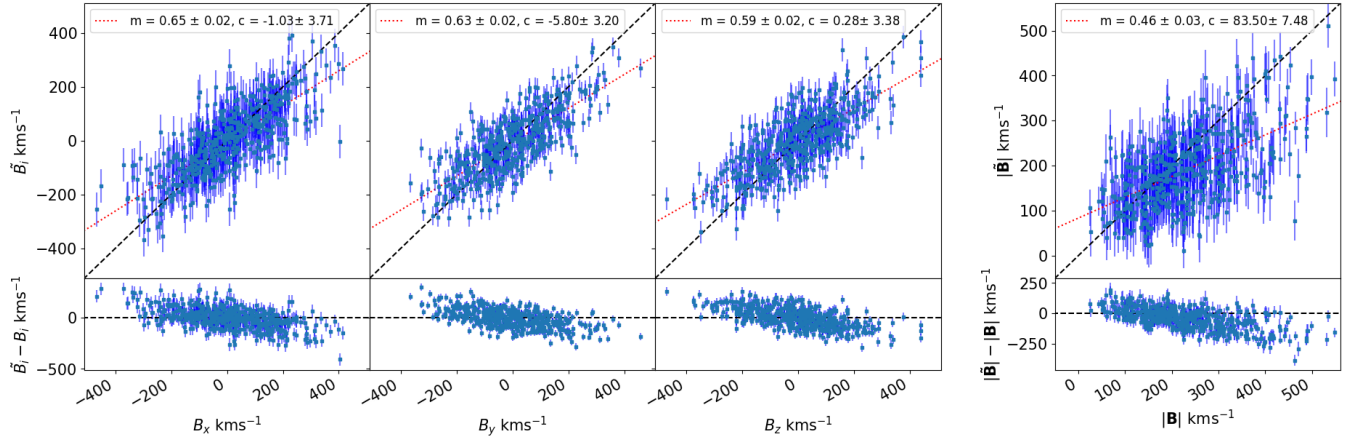


Figure 104: Same as Figure 101, but when a radius for the ideal survey of $170 \text{ Mpc} h^{-1}$ has been applied.

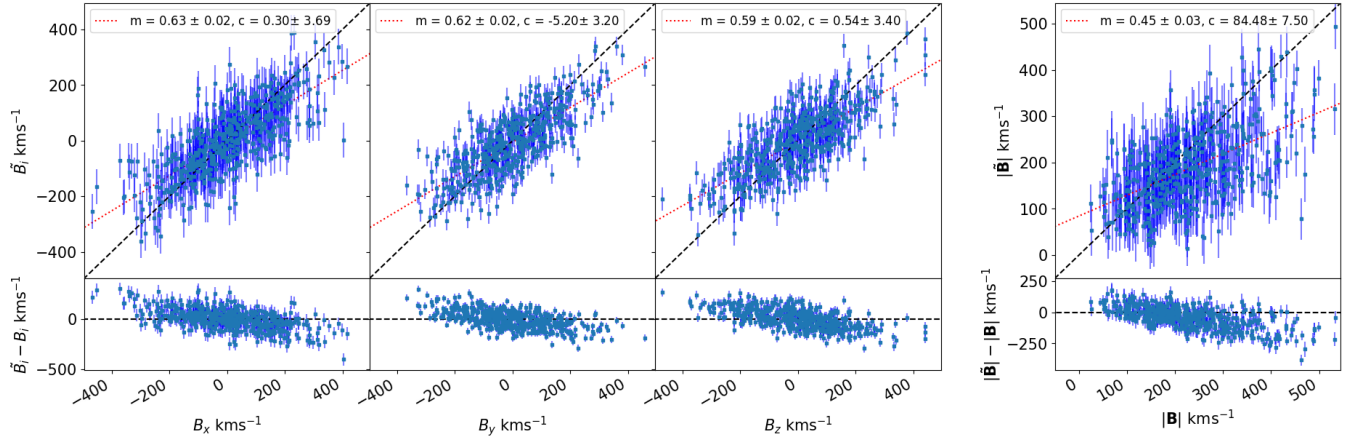


Figure 105: Same as Figure 101, but when a radius for the ideal survey of $210 \text{ Mpc} h^{-1}$ has been applied.

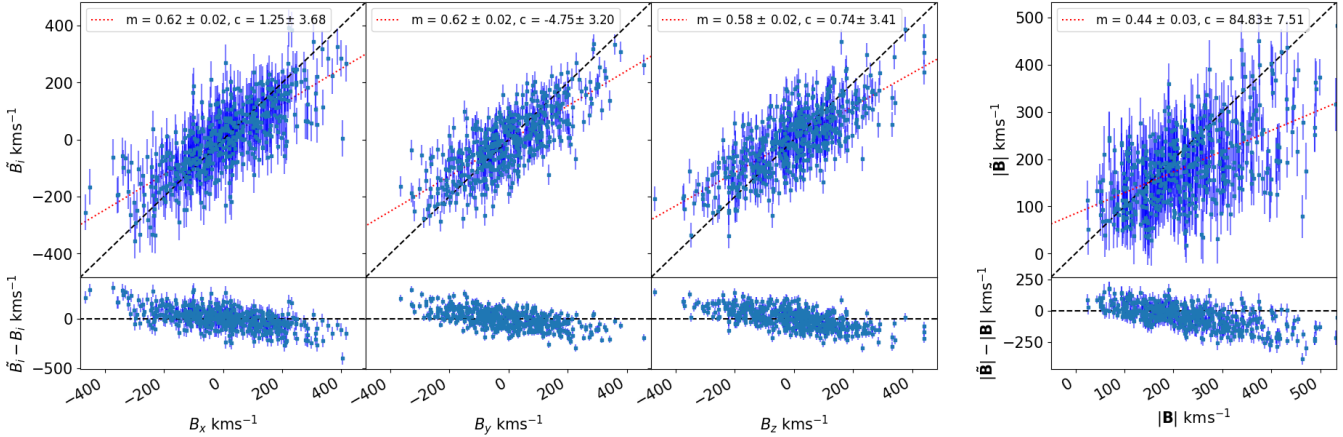


Figure 106: Same as Figure 101, but when a radius for the ideal survey of $240 \text{ Mpc} h^{-1}$ has been applied.

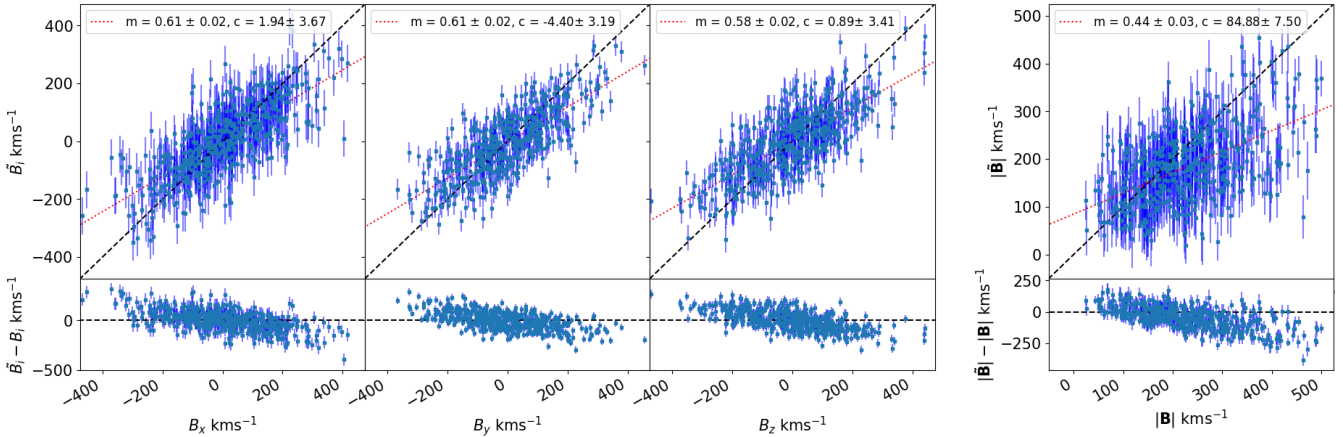


Figure 107: Same as Figure 101, but when a radius for the ideal survey of $275 \text{ Mpc} h^{-1}$ has been applied.

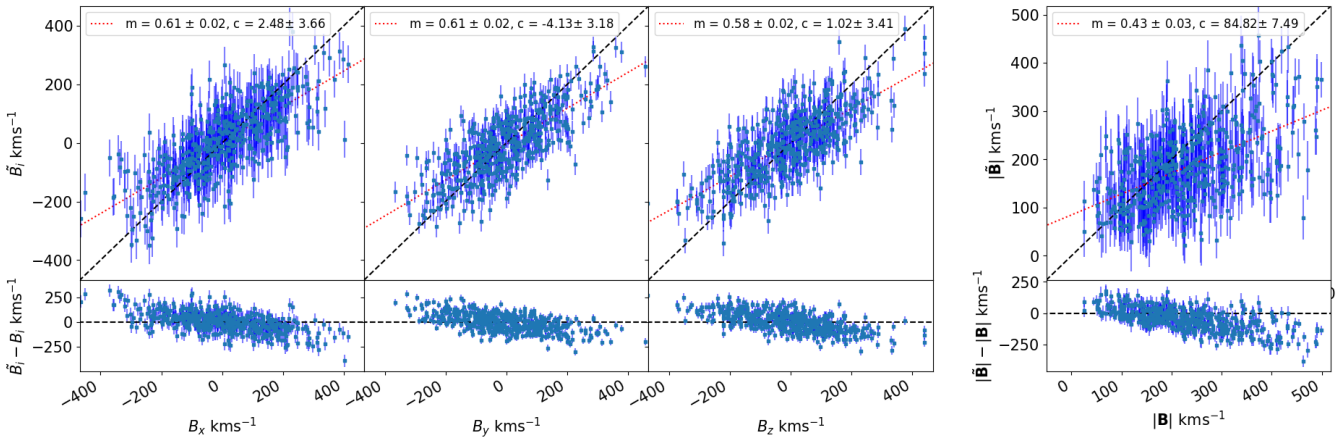


Figure 108: Same as Figure 101, but when a radius for the ideal survey of $310 \text{ Mpc} h^{-1}$ has been applied.

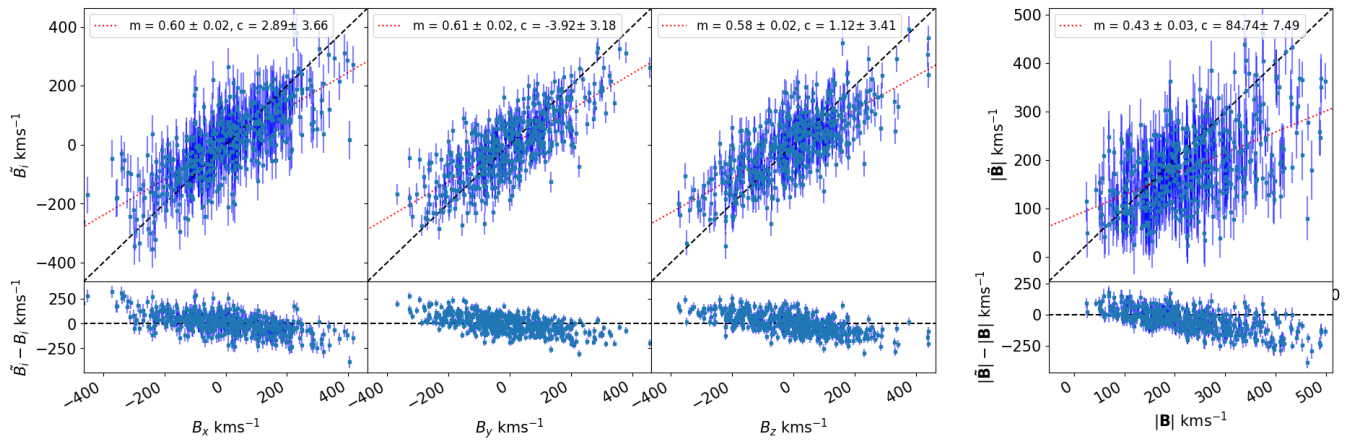


Figure 109: Same as Figure 101, but when a radius for the ideal survey of $345 \text{ Mpc}h^{-1}$ has been applied.

Peery MVE, 6dFGSv mock data only

Results are shown here for the 6dFGSv mocks only when applying the Peery MVE, for comparison to the same analysis done on the 6dFGSv part of the data included in the CF4 dataset only. The $\chi^2 \sim 1.6$ for each choice of the ideal radius that was tested.

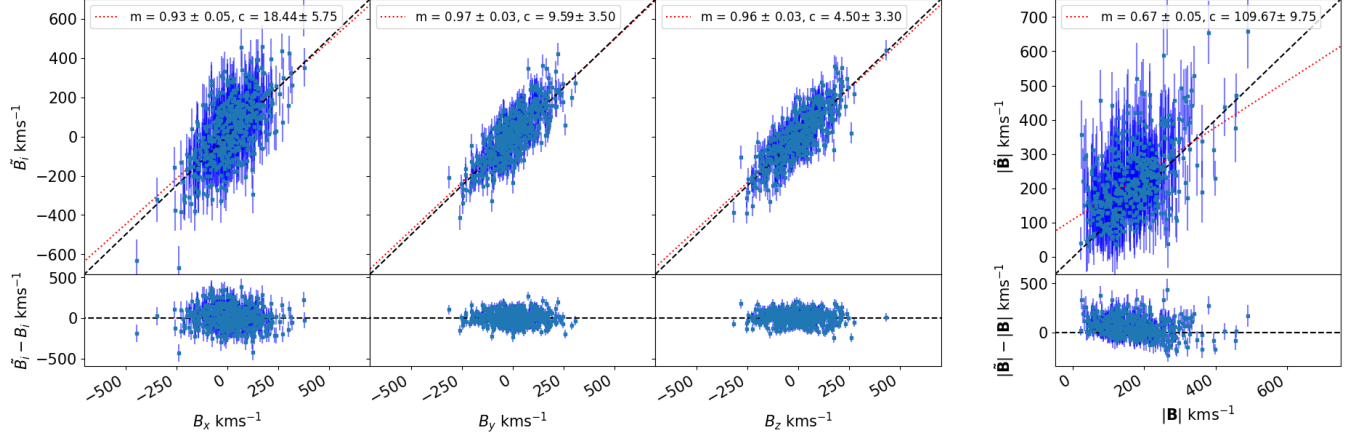


Figure 110: Results applying the Peery MVE approach to the 6dFGSv part of the CF4 mocks in the mock data, for 512 mocks. For the ideal survey a radius of $69 \text{ Mpc}h^{-1}$ has been applied.

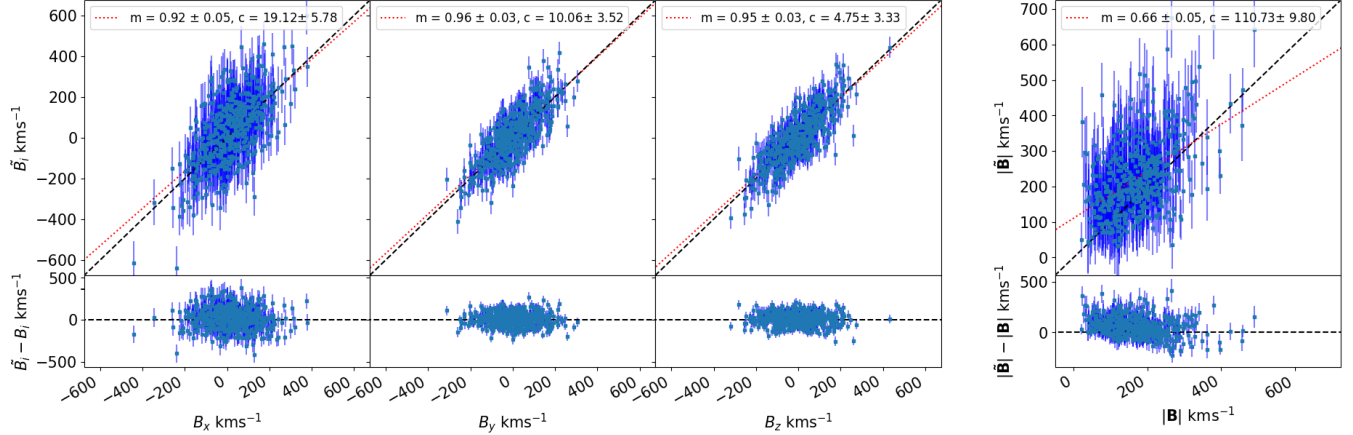


Figure 111: Same as Figure 110, but when the radius of the ideal survey is $100 \text{ Mpc}h^{-1}$.

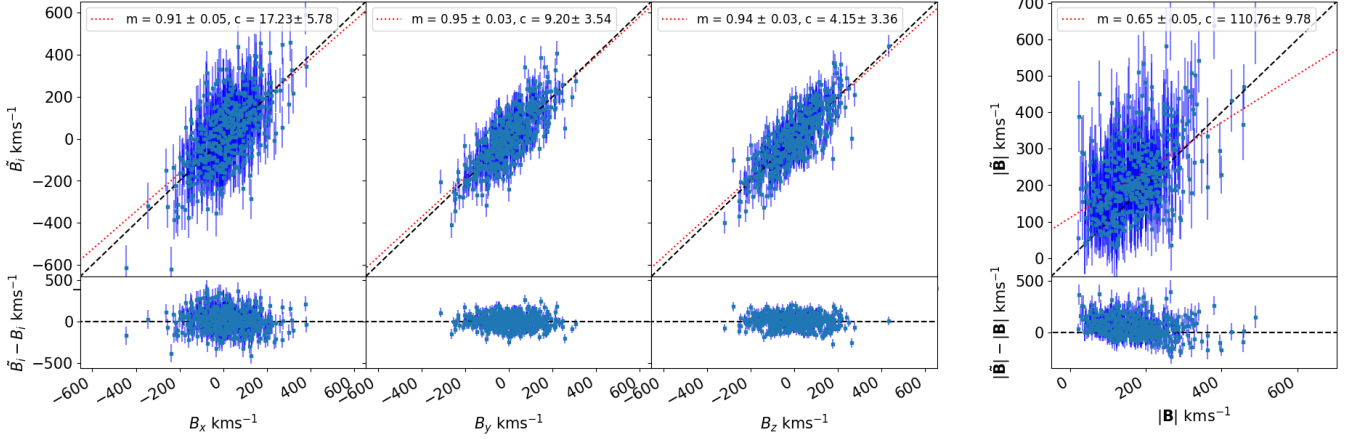


Figure 112: Same as Figure 110, but when the radius of the ideal survey is $140 \text{ Mpc} h^{-1}$.

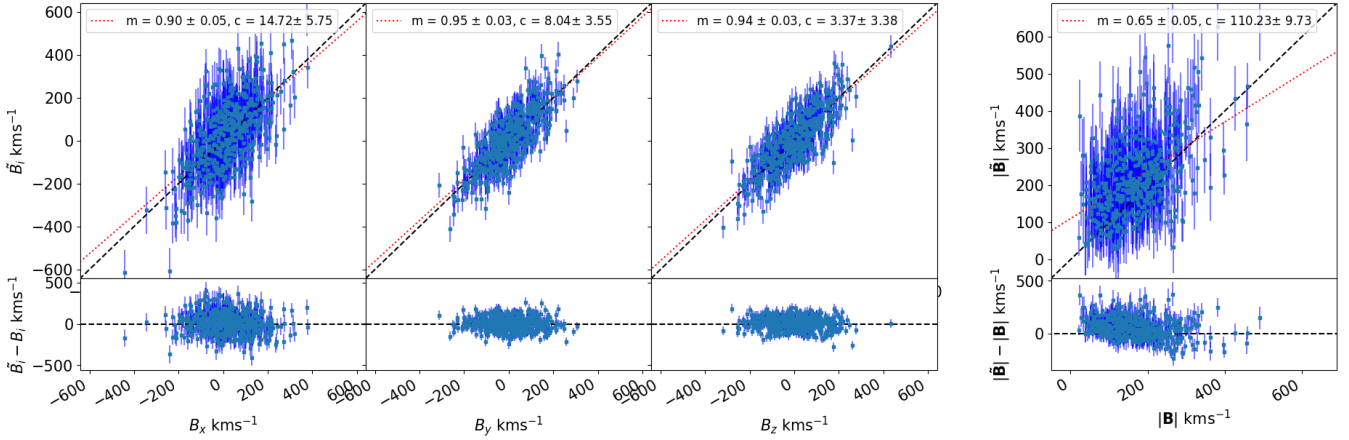


Figure 113: Same as Figure 110, but when the radius of the ideal survey is $170 \text{ Mpc} h^{-1}$.

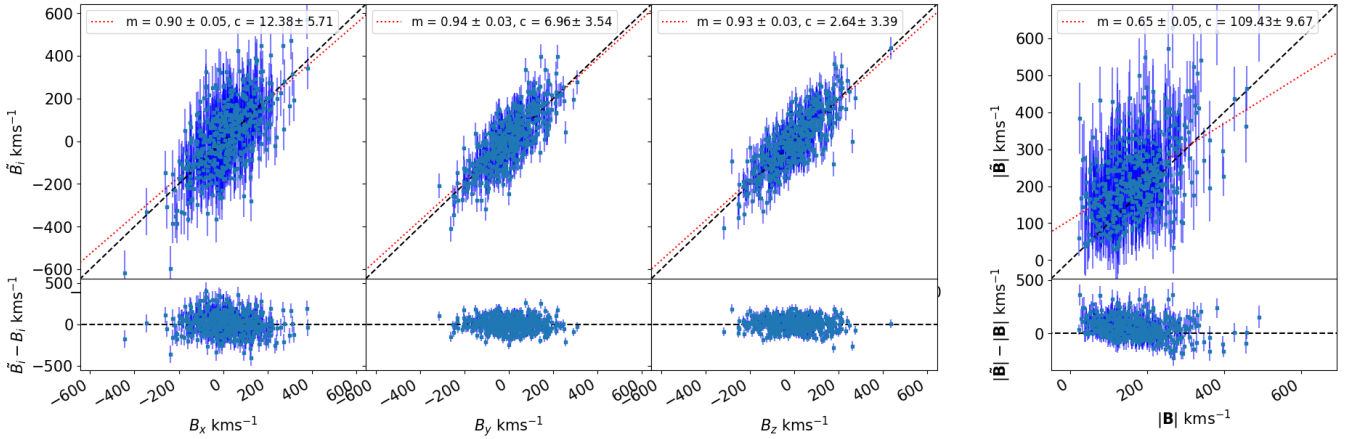


Figure 114: Same as Figure 110, but when the radius of the ideal survey is $210 \text{ Mpc} h^{-1}$.

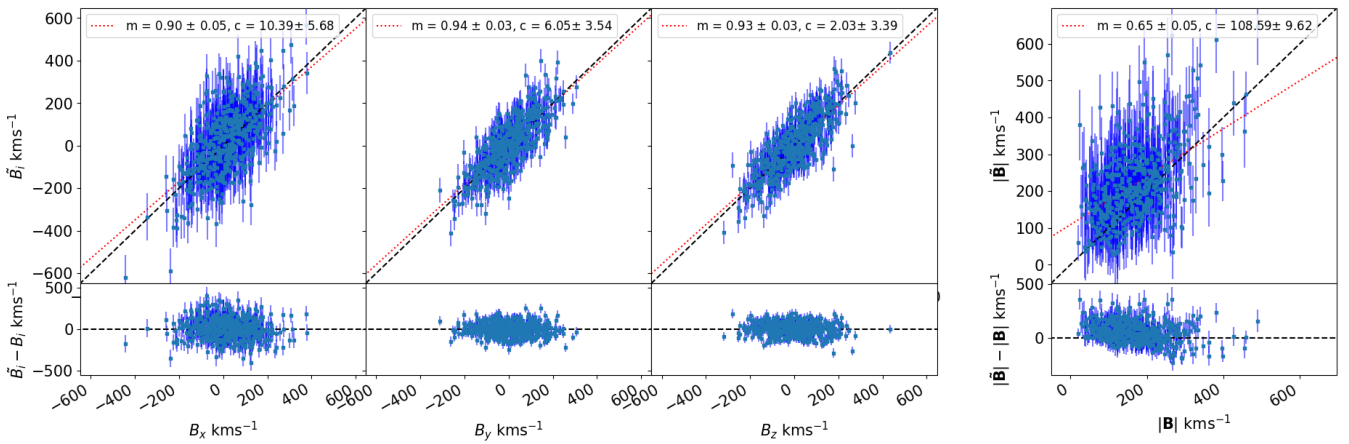


Figure 115: Same as Figure 110, but when the radius of the ideal survey is $240 \text{ Mpc} h^{-1}$.

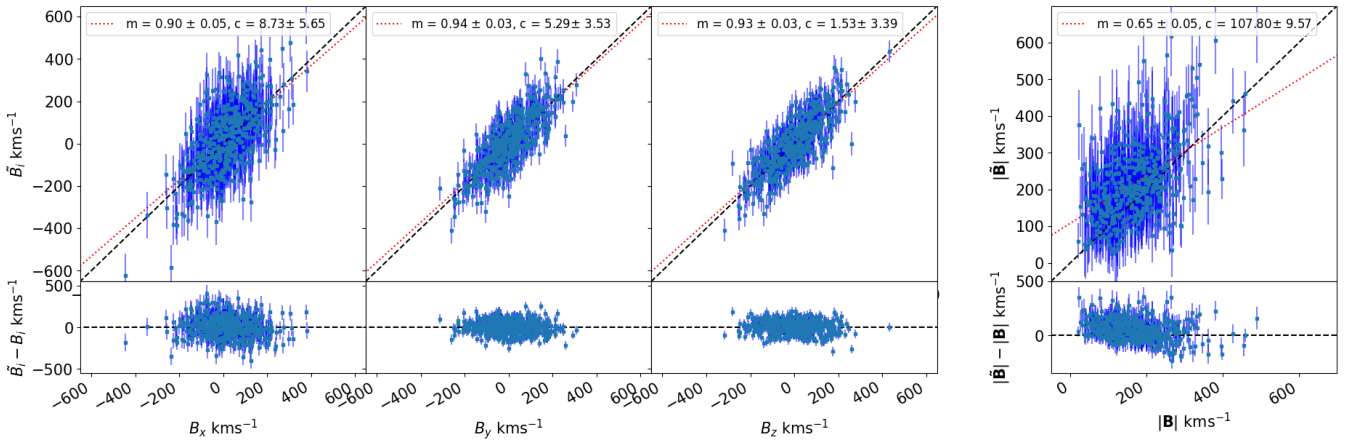


Figure 116: Same as Figure 110, but when the radius of the ideal survey is $275 \text{ Mpc} h^{-1}$.

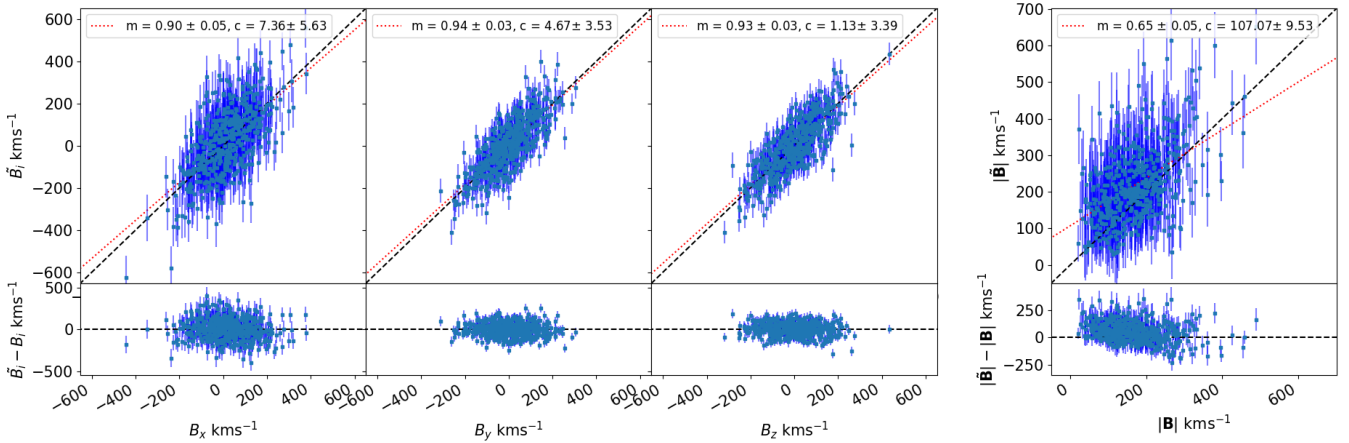


Figure 117: Same as Figure 110, but when the radius of the ideal survey is $310 \text{ Mpc} h^{-1}$.

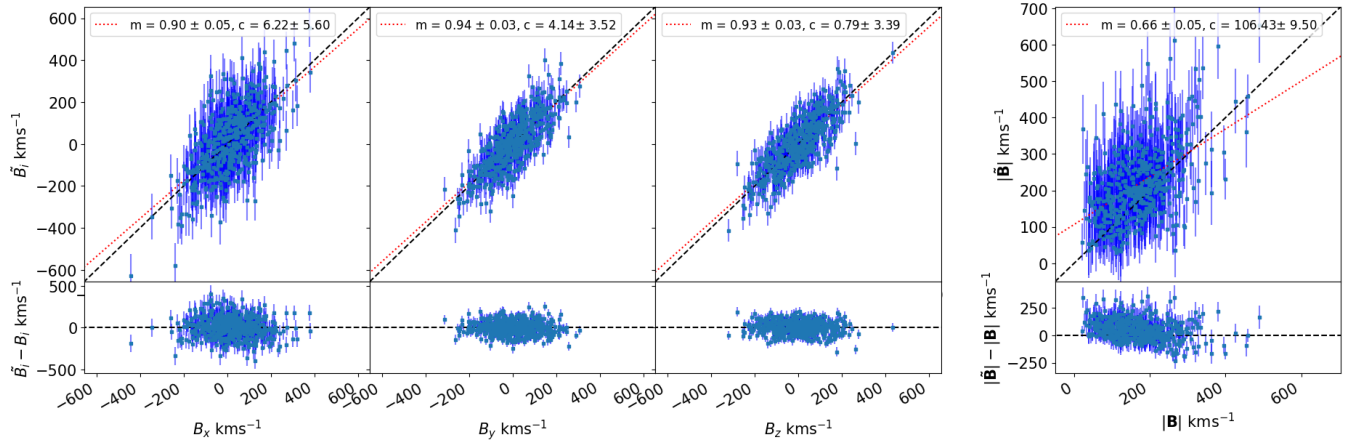


Figure 118: Same as Figure 110, but when the radius of the ideal survey is 345 Mpc h^{-1} .